



A VALIDATION OF THE PARAMETERIZED
REAL-TIME IONOSPHERIC SPECIFICATION MODEL
(PRISM) VERSION 1.7B

THESIS

Shawn D. Filby, Captain, USAF

AFIT/GAP/ENP/07D.03

DISTRIBUTION STATEMENT A

Approved for public release;
Distribution Unlimited

DTIC QUALITY INSPECTED 3

DEPARTMENT OF THE AIR FORCE
AIR UNIVERSITY

AIR FORCE INSTITUTE OF TECHNOLOGY

Wright-Patterson Air Force Base, Ohio

19980120 125

AFIT/GAP/ENP/97D-03

**A VALIDATION OF THE PARAMETERIZED
REAL-TIME IONOSPHERIC SPECIFICATION MODEL
(PRISM) VERSION 1.7B**

THESIS

Shawn D. Filby, Captain, USAF

AFIT/GAP/ENP/97D-03

[DTIC QUALITY INSPECTED 3]

Approved for public release; distribution unlimited

AFTT/GAP/ENP/97D-03

**A VALIDATION OF THE PARAMETERIZED REAL-TIME IONOSPHERIC
SPECIFICATION MODEL (PRISM) VERSION 1.7B**

THESIS

Presented to the Faculty of the Graduate School of Engineering

of the Air Force Institute of Technology

Air University

Air Education and Training Command

In Partial Fulfillment of the Requirements for the

Degree of Master of Science in Physics

Shawn D. Filby, B.S.

Captain, USAF

December 1997

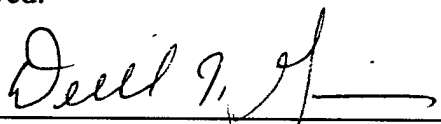
Approved for public release, distribution unlimited

The views expressed in this thesis are those of the author and do not reflect the official policy or position of the Department of Defense or the U. S. Government

A VALIDATION OF THE PARAMETERIZED REAL-TIME IONOSPHERIC
SPECIFICATION MODEL (PRISM) VERSION 1.7B

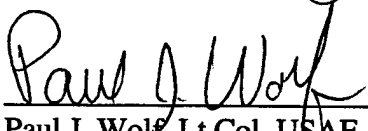
Shawn D. Filby, B.S.
Captain, USAF

Approved:




Derrill T. Goldizen, Major, USAF (Chairman)

24 Nov 97
date



Paul J. Wolf, Lt Col, USAF

24 Nov 97
date



Michael L. Talbert, Major, USAF

25 Nov 97
date

Acknowledgments

I would like to express my sincere appreciation to my faculty advisor, Maj Derrill Goldizen, for his insight and guidance through the course of this research. I would also like to thank my committee members, Lt Col Paul Wolf and Maj Michael Talbert, for their patience and genuine interest in this project.

I am grateful to Lincoln Brown at Computational Physics Inc. for the endless array of e-mail exchanged in the efforts to make PRISM perform to its optimum level. I also owe a great debt to MSgt Pete Rahe for his efforts in honing my UNIX and overall computer skills. Thanks also to Capt Dave Coxwell and Mr. Kevin Scro at the 55th Space Weather Squadron for helping me realize what "Operational Space Weather Forecasting" really means. Thanks to Dr. Dave Anderson for all his guidance and sanity checks on methodology. Thanks also to Pat Doherty for GPS TEC data interpretation and satellite bias confirmation. I want to acknowledge the assistance of the National Geophysical Data Center (NGDC) in providing DISS data over the World Wide Web, specifically to Dr. Raymond Conkright for his insights into the data's accuracy.

Most importantly, I would like to thank my wife, Melanie, who has gone over and above in supporting me through this time-consuming effort. She has certainly made my tour at the Air Force Institute of Technology bearable.

Shawn D. Filby

Table of Contents

	Page
Acknowledgments	ii
Table of Contents	iii
List of Figures	v
List of Tables.....	vii
Abstract	xi
1. Introduction	1
1.1 The Problem	1
1.2 Assumptions	1
1.3 Modeling the Ionosphere.....	2
1.4 The Anatomy of PRISM.....	5
1.4.1 <i>The Low Latitude Model (LOWLAT)</i>	7
1.4.2 <i>The Mid-Latitude Model (MIDLAT)</i>	7
1.4.3 <i>The Low and Mid-Latitude E Layer Model (ECSD)</i>	7
1.4.4 <i>The High Latitude Model</i>	8
1.4.5 <i>Empirical Model Inputs to PIM</i>	8
1.4.6 <i>Parameterization of the Physical Models</i>	10
1.4.7 <i>The Real-Time Adjustment (RTA) Algorithm</i>	11
1.5 Input and Output Parameters.....	13
1.6 Scope	15
2. Previous and Current Validations of PRISM.....	17
2.1 Validation of PRISM Version 1.2	17
2.2 Validation of PRISM Version 1.6b	18
2.3 This Validation of PRISM (Version 1.7b)	19
2.3.1 <i>Methodology</i>	19
2.3.2 <i>Data Used</i>	20
3. Ground Truth Data and Real-time Input Data	21
3.1 Digital Ionospheric Sounding System (DISS) Data	21
3.2 Errors in DISS Data.....	22
3.3 Global Positioning System (GPS) Total Electron Content (TEC) Measurements	23
3.4 Errors in GPS TEC data	25
3.5 Chapter Summary.....	26
4. Results	27

4.1 Statistical Methodology in Data Analysis	27
4.2 Model Bias	28
4.3 Goodness of Fit Test	31
4.4 Averaged Model Output.....	34
4.5 Possible Influence of Topside/Plasmaspheric Electrons on Error Analysis.....	40
4.6 Influence of Geomagnetic Activity	42
5. Conclusions and Recommendations	50
5.1 Summary	50
5.2 Conclusions.....	52
5.3 Recommendations	54
Appendix A: Characteristics of the Ionosphere	58
A.1 The Continuity Equation	58
A.2 Ionospheric Layers.....	61
A.3 Ionospheric Variability	63
Appendix B: Physical Models versus Climatological Models.....	67
Appendix C: Data Inventory	69
Appendix D: Sample PRISM Inputs/Outputs	73
Appendix E: Statistics	77
Appendix F: Plots.....	101
Bibliography	110
Vita.....	113

List of Figures

Figure	Page
Figure 1: Data Flow in PRISM.....	5
Figure 2: Theoretical and Empirical Model Contributions to the PIM Database.....	10
Figure 3: RTA Adjustment Example	12
Figure 4: PRISM Inputs/Outputs.....	15
Figure 5: Wallops Island Reduced Chi-Squared for Winter foF2.....	32
Figure 6: Point Arguello Average hmF2 at Equinox	34
Figure 7: Wallops Island Average hmF2 at Equinox	35
Figure 8: Point Arguello Average Winter hmF2.....	37
Figure 9: Wallops Island Average Winter hmF2	37
Figure 10: Point Arguello Average Winter foF2.....	39
Figure 11: Wallops Island Average Winter foF2	39
Figure 12: Wallops Island Average foF2 at Equinox.....	40
Figure 13: Point Arguello Equinox hmF2 for Low Geomagnetic Activity.....	44
Figure 14: Point Arguello Average Equinox hmF2 for High Geomagnetic Activity.....	45
Figure 15: Point Arguello Average Equinox foF2 for Low Geomagnetic Activity	45
Figure 16: Point Arguello Average Equinox foF2 for High Geomagnetic Activity	46
Figure 17: Point Arguello Average Winter foF2 for Median Geomagnetic Activity.....	48
Figure 18: Point Arguello Average Winter foF2 for High Geomagnetic Activity.....	49
Figure 19: A Typical Mid-Latitude Ionospheric Profile.....	61
Figure 20: A Sample PRISM Input Sequence	73
Figure 21: A Sample PRISM Output File	75
Figure 22: A Sample Electron Density Profile Output.....	76
Figure 23: Point Arguello Reduced Chi-Squared for Equinox hmF2	90
Figure 24: Wallops Island Reduced Chi-Squared for Equinox hmF2.....	90
Figure 25: Point Arguello Reduced Chi-Squared for Summer hmF2	92
Figure 26: Wallops Island Reduced Chi-Squared for Summer hmF2.....	92
Figure 27: Point Arguello Reduced Chi-Squared for Winter hmF2	94
Figure 28: Wallops Island Reduced Chi-Squared for Winter hmF2	94
Figure 29: Point Arguello Reduced Chi-Squared for Equinox foF2.....	96
Figure 30: Wallops Island Reduced Chi-Squared for Equinox foF2	96
Figure 31: Point Arguello Reduced Chi-Squared for Summer foF2.....	98
Figure 32: Wallops Island Reduced Chi-Squared for Summer foF2	98
Figure 33: Point Arguello Reduced Chi-Squared for Winter foF2	100
Figure 34: Wallops Island Reduced Chi-Squared for Winter foF2.....	100
Figure 35: Point Arguello Average Summer hmF2	101
Figure 36: Wallops Island Average Summer hmF2.....	101
Figure 37: Point Arguello Average foF2 at Equinox	102
Figure 38: Point Arguello Average Summer foF2	102
Figure 39: Wallops Island Average Summer foF2.....	103

Figure 40: Point Arguello Average Equinox hmF2 for Median Geomagnetic Activity	103
Figure 41: Point Arguello Average Equinox foF2 for Median Geomagnetic Activity ..	104
Figure 42: Point Arguello Average Winter hmF2 for Low Geomagnetic Activity	104
Figure 43: Point Arguello Average Winter hmF2 for Median Geomagnetic Activity ...	105
Figure 44: Point Arguello Average Winter hmF2 for High Geomagnetic Activity	105
Figure 45: Point Arguello Average Winter foF2 for Low Geomagnetic Activity	106

List of Tables

Table	Page
Table 1: Geophysical Parameter Values.....	11
Table 2: Horizontal Grid Parameters	11
Table 3: Summary of PRISM and ICED validation results	17
Table 4: Global Positioning Satellite Biases	24
Table 5: Seasonal hmF2 (km) Mean Residual and Standard Deviation Values	29
Table 6: Seasonal foF2 (MHz) Mean Residual and Standard Deviation Values	31
Table 7: Point Arguello foF2 Reduced Chi-Square Rank By Hour	33
Table 8: Wallops Island foF2 Reduced Chi-Square Rank By Hour.....	33
Table 9: Point Arguello Equinox hmF2 Mean Residual and Standard Deviation by Geomagnetic Activity.....	42
Table 10: Point Arguello Equinox foF2 Mean Residual and Standard Deviation by Geomagnetic Activity.....	43
Table 11: Point Arguello Winter hmF2 Mean Residual and Standard Deviation by Geomagnetic Activity.....	47
Table 12: Point Arguello Winter foF2 Mean Residual and Standard Deviation by Geomagnetic Activity.....	47
Table 13: Inventory of Data Used	69
Table 14: Equinox Hourly hmF2 Mean Residuals and Standard Deviations of the Mean Residuals	77
Table 15: Summer Hourly hmF2 Mean Residuals and Standard Deviations of the Mean Residuals	79
Table 16: Winter Hourly hmF2 Mean Residuals and Standard Deviations of the Mean Residuals	81
Table 17: Equinox Hourly foF2 Mean Residuals and Standard Deviations of the Mean Residuals	83
Table 18: Summer Hourly foF2 Mean Residuals and Standard Deviations of the Mean Residuals	85
Table 19: Winter Hourly foF2 Mean Residuals and Standard Deviations of the Mean Residuals	87
Table 20: Reduced Chi-Squared for Equinox hmF2.....	89
Table 21: Reduced Chi-Squared for Summer hmF2.....	91
Table 22: Reduced Chi-Squared for Winter hmF2	93
Table 23: Reduced Chi-Squared for Equinox foF2.....	95
Table 24: Reduced Chi-Squared for Summer foF2.....	97
Table 25: Reduced Chi-Squared for Winter foF2	99

List of Symbols

B_y – The y-component of the Interplanetary Magnetic Field (+ east, - west) (nT).

B_z – The z-component of the Interplanetary Magnetic Field (+ north, - south) (nT).

EBARE – the DMSP-measured mean electron energy (keV).

EBARI – the DMSP-measured mean ion energy (keV).

EFLUXE – the DMSP-measured energy flux of electrons ($\text{erg cm}^{-2} \text{s}^{-1}$).

EFLUXI – the DMSP-measured energy flux of protons ($\text{erg cm}^{-2} \text{s}^{-1}$).

F10.7 – The measure of 10.7 cm radio flux ($10^{-22} \text{ W m}^{-2} \text{ Hz}^{-1}$) produced by the Sun which acts as a surrogate parameter for the EUV flux.

F_j – the forces acting on species 'j' (N).

FHEP – the DMSP-measured fraction of He^+ ions compared to the total number of ions (unitless).

FHP – the DMSP-measured fraction of H^+ ions compared to the total number of ions (unitless).

foE – The critical radio frequency below which radio waves are reflected off of the E layer in the ionosphere (MHz).

foF1 -- The critical radio frequency below which radio waves are reflected off of the F1 layer in the ionosphere (MHz).

foF2 – The critical radio frequency below which radio waves are reflected off of the F2 layer in the ionosphere (MHz).

FOP – the DMSP-measured fraction of O^+ ions compared to the total number of ions (unitless).

GLAT – Geomagnetic latitude (degrees).

GLON – Geomagnetic longitude (degrees).

hmE – the E layer electron density peak height in kilometers (km).

hmF1 – the F1 layer electron density peak height in kilometers (km).

hmF2 – the F2 layer electron density peak height in kilometers (km).

K_p – The planetary average of geomagnetic activity indicators. A K_p of 0 indicates a period of low geomagnetic activity and a K_p of 9 indicates a period of strong geomagnetic activity (unitless).

k – Boltzmann's constant, 1.380662 J K⁻¹.

L_j^T – a term in the energy equation representing the heat loss rate (J s⁻¹).

L_j – A term in the continuity equation representing the loss of species 'j' (number s⁻¹).

N_e – the number density of electrons per cubic meter of electrons.

N_{ec} – the number density of electrons per cubic meter at the critical frequency height.

VP_j – the generalized pressure tensor term (N s⁻¹).

P_j – A term in the continuity equation representing the production of species 'j' (number s⁻¹).

Q_j – A term in the energy equation which represents the local heating rate of the species 'j' (J s⁻¹).

∇q – the divergence of the heat flow (J s⁻¹).

SIG_E – one standard deviation uncertainty in the energy flux of electrons (erg cm⁻² s⁻¹).

SIG_I – one standard deviation uncertainty in the energy flux of ions (erg cm⁻² s⁻¹).

STEC – The measured slant total electron content (TEC units).

TEC – The total number of electrons in a vertically-integrated column of unit cross-sectional area.

T_e – electron temperature. (Kelvin).

T_i – ion temperature. (Kelvin).

UT – Universal Time given in seconds in PRISM output, but usually given in hours and minutes (hh:mm).

ν_c – Critical frequency (MHz).

ρ_j – the density of species 'j' (kg m^{-3}).

χ – The solar zenith angle, the angle between the local vertical and a line drawn to the center of the Sun (degrees).

Abstract

The most current version of the Parameterized Real-time Ionospheric Specification Model (PRISM), version 1.7b, was validated using Digital Ionospheric Sounding System (DISS) measurements of F2 layer critical frequency (foF2) and F2 peak electron density height (hmF2) as the "ground truth." PRISM was executed, first, with no real-time input parameter and, second, with Global Positioning System (GPS) Total Electron Content (TEC) measurements as the sole real-time input parameter. Hourly values of hmF2 and foF2 over 123 days in 1994-1996 (solar minimum conditions) and covering three seasons (equinox, summer solstice, and winter solstice) were compared for Wallops Island, Virginia and Point Arguello, California, which both have a GPS receiver and a nearby DISS station. Values of hmF2 and foF2 from the DISS data, the PRISM output with no real-time input parameters, and the PRISM output with the GPS TEC measurements are compared as a function of season and local time. Results indicate PRISM overestimates foF2 by 20-30% when ingesting GPS TEC. On a subsequent execution of PRISM, the GPS TEC measurements were decreased by four TEC units as an estimation of the topside light ion (He^+ , H^+) and plasmaspheric electrons which are not considered in the physical models of PRISM. PRISM underestimates foF2 by 30-40% and underestimates hmF2 by as much as 40 km in the post-midnight time-frame when driven by the corrected TEC values.

A VALIDATION OF THE PARAMETERIZED REAL-TIME IONOSPHERIC SPECIFICATION MODEL (PRISM) VERSION 1.7B

1. Introduction

1.1 *The Problem*

The problem addressed in this research is a validation of the Parameterized Real-time Ionospheric Specification Model (PRISM) version 1.7b. In this research, PRISM hourly calculations without any real-time input parameters and PRISM hourly calculations using the real-time input of Global Positioning System measurements of total electron content (TEC) are compared to Digital Ionospheric Sounding System (DISS) measurements, considered to be “ground-truth.” The two parameters used for comparison are the critical frequency (foF2) and the height (hmF2) of the electron density peak for the ionospheric F2 layer. A quantitative accuracy of PRISM as a function of season, local time, and geomagnetic activity is assessed. Also, the influence on PRISM calculations of foF2 and hmF2 from topside/plasmaspheric electrons is considered as a function of season and local time. (The term topside/plasmaspheric electrons, as used in this paper, is defined as the free electrons associated with ionospheric light ions (e.g. H^+ , He^+) not modeled by PRISM and the free electrons above the top of the ionosphere (≈ 1000 km) and below the GPS satellite orbit ($\approx 22,000$ km) along the GPS broadcast ray path.)

1.2 *Assumptions*

There are four assumptions used in this research. First, the DISS measurements are taken to be the true F2 critical frequency and F2 peak electron density height. DISS data

is considered reliable to 17km for hmF2 measurements and 0.4 MHz for foF2 [Titheridge, 1990]. Second, four TEC units correctly account for the contribution of topside/plasmaspheric electrons to GPS measurements, regardless of time of day and season [Anderson, 1997]. Third, the behavior of the ionosphere at vernal equinox and autumnal equinox is similar enough to allow grouping of both equinox measurements/calculations because solar flux is similar during both seasons. In addition, PRISM parameterizes data from both vernal and autumnal equinox into one category; consequently, separating vernal and autumnal data would yield similar results. Fourth, the spatial coherence length of the real-time input parameter, TEC, is much larger than the distance between Wallops Island, Virginia, and Westford, Massachusetts, as well as the distance between Point Arguello, California, and Vandenberg AFB, California. In a previous validation of PRISM [Coxwell, 1996] the influence of a single real-time input parameter was noted 2,000 km away from the measurement, considerably farther than the distance between either two sites. GPS TEC measurements are calculated as a vertical electron content from the point of intersection with the ionosphere, which involved an atmospheric window encompassing each respective DISS location. Also, it is implied in this assumption that there is not an appreciable difference in mid-latitude ionospheric parameters over this distance.

1.3 Modeling the Ionosphere

Science has made a noble attempt to understand the ionosphere over the past fifty years but the ionosphere has been reluctant to give away many of its secrets. Current modeling of the ionosphere has been likened to the state of tropospheric weather

prediction modeling in the 1950's: crude, with limited observations leading to somewhat broad and unreliable forecasting abilities. As more observations from satellites, rockets, coherent and incoherent scatter radar, magnetometers, lidar, and other ground-based instruments are made available, variations of the ionosphere, both large and small scale, will give more insight into the modeling challenge.

In addition to the scarcity of observational data, the ionosphere fluctuates radically, making a complete understanding more complex and elusive. Changes in solar radiation flux, altitude, latitude, season, solar cycle, neutral winds, gravity waves, geomagnetic activity, and tides can produce large shifts in the electron contents and altitudes of various layers of the ionosphere. Appendix A provides a brief discussion of physics, chemistry, and variability observed in the ionosphere.

Ionospheric variability impacts many facets of space-based and some surface-based operations. One notable impact is caused by small-scale changes in ionospheric electron density along a radio signal path, resulting in rapid signal fluctuations in satellite transmissions (scintillation) and a degradation of communications. Some military organizations rely on ground-to-ground high frequency (HF) communications, which can be rendered useless by unanticipated changes in the size and shape of the ionosphere, hampering battlefield information flow.

Communication is not the only area affected by these disturbances: navigation systems, satellite orbits, radar, and, to some extent, even entire power grids and pipelines are all subject to these variations [Schunk and Sojka, 1996]. Optimization of space-based systems provides another impetus for accurate ionospheric modeling. Ionospheric

effects on the neutral atmosphere can affect satellite drag, prompting course corrections to keep satellites in the desired orbit.

The lead organization in monitoring the global ionosphere and its effects on DoD operations is the 55th Space Weather Squadron (55th SWXS) at Falcon Air Force Base, Colorado Springs, Colorado. They are charged with a 24-hour global watch of the solar-terrestrial environment and geomagnetic activity. One of their tools is an ionospheric model named PRISM: the Parameterized Real-time Ionospheric Specification Model.

PRISM was constructed by programmers at Computational Physics Inc. (CPI) based in Waltham, Massachusetts. PRISM ties together four physics-based ionospheric models while allowing real-time (or near real-time) data from satellites or ground based instrumentation to modify eight model output parameters, which can be provided on a global scale or for a single location. Real-time inputs are ionosonde critical frequencies and heights of the ionospheric layers (E, F1, and F2); satellite-measured total electron content (TEC); and Defense Meteorological Satellite Program (DMSP) ion drift velocities and *in situ* electron/ion measurements.

PRISM is used by the 55th SWXS to construct ionospheric profiles in the analysis of near real-time or past ionospheric events; PRISM does not provide forecasting capability.

PRISM is based on a theoretical climatological model data base which can be modified by real-time input parameters, making this model a step above the average climatological model. A discussion of physical models as compared to climatological models is contained in Appendix B. What makes PRISM a good ionospheric model? A look into the inner-workings of PRISM are discussed in the following section.

1.4 The Anatomy of PRISM

PRISM is the marriage of real-time parameters, four distinct physical ionospheric models, and a weighting algorithm. The collective name for the four ionospheric models is the Parameterized Ionospheric Model, or PIM. The weighting algorithm, called the Real-Time Adjustment (RTA) algorithm, assimilates the real-time data and the four-model representation of the ionosphere to produce one or more user-selected output(s). See Figure 1 below for the data flow in PRISM.

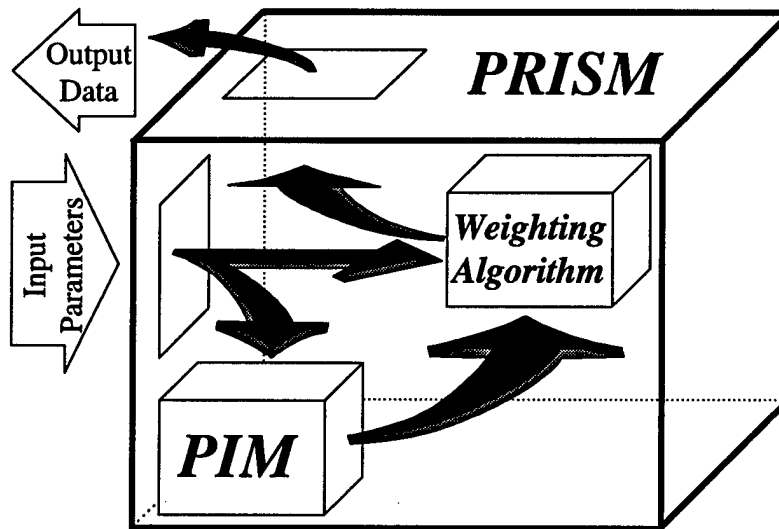


Figure 1: Data Flow in PRISM

[Coxwell, 1996]

Because of the ionosphere's high degree of variability with latitude and altitude, the selection of PIM's models was deliberate. PIM combines a low-latitude F layer model (LOWLAT), a mid-latitude F layer model (MIDLAT), a low- and mid-latitude E-layer Continuous Slowing Down Model (ECSD), and a high latitude model (the Time-

Dependent Ionospheric Model, TDIM). The four theoretical models utilize three governing equations for the ionosphere: the continuity equation (1), the momentum equation (2), and the energy equation (3), which are respectively given below:

$$\frac{dn}{dt} + \nabla \cdot nv = P - L \quad (1)$$

$$\rho_j \frac{dv_j}{dt} + \nabla \cdot \bar{P}_j = \sum_j n_j F_j \quad (2)$$

$$n_j k \frac{dT}{dt} = Q_j - L_j^T - n_j k T_j \nabla \cdot v_j - \nabla q + \sum_j n_j F_j v_j \quad (3)$$

In the continuity equation (1), the first term on the left side is the time rate of change of number density, the second is the flux divergence of the density, and on the right side of the equation is the production and loss of electrons. The momentum equation (2) equates the time rate of change of momentum plus the divergence of the pressure field to the sum of forces acting on the species j. The energy equation (3) states that the time rate of change of the energy per unit volume equals local heating (Q), the heat loss rate (L^T), the third term which represents the compressional heating/cooling of the volume, the fourth term which is the divergence of heat flow, plus the last term which is the work done on species "j."

Also, all four models assume the earth's magnetic field structure to be a tilted dipole, and all are consistent in their treatment of chemical reaction rates and collision rates.

1.4.1 The Low Latitude Model (LOWLAT)

LOWLAT was developed by Dr. David N. Anderson of the USAF Phillips Lab/Ionospheric Effects Branch, Hanscom AFB, MA. This model solves the diffusion equation for O^+ (the principal ion formed by solar EUV flux in the F region of the ionosphere) along a large number of magnetic flux tubes to build an altitude profile. LOWLAT utilizes the empirical Ion/Electron Temperature Model developed by Brace and Theis [1981] which is needed to calculate heat transport at low latitudes. Neutral thermospheric winds are calculated by the Horizontal Wind Model (HWM90) [Hedin *et al.*, 1988], and a model by Fejer *et al.* [1995] provides empirical plasma drift velocities to include the effects of the equatorial dynamo.

1.4.2 The Mid-Latitude Model (MIDLAT)

The mid-latitude F region model is essentially the LOWLAT model but with the equatorial dynamo electric field effects eliminated [Daniell, 1991].

1.4.3 The Low and Mid-Latitude E Layer Model (ECSD)

The low and mid-latitude E layer model, E-layer Continuous Slowing Down Model (ECSD), was developed by Dwight T. Decker and John R. Jasperse. It incorporates photoelectrons using the continuous slowing down approximation [Decker *et al.*, 1996]. In this model, ion concentrations are calculated assuming local photochemical equilibrium, and the E layer is maintained throughout the night by imposing a small nighttime plasma source [Daniell *et al.*, 1995].

1.4.4 The High Latitude Model

The fourth model is the Time Dependent Ionospheric Model (TDIM) developed by R. W. Schunk and J. J. Sojka at Utah State University which models both the E and F layers. This model is similar to LOWLAT and MIDLAT except the continuous flux tubes are truncated and the boundary condition is modeled by the empirical High-Latitude Convection (HLC) Model. In addition, the flux tubes move under the influence of the high-latitude horizontal convection electric field: the near-vertical geomagnetic field drives the ionization horizontally in the $\mathbf{E} \times \mathbf{B}$ drift direction. Lastly, the model allows for the effects of ionization by precipitating auroral particles [Daniell, 1991]. Appendix A provides a general overview of ionospheric variability with latitude.

1.4.5 Empirical Model Inputs to PIM

CPI also needed to incorporate six empirical models into PIM: the Plasma Drift Model, the Horizontal Wind Model (HWM90), the Ion/Electron Temperature Model, the High Latitude Convection Model, the B3C Electron Transport Model, and the Electron Precipitation Model. The Plasma Drift Model was developed by Fejer et al. [1995] using an ion drift meter aboard the Atmospheric Explorer E satellite. It provides the $\mathbf{E} \times \mathbf{B}$ driven vertical drift used in the momentum equation. This empirical model is critical to LOWLAT's ability to predict the Appleton Anomaly (high concentrations of electrons on either side of the geomagnetic equator in the post-sunset sector). HWM90, developed by A. E. Hedin, *et al.* [1988], gives neutral wind information for momentum transfer from collisions (momentum equation) and energy exchange from collisions (energy equation). Hedin *et al.* analyzed wind data obtained by the Atmospheric Explorer E satellite, the

Dynamics Explorer 2 satellite, and ground-based incoherent scatter radar and Fabry-Perot optical interferometers to construct HWM90. It is used by both LOWLAT and MIDLAT. The Ion/Electron Temperature Model by Brace and Theis [1981] is also used by LOWLAT and MIDLAT. It influences ion/electron temperature- dependent chemical reactions in the loss terms of the continuity equation and momentum transfer and pressure terms in the momentum equation. This empirical model of global distributions of ion/electron temperatures was constructed using Langmuir probe measurements in the vicinity of the Atmospheric Explorer C and ISIS satellites.

The next three empirical models discussed are unique to the high latitude regions and are incorporated into the Time Dependent Ionospheric Model (TDIM). The High Latitude Convection (HLC) Model patterns high-latitude electric fields, electric potential, field-aligned currents, and Joule heating. It was developed with data from the Dynamics Explorer 2 and the Polar-Orbiting Geophysical Observatory 6 (OGO 6) satellites by J. P. Heppner and N. C. Maynard [1987]. Inputs to the heat source term in the energy equation and the transport term in the momentum equation are based on the HLC model. The BC3 Electron Transport Model [Strickland *et al.*, 1976] provides ion production rates and is coupled with the electron precipitation model developed by Hardy *et al.* [1985]. These two empirical models combine to solve part of the production term in the continuity equation for the auroral regions. Figure 2 shows which empirical model contributes to which physical model.

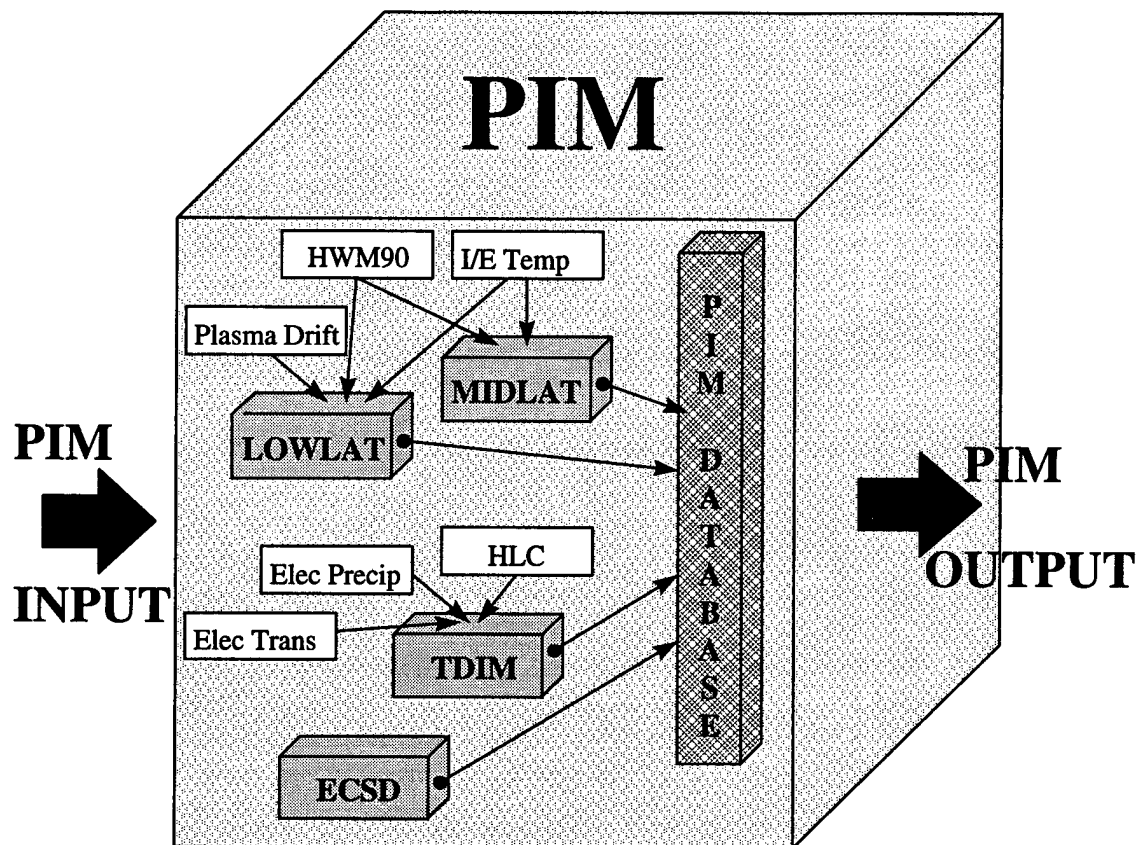


Figure 2: Theoretical and Empirical Model Contributions to the PIM Database
The four theoretical (physical) models are in the dark boxes while the empirical models are in the white rectangles. All four theoretical models contribute to the PIM database.

1.4.6 Parameterization of the Physical Models

The parameterization of the physical models was accomplished in two steps. First, CPI generated four model output databases for a discrete set of geophysical conditions. Each database consists of ion density profiles on a discrete latitude/longitude grid for a 24-hour period. Second, to reduce storage requirements, the databases were approximated with semi-analytic functions (empirical orthonormal functions - EOFs)

[Daniell, 1995]. Due to time and computer resource limitations, only a few discrete values of each geophysical parameter were used (See Table 1). The space and time grid parameters are summarized for each latitude region in Table 2.

Table 1: Geophysical Parameter Values
[Daniell et al., 1995]

Model	Solar Activity, $F_{10.7}$	Magnetic Activity, K_p	IMF B_y Direction	Number of Databases
LOWLAT	70, 130, 210	N/A	N/A	36
MIDLAT	70, 130, 210	1, 3.5, 6	N/A	54
ECSD	70, 130, 210	1, 3.5, 6	N/A	54
TDIM	70, 130, 210	1, 3.5, 6	+, -	324

Table 2: Horizontal Grid Parameters
[Daniell et al., 1995]

Model	Magnetic Latitude	Magnetic Longitude	UT
LOWLAT	-32° to 32° in 2° steps	0°, 30°, 139°, and 237°	MLT: 0.0 to 23.5 in .5 hour steps
MIDLAT	30° to 74° and -30° to -74° in 4° steps	0° to 345° in 15° steps	0100 to 2300 in 2 hour steps
ECSD	-76° to 76° in 4° steps	0° to 345° in 15° steps	0100 to 2300 in 2 hour steps
TDIM	51° to 89° and -51° to -89° in 2° steps	MLT: 0.5 to 23.5 in 1 hour steps	0100 to 2300 in 2 hour steps

1.4.7 The Real-Time Adjustment (RTA) Algorithm

The Real-Time Adjustment (RTA) algorithm modifies the PIM data base constructed by the four theoretical models by adjusting the PIM output with correction factors for each of six output parameters: foF2, foE, hmF2, hmE, O⁺ density at a specific altitude (i.e., the DMSP altitude), and the O⁺ scale height at a specific altitude (i.e., the DMSP

altitude). The starting value for each of these ‘correction factors’ is zero and is changed if a real-time measurement for a given parameter is entered. For example, if DISS data is entered giving a value for hmF2 of 300 km and the PIM output gave a hmF2 value of 275 km, the correction factor for hmF2, ΔhmF2 , would be +25 km.

The RTA adjusts the electron density profile (EDP) generated in a specific order: first, it corrects F2 and E layer heights; secondly, critical frequencies (number densities) of the F2 and E layers are adjusted; lastly, the topside profile is adjusted. If the real-time input parameter does not influence one of the correction factors (e.g. a sole DISS measurement of hmF2 would not affect the critical frequency), the correction factor remains zero, thus no correction is made.

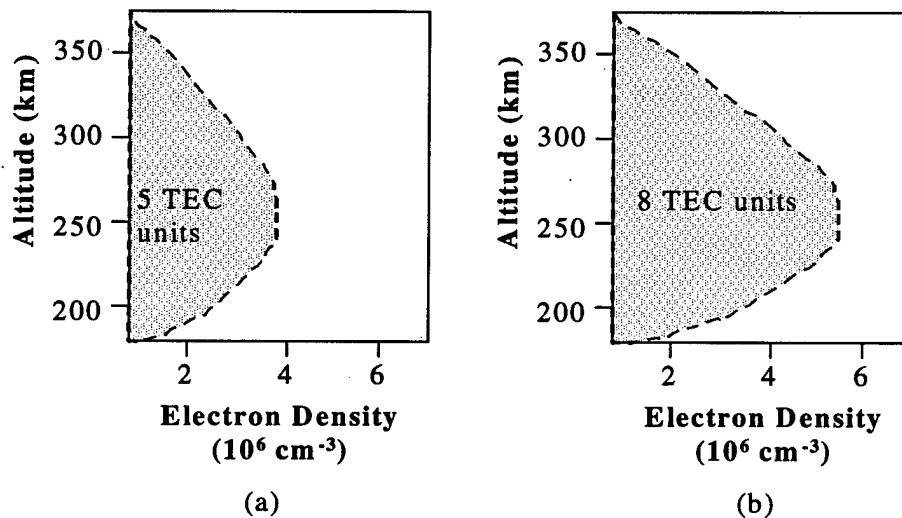


Figure 3: RTA Adjustment Example

Figure 3 demonstrates the method the RTA uses to adjust the electron density profile (EDP) when PRISM ingests GPS TEC. In this example PIM estimates the total electron

content to be 5 TEC units and GPS TEC is measured to be 8 TEC units. First (a), PIM determines the EDP, which includes an estimation of the total electron content (the “area” under the curve). Then the RTA adjusts the TEC “area” (b) by translating the profile shape left or right as appropriate until the number density under the profile matches the GPS TEC input. Note that the peak height has not changed (it remains at about 255 km, identical to what PIM estimated).

In order to use GPS TEC data, PRISM must convert the TEC measurement into an equivalent point measurement. When close to a DISS site, the TEC data is ingested as a vertical equivalent TEC at the Ionospheric Intersection Point (IIP), which is latitude and longitude of penetration of the GPS ray path into the top of the ionosphere ($z \approx 1000$ km). If the IIP is farther than 1000 km from the nearest DISS site, then the TEC is converted into an equivalent F2 layer number density value. Thus, ingesting TEC measurements will solely affect critical frequency values.

1.5 Input and Output Parameters

There are a minimum of seven input parameters required by PRISM. The parameterization in PIM requires time, Julian date, and year to account for diurnal, seasonal, and solar cycle variations, respectively. The fourth parameter is a geomagnetic index, K_p , which is the average of 12 global magnetic field observations of geomagnetic activity from selected locations around the globe and is produced every three hours. A K_p value ranges from 0 for a ‘very quiet’ to 9 for a ‘very disturbed’ geomagnetic state [Hargreaves, 1992]. The fifth parameter is the ground-based measure of the solar radio flux observed at a wavelength of 10.7 cm, called “F10.7.” PIM requires a daily F10.7

value and a running 90-day average value. Lastly, the user is prompted for the magnitude and direction of the interplanetary magnetic field (IMF) B_y (+ east or - west) and B_z (+ north or - south). PIM uses these parameters to calculate the 'best fit' representation of the ionosphere using the semi-analytic functions derived from its theoretical climatological database (created from the output of the four physics-based models that make up PIM).

The PIM output is then fed to the RTA algorithm along with any 'real-time' or 'near real-time' input data. This 'real-time' input can come from three sources: the Defense Meteorological Satellite Program (DMSP) which can provide measurement of 13 different ionospheric properties, the Digital Ionospheric Sounding System (DISS) data providing four ionospheric measurements, or the Global Positioning Satellite (GPS) (or any other platform or ground-based instrument) total electron content measurements. A total electron content measurement is the height integrated number of electrons found within a 1 m^2 column from the surface of the earth to the vertical extent of the column. Figure 4 lists the individual measurements obtained by each source. For a more detailed discussion of how the measurements of 'real-time' inputs are obtained, see Chapter 3 of this thesis. A sample input sequence is provided in Appendix D.

The model's output can be produced in two forms: regionally, or by user-specified location(s). Outputs can be chosen by latitude/longitude in either geographic or geomagnetic coordinates. PRISM also allows for three choices in output format: electron density profiles; critical frequencies, heights of each ionospheric layer, and

vertical TEC values; or a combination of both of these choices. For a sample output file refer to Appendix D.

Input parameters are ingested into PRISM as shown in the figure below:

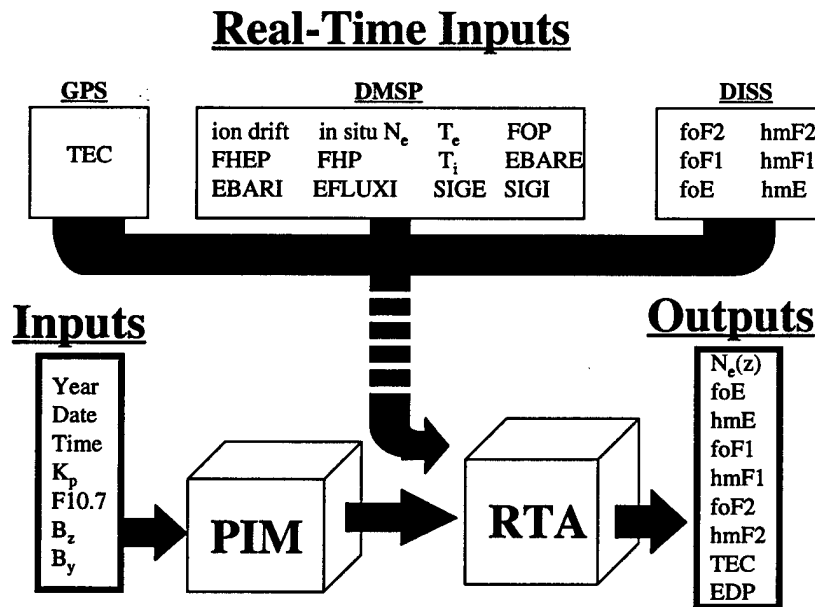


Figure 4: PRISM Inputs/Outputs

1.6 Scope

This thesis contains the hourly comparison of three PRISM executions: the first with no real-time inputs (referred in this paper as ‘PRISM/PIM’), the second with the real-time input of GPS TEC measurements (referred in this paper as ‘PRISM/TEC’), and the third with a real-time input of GPS TEC measurements minus four TEC units to correct for topside/plasmaspheric electrons (referred to in this paper as ‘PRISM/corTEC’). (The reasoning for this correction is discussed in the next paragraph.) These three PRISM executions will be compared to DISS data from a station in close proximity to the GPS

receiver used in measuring the total electron content ingested by PRISM. Due to the limited availability of data and the requirement that the DISS and GPS receivers be in close proximity, only two locations are used in this research: the DISS station at Point Arguello, California, (35.6N 239.4E) coupled with the GPS receiver at Vandenberg AFB, California, (34.7N, 239.4E); and the DISS station at Wallops Island, Virginia, (37.8N, 284.5E) coupled with the GPS receiver at Westford, Massachusetts, (42.9, 280.0E). Point Arguello and Wallops Island are at geomagnetic latitude 41.49N and 49.83N respectively. Even though only two sites were chosen, the copious amounts of hourly data gave a reasonable statistical base for analysis. The available data, as listed in Appendix C, is from the solar quiet period of March 1994, through January 1996.

Comparisons are made between PRISM/PIM, PRISM/TEC and DISS data to quantify the model's performance. The four physical models which comprise PIM do not take into account topside/plasmaspheric electrons measured by GPS. This thesis also investigates whether the topside/plasmaspheric electron content, as part of the GPS TEC measurements, should be eliminated before ingesting into PRISM to more accurately reflect the ionosphere's true critical frequencies and layer heights. The correction of four TEC units is an estimate, provided by Dr. Dave Anderson of the United States Air Force's Philips Laboratory, of the topside/plasmaspheric electron contribution to GPS TEC measurements. GPS satellites orbit 22,000 km above the surface of the earth and include the topside/plasmaspheric electrons in their measurement of electron content.

2. Previous and Current Validations of PRISM

2.1 Validation of PRISM Version 1.2

The first validation of PRISM was conducted by CPI in 1994 using the then-current version 1.2. CPI compared the results of PRISM to the ionospheric model then used by the Space Forecast Center, the Ionospheric Conductivity and Electron Density (ICED) model. The validation used a data set comprising measurements from analog ionosondes, digisondes, polarimeters, incoherent scatter radars, Defense Meteorological Satellite Program (DMSP) instrumentation, and particle precipitation data over the solar active period of 2 October through 6 October 1989 and additional data from 9 October 1989. This data was divided into two sets; one set was ingested by PRISM (referred to as 'driving') and the second set served as the 'ground truth' used to quantify model accuracy.

A summary of the results are shown in the table below:

Table 3: Summary of PRISM and ICED validation results

[Daniell et al, 1994]

Quantity	ICED	PRISM	Improvement
RMS foF2 error (MHz)	1.5 MHz	0.7 MHz	54%
RMS NmF2 error (%)	40%	20%	50%
RMS TEC error (TEC units)	7.1	3.1	56%
RMS TEC error (%)	31%	8%	74%
RMS hmF2 error (km)	25 km	6 km	75%

PRISM showed a significant improvement over the operational model ICED and demonstrated its ability to ingest real-time data from a variety of sources. However, in regions well away from a real-time data source, the improvement over ICED was minimal [Daniell *et al.*, 1994]. Also, the data set selected would not be a representative data set available to operational space forecasters at the 55th SWXS.

2.2 Validation of PRISM Version 1.6b

The validation study of PRISM version 1.6b was performed by Coxwell [1996] and focused on the operational needs of the 55th Space Weather Squadron (55th SWXS). In Capt Coxwell's research, he used data from the solar quiet months of March 1994, through January 1996. His real-time input parameters were critical frequencies and layer heights from DISS stations and total electron content measurements from Global Positioning Satellites. PRISM calculations of total electron content at 0000L, 0600L, 1200L, and 1800L at two latitudes (30° N and the equator) for three seasons (Equinox, Summer, and Winter) were compared to "ground truth" measurements of total electron content taken from the NASA dual-frequency radar altimeter on-board the TOPEX satellite during 1995. TOPEX is the TOPographic EXperiment satellite which was launched to measure sea-surface heights.

Several conclusions were made about PRISM's performance with this data set. The first was a determination of the radius of influence of a single real-time observation. It was shown that at 2000 km from the location of the observation, model outputs were identical to those obtained by PRISM with no real-time data inputs (PIM output). This revealed that if all the currently available real-time DISS stations and GPS observations

stations provided input data, only 24% of the earth's ionosphere could be modeled by PRISM with real-time inputs and the remaining 76% would be modeled by PIM alone. Secondly, PRISM TEC calculations driven by DISS data (PRISM/DISS) generally performed worse than PIM alone during equinox seasons; however, the same tests executed for summer and winter solstice months showed PRISM/DISS with a slight advantage over PIM (using TOPEX TEC values as ground truth). And lastly, the thesis concluded that for mid-latitude stations, the PRISM calculations when driven by GPS TEC (PRISM/TEC) outperformed both PRISM/DISS and PIM for summer, fall, and winter; for equatorial stations, PRISM/TEC did not perform as well as both PIM and PRISM/DISS in winter [Coxwell, 1996].

2.3 This Validation of PRISM (Version 1.7b)

2.3.1 Methodology

PRISM version 1.7b was executed to generate three distinct data sets for two geographical locations, Wallops Island, Virginia, and Point Arguello, California. The first data set was generated by PRISM without any real-time data inputs, hereafter referred to as "PRISM/PIM", which was used as a control data set to quantify improvements or shortfalls. The second execution consisted of PRISM driven by GPS total electron content (TEC) measurements taken at Westford, Massachusetts, and Vandenberg AFB, California, hereafter referred to as "PRISM/TEC"; in the third execution, PRISM was driven by GPS TEC reduced by four TEC units to correct for topside/plasmaspheric electrons, hereafter referred to as "PRISM/corTEC". Ionospheric

profile parameter measurements taken by the DISS stations at Wallops Island and Point Arguello were used as the ground truth for the three data sets. The two parameters used for the validation were hmF2 (height of the ionospheric F2 layer peak electron density) and foF2 (critical frequency of the F2 layer) which is a function of number density at the F2 peak (see Figure 19).

2.3.2 Data Used

The data set used in this validation is a subset of the data used in validation of version 1.6b. GPS TEC measurements were provided by Pat Doherty at the United States Air Force's Philips Laboratory in Massachusetts. Values were extracted for each hour based upon a minimum satellite elevation of 40° to assure vertical estimates of TEC were not greatly influenced by horizontal gradients in electron density. Ms. Doherty also confirmed satellite bias and receiver bias numbers for the period of 1994-1996.

DISS data was extracted from the National Geophysical Data Center archives through the World Wide Web (<http://ngdc.noaa.gov>) and used for ground truth comparisons. Methods of obtaining (and estimating inconsistencies in) DISS data and GPS TEC data are discussed in the following sections.

A 27-day running mean value of F10.7 flux was used in lieu of the daily F10.7 flux value in the PRISM input stream. Based on work done by Pat Doherty, it has been shown that the mean F10.7 correlates much better with the state of the ionosphere than the daily value, either because of the solar EUV has less day-to-day variability than F10.7 or because the day-to-day variability in solar EUV is uncorrelated with the day-to-day variability in F10.7 [*Computational Physics Inc.*, 1996].

3. Ground Truth Data and Real-time Input Data

3.1 Digital Ionospheric Sounding System (DISS) Data

The Digital Ionospheric Sounding System (DISS) is a ground-based network of ionosondes providing observations of ionospheric profile parameters (e.g. foF2 and hmF2). DISS observations are analyzed by computers and recorded digitally.

An ionosonde uses four key properties of the ionosphere to measure profile parameters. First, the electron density increases with height up to the F2 layer peak (see Figure 19). Second, the plasma frequency (the natural resonant frequency of the ionosphere) is a function of electron density:

$$\nu_{\text{plasma}} (\text{kHz}) = 8.97 \sqrt{N_{\text{ec}} (\text{cm}^{-3})} \quad (4)$$

where N_{ec} is the number density of electrons of the layer and ν_{plasma} is the plasma frequency. Therefore, the plasma frequency increases with height up to the F2 layer peak. Third, a vertically-propagating radio wave of frequency ν_{radio} will reflect at the altitude where the radio wave frequency equals the local plasma frequency, because at this level the radio wave causes the local plasma to resonate at its natural oscillating frequency. Last, a conclusion from the second and third properties, low frequencies reflect at lower altitudes where the plasma frequencies (and hence, electron densities) are less; higher frequencies reflect at higher altitudes.

By determining the time, Δt , it takes for a given radio wave to return to the receiver (and assuming some value, c' , for the propagation speed of the radio wave), an altitude, h' , can be determined at which reflection occurred:

$$h' = \frac{c' \cdot \Delta t}{2} \quad (5)$$

By broadcasting a range of frequencies, the number density can be determined (since $v_{\text{plasma}} = v_{\text{radio}}$) as a function of altitude so that the full electron density profile of the ionosphere up to the F2 layer peak can be recovered.

The analysis is complicated by the fact that c' is a function of radio wave refractive index, which itself is a function of N_e , so:

$$N_e(h') = N_e\left(\frac{c' \cdot \Delta t}{2}\right) = N_e(c'(N_e))$$

The computer analysis of the ionosonde data interprets the raw data and, through an iterative scheme, can determine profile parameters. The resulting numerical values are archived at five World Data Centers including the National Geophysical Data Center (NGDC).

3.2 Errors in DISS Data

Digital ionosonde data used in this research has been quality-assured by the NGDC, but there are some questions as to the accuracy of the ionosonde data in general. In a 1990 article in *Advances in Space Research*, J.E. Titheridge challenged the accuracy of ionogram interpretation of hmF2 because of a poor understanding of the size and shape of the valley region between the E and F layers and its effect on ionogram measurements

[Titheridge, 1990]. Titheridge contended ionosonde F2 peak height was being underestimated by as much as 12 km. A study comparing digisonde (computer-scaled ionograms) measurements with incoherent scatter radar (ISR) measurements confirmed Titheridge's theory. The digisonde measurements were lower than the ISR measurements by an average of 4 km in January and 17 km in June. These underestimates were attributed to inversion software correction factors used to model the E-F1 and F1-F2 transition regions [Chen *et al.*, 1994]. Raymond O. Conkright of the National Geophysical Data Center in Boulder, Colorado, countered that the interpretation of an ionogram by trained and knowledgeable people rivaled any other method of measuring the ionosphere. However, most ionograms are scaled by computer programs and are not normally double-checked by technicians, and the data is only as good as the assumptions and quality of the procedure used to estimate ionospheric characteristics (e.g. hmF2). Conkright stated confidence in *averaging* the DISS data to provide a representative ionosphere, which is the method employed in this research [Conkright, 1997].

Our assumption on the accuracy of DISS-measured hmF2 is ± 17 km and ± 0.4 for foF2.

3.3 Global Positioning System (GPS) Total Electron Content (TEC) Measurements

The Global Positioning System (GPS) obtains total electron content (TEC) using a differential delay technique. The satellite broadcasts at two frequencies, 1575.42 MHz and 1227.6 MHz, and a ground based receiver measures the time difference between transmission of the wave and receipt of both frequencies (refer to The Handbook of

Geophysics and the Space Environment, chapter 10, section 8 for an in-depth derivation and discussion of differential carrier phase delay calculations). The measured delay contains contributions from three sources: the ionosphere, the satellite transmitter, and the receiving system including antennas, cables, etc. [Conkright *et al.*, 1997]. The slant-path total electron content (STEC) is derived from the delay, D , in nanoseconds, assuming a thin-shell ionosphere model at height ($h=400\text{km}$) using the following:

$$\text{STEC} = 1.85 \cdot D \quad (6)$$

where STEC is in units of 10^{16} electrons per m^2 .

The STEC is converted into a vertical TEC measurement (because the satellite is not normally directly overhead of the receiver) using:

$$\text{TEC} = \text{STEC} / \text{Sec}[\chi] \quad (7)$$

where χ is the angle between the ray path and the vertical.

Finally, the vertical TEC is corrected for delays associated with individual satellite and receiver biases. The biases used in this research are as follows:

Table 4: Global Positioning Satellite Biases

Satellite Number	Satellite Bias (TEC)	Satellite Number	Satellite Bias (TEC)	Satellite Number	Satellite Bias (TEC)
1	-3.1372	14	-2.5668	23	-1.7112
2	-0.8556	15	-1.7112	24	0.2852
4	-8.8412	16	0.5704	25	-11.1228
5	-5.704	17	-0.5704	26	-8.2708
6	-6.5596	18	-7.4152	27	-5.9892
7	-1.1408	20	-1.7112	28	-9.6968
9	-7.7004	21	-1.9964	29	-12.2636
12	7.9856	22	-4.8484	31	-8.8412

The receiver bias for both Vandenberg, California, and Westford, Massachusetts, was -23.6 TEC units.

3.4 Errors in GPS TEC data

Errors can be introduced into the vertical TEC in at least four ways. First, the conversion from slant TEC to vertical TEC does not take into account horizontal gradients in electron density. In this research, elevation angles of less than 40° were completely excluded from consideration and, furthermore, when two or more satellites gave data for the same hour of observation, the measurement closest to vertical was chosen to minimize this error source. Another density gradient error source is the traveling ionospheric disturbance (TID) which can contribute a ± 0.5 TEC unit difference to GPS TEC measurements [Beach *et al.*, 1997]. Second, satellite and receiver biases may not be accurately estimated. Third, for this research the satellite (Table 4) and receiver corrections were considered constant over the entire twenty-month span of data. This does not consider the effect of maintenance or normal degradation on circuitry, nor changes in temperature in the ground-based receiver. Finally, the ionosphere may not always be adequately represented by the thin shell model which assumes a slab-thickness of 400 km. At night slab thickness can approach 1000 km which can reduce the TEC values by 8% [Davies and Hartmann, 1997]. The overall accuracy of GPS TEC is estimated at ± 2 -3 TEC units [Doherty, 1997; Conkright *et al.*, 1997].

3.5 Chapter Summary

As discussed in Appendix A, the ionosphere has very dynamic characteristics. Measurements of the electron densities, peak heights, and critical frequencies will always be subject to question, but awareness of DISS and GPS weaknesses will provide understanding as to the accuracy of their ionospheric observations. The benefits of the DISS and GPS systems are their ability to quickly provide large amounts of ionospheric data.

4. Results

4.1 Statistical Methodology in Data Analysis

The objective of the statistical analysis is to quantify the accuracy of PRISM with and without ingesting GPS TEC as a real-time input parameter.

There are four statistical methods used in this thesis: mean residual, standard deviation of the mean residual, reduced chi-square, and data averaging.

The mean residual is an estimate of model bias. It is calculated as follows:

$$\bar{e} = \frac{1}{n} \sum_{i=1}^n (m_i - o_i) \quad (8)$$

where n is the number of observations, m is the model calculation, and o is the observed value (DISS). An accurate model will possess little to no bias; a large bias is a strong indication of either (1) an instrument or measurement problem, or (2) a problem with the physical basis of the model. Conversely, a small or zero bias may only mean the model residuals are randomly distributed and does not necessarily imply a more accurate calculation. The mean residual is calculated for each location, for each season, and for each hour, for both foF2 and hmF2.

The standard deviation of the mean residual is calculated as follows:

$$\sigma_e = \sqrt{\frac{1}{n-1} \sum_{i=1}^n (e_i - \bar{e})^2} \quad (9)$$

where σ_e is the standard deviation, n is the number of observations, the quantity squared is the model error for an individual run minus the mean residual calculated for the hour in question. A standard deviation value that is larger than the residual may indicate the model does not have a bias, but instead the mean residual is not representative due possibly to small sample size.

The reduced chi-squared “goodness of fit” test is calculated as follows:

$$\chi^2 = \frac{1}{n-1} \sum_{i=1}^n \frac{(e_i)^2}{o_i} \quad (10)$$

where e_i is the model residual, n is the number of calculations, and o_i is the observed value (DISS data). The reduced chi-square is used only as a comparative statistic to show where the model performs better with or without ingesting GPS TEC as real-time input parameters.

An accurate model will show a reduced chi-square of near one assuming that the statistical assumptions upon which the test is based hold for our experiment [Bevington *et al*, 1992]. The third method is averaging hourly results to show trends for each season. Averaging was accomplished by taking the value of each separate PRISM execution (or DISS data), summing values for each hour, and dividing by the number of calculations /observations.

4.2 Model Bias

All hmF2 mean residuals calculated by month (no hourly distinction) were less than their respective standard deviation, as shown in Table 5. No conclusive remark can be

made as to model bias based on the seasonal calculations of the mean residuals; an hourly calculation was also performed to isolate any particular hour (or time frame) in which a trend can be identified as discussed in the following paragraph. For mean residuals and standard deviations of hmF2 for each hour refer to Tables 14 - 16 in Appendix E.

Table 5: Seasonal hmF2 (km) Mean Residual and Standard Deviation Values

Residual values were calculated as model output minus ground truth data (DISS), so a negative residual (bias) suggests an underestimation and a positive residual suggests an overestimation. The standard deviation values are given in the shaded rows.

	Point Arguello		Wallops Island	
	PRISM/TEC	PRISM/PIM	PRISM/TEC	PRISM/PIM
Equinox	-13.749	-14.325	-0.977	-4.616
	51.707	51.981	31.310	29.479
Summer	9.940	6.237	6.790	2.536
	35.242	35.268	37.957	38.772
Winter	-14.101	-17.152	-9.083	-14.658
	34.005	33.916	35.123	35.564

There were three hourly periods (out of 48 calculations; two stations, 24 hours in a day) which indicate a model bias for equinox hmF2 where the absolute value of the mean residual was higher than the standard deviation. This is not a sufficient argument for showing an overall model bias. For the summer calculations of the mean residual for hmF2, seven out of 48 calculations (14.6%) were greater than the standard deviation suggesting a positive model bias, but once again, not a compelling statistical argument. However, a trend in the winter calculations of the hmF2 mean residual (for both PRISM/TEC and PRISM/PIM) for the evening hours of 20:00L - 04:00L at Wallops Island all showed a negative model bias in which six out of the nine calculations were greater than their standard deviations. The winter hmF2 mean residuals for Point

Arguello also showed a negative model bias for the 20:00L - 04:00L time frame, but all but one were less than the standard deviation.

The foF2 seasonal mean residuals (Table 6) shows an overall positive model bias for PRISM/TEC at Wallops Island for all seasons. At Point Arguello, only the summer mean residual exceeds the standard deviation allowing for a positive model bias conclusion. This suggests PRISM/TEC overestimates foF2 for all seasons at Wallops Island and for summer at Point Arguello. An overestimation in the foF2 measurements is not unexpected. The RTA takes what is an overestimation of electrons in the ionosphere (due to the topside/plasmaspheric electrons content in the GPS TEC measurement) and increases the model output to coincide with what the GPS total electron count is representing as all ionospheric electrons.

There are at least three possible reasons why equinox and winter foF2 mean residual/standard deviation comparisons do not support a positive model bias conclusion. First, an underestimation of a (satellite or receiver) bias correction factor exactly compensates for the additional electrons present in the GPS measurement so that the net effect is zero. Second, PIM exhibits a sufficiently large negative error for equinox and winter to counter the contributions to the GPS TEC measurements by the topside/plasmaspheric electrons. Last, topside/plasmaspheric electrons do not contribute enough to the GPS TEC measurements during winter and equinox to show a positive bias. Since only the first of these three reasons is dependent on location, and the positive bias was indicated only for Wallops Island, we question the accuracy of the GPS receiver bias at Vandenberg, California.

Table 6: Seasonal foF2 (MHz) Mean Residual and Standard Deviation Values

Residual values were calculated as model output minus ground truth data (DISS), so a negative residual (bias) suggests an underestimation and a positive residual suggests an overestimation.

	Point Arguello		Wallops Island	
	PRISM/TEC	PRISM/PIM	PRISM/TEC	PRISM/PIM
Equinox	0.537	-0.215	1.162	-0.140
	1.047	1.167	1.158	0.864
Summer	2.045	0.255	1.356	0.184
	1.463	0.839	0.858	0.851
Winter	0.239	-0.855	1.827	0.227
	1.635	1.204	0.756	1.771

An examination of the hourly mean residual/standard deviations for foF2 in Tables 17-19 (Appendix E) shows Wallops Island mean residuals for PRISM/TEC are larger than the standard deviation for 79% of hours calculated for equinox, winter, and summer. Point Arguello calculations do not show the consistent positive bias in foF2 throughout the seasons as seen with Wallops Island calculations. In the summer Point Arguello calculations showed the only consistent positive bias: the mean residuals were larger than the standard deviation for every hour except 8:00L and 9:00L. However, these two hours still had mean residuals of +1.454 and +1.274 respectively, confirming the seasonal positive model bias calculations.

4.3 Goodness of Fit Test

Reduced chi-square model goodness of fit values for hmF2 and foF2 (both PRISM/PIM and PRISM/TEC) are given in Appendix E. These values are normalized to one; if the model performed perfectly (exactly matching the DISS data) for the hour

calculations examined, the reduced chi-square value would be zero (which is statistically unlikely).

The hmF2 reduced chi-square calculations for PRISM/PIM and PRISM/TEC should be identical because ingesting GPS TEC measurements should not cause the RTA to adjust heights. However, we do see minor differences in every season; this will be explained in the next section.

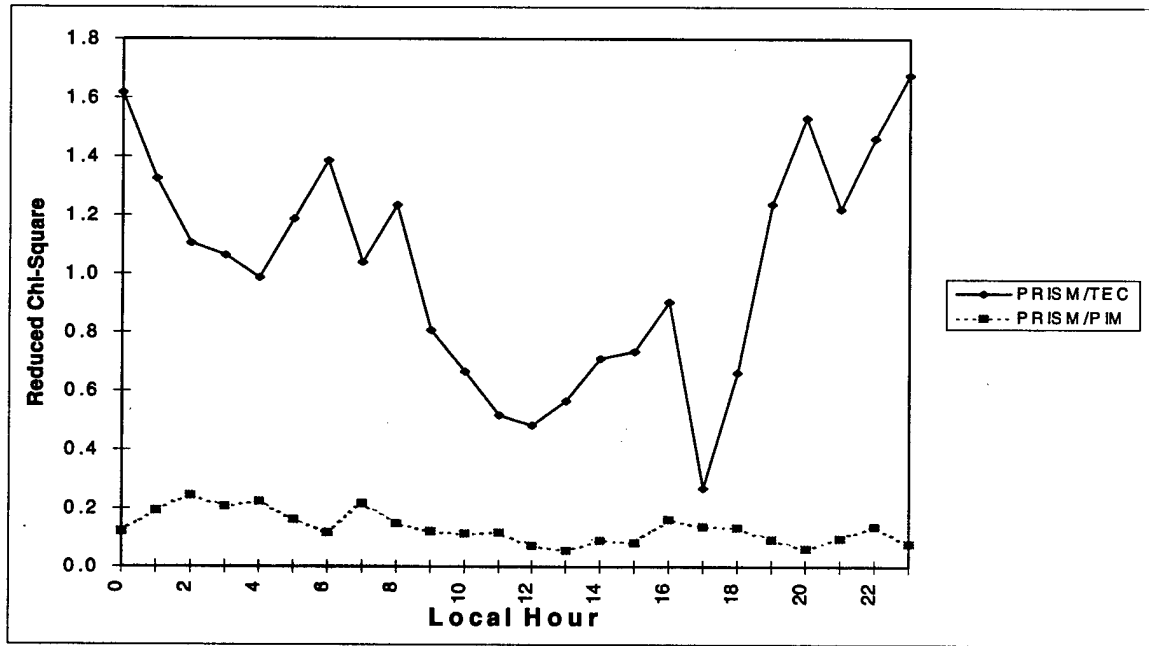


Figure 5: Wallops Island Reduced Chi-Squared for Winter foF2

Patterns in the foF2 reduced chi-square calculations are evident (See Figure 5).

Values for the reduced chi-square are sometimes less than one. This is a result of subtracting DISS values so close to those of PRISM/PIM that the difference was less than one MHz, and when squared for the chi-square calculation, is still less than one.

PRISM/PIM reduced chi-square numbers showed a better model fit than PRISM/TEC over all times and seasons with the exception of 10:00L - 19:00L during Equinox and

07:00L - 08:00L in winter at Point Arguello. PRISM/PIM's better fit is expected, because the additional topside/plasmaspheric electron contribution to the GPS TEC measurements would cause the foF2 calculations by PRISM/TEC to be high.

Table 7: Point Arguello foF2 Reduced Chi-Square Rank By Hour

	0	1	2	3	4	5	6	7	8	9	10	11	12	13	14	15	16	17	18	19	20	21	22	23
Equinox																								
PRISM/TEC	3	2	2	2	2	2	2	2	1	1	1	1	1	1	1	1	1	1	1	1	2	2	2	2
PRISM/PIM	3	1	1	1	1	1	1	1	1	1	1	1	1	1	1	1	2	1	1	1	1	1	2	1
Summer																								
PRISM/TEC	3	3	3	3	3	3	3	3	3	3	3	2	3	3	2	2	3	3	3	3	3	3	3	3
PRISM/PIM	1	1	1	1	1	1	1	1	1	2	1	1	1	1	1	2	1	1	1	1	1	1	1	1
Winter																								
PRISM/TEC	3	3	3	2	3	3	3	2	2	1	2	2	1	1	1	2	2	2	3	3	3	3	3	3
PRISM/PIM	2	2	2	2	2	2	2	2	2	1	1	1	1	1	1	1	1	1	2	1	1	2	2	2

Table 8: Wallops Island foF2 Reduced Chi-Square Rank By Hour

	0	1	2	3	4	5	6	7	8	9	10	11	12	13	14	15	16	17	18	19	20	21	22	23
Equinox																								
PRISM/TEC	3	3	3	3	3	3	3	3	2	2	2	2	1	2	1	1	1	1	1	2	2	3	3	3
PRISM/PIM	1	1	1	1	1	1	1	1	1	1	1	1	1	1	1	1	1	1	1	1	1	1	1	1
Summer																								
PRISM/TEC	3	3	3	3	3	3	3	2	2	1	1	1	1	2	2	2	2	3	2	2	2	2	3	2
PRISM/PIM	1	1	1	1	1	1	1	1	1	1	1	1	1	2	2	1	1	1	1	2	1	1	1	1
Winter																								
PRISM/TEC	3	3	3	3	3	3	3	3	3	3	2	2	2	2	3	3	3	1	2	3	3	3	3	3
PRISM/PIM	1	1	1	1	1	1	1	1	1	1	1	1	1	1	1	1	1	1	1	1	1	1	1	1

In the Tables 7 and 8, the reduced chi-square calculations are ranked to indicate goodness of fit; "1" is a excellent fit, "2" is a good fit, "3" is a fair fit, and "4" is a poor fit. PRISM/PIM has a better or equal rank for nearly all hours at both locations for all seasons.

4.4 Averaged Model Output

The results of the PRISM executions (PRISM/PIM, PRISM/TEC, PRISM/corTEC) and the ground truth data (DISS) have been averaged for each hour and presented by season to indicate seasonal and temporal trends and features in both the model output and the ionosonde data.

Figures 6 and 7 show the averaged hmF2 (km) values for equinox at Point Arguello and Wallops Island respectively. A common feature at both locations is PRISM/TEC's underestimation of hmF2 from 23:00L through 4:00L by as much as 35 km.

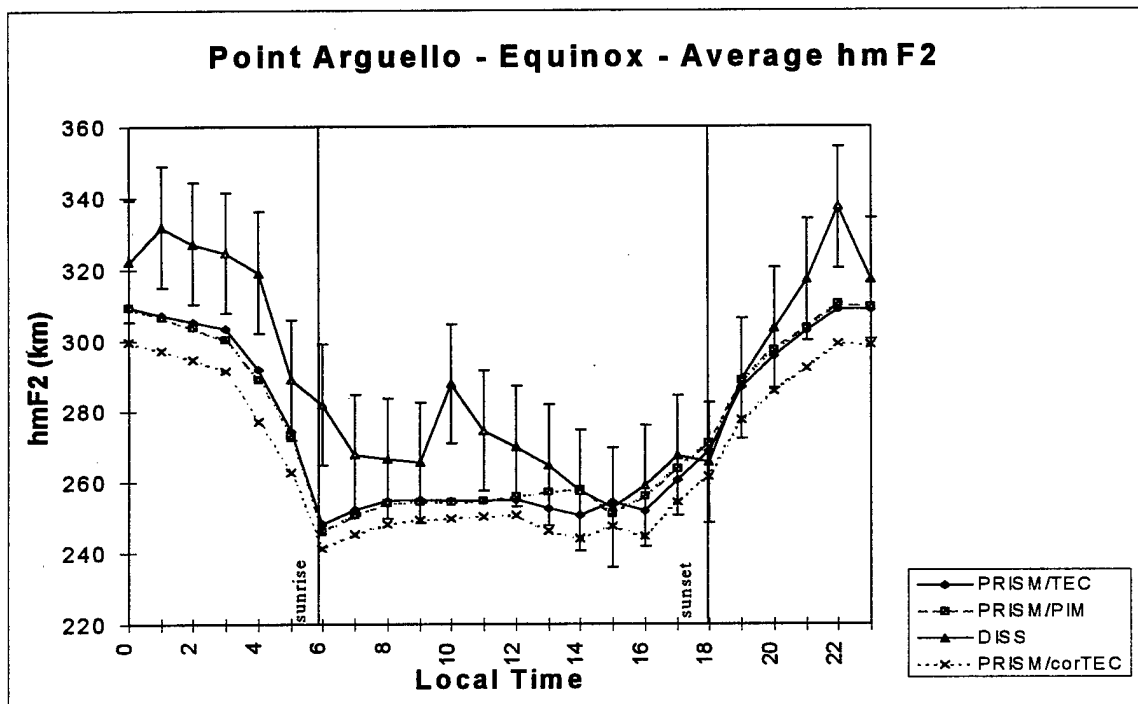


Figure 6: Point Arguello Average hmF2 at Equinox

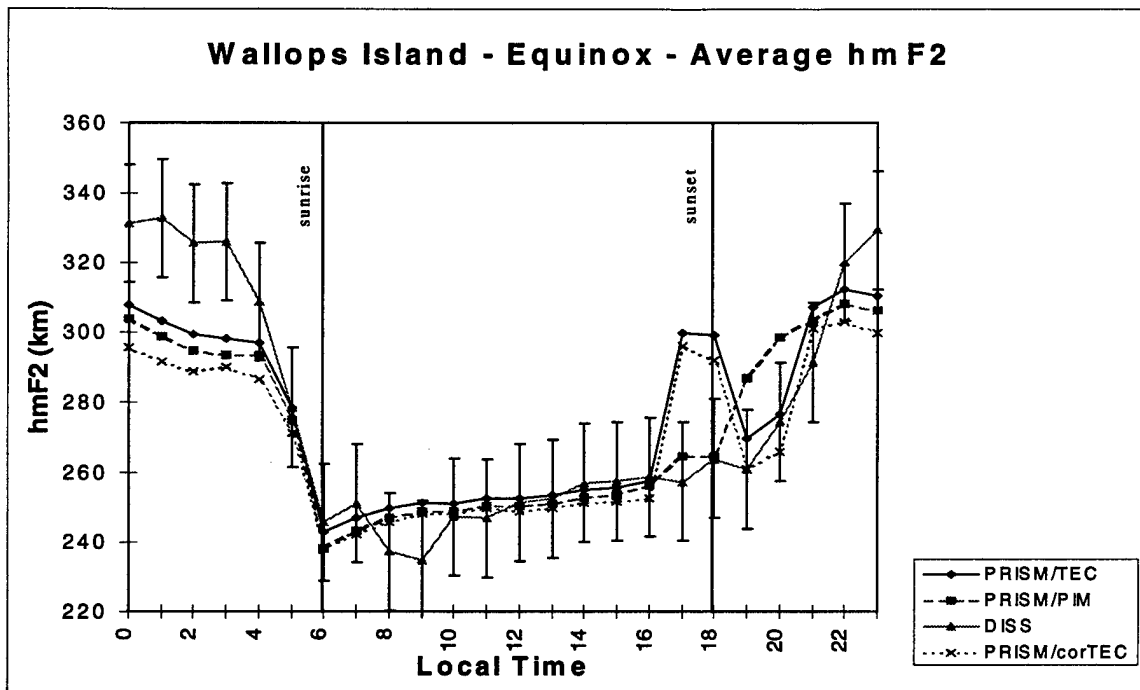


Figure 7: Wallops Island Average hmF2 at Equinox

A surprising result in the hmF2 calculations is the higher hmF2 calculated by PRISM/TEC as compared to PRISM/PIM. The values of hmF2 should be identical for both executions of PRISM because the TEC measurements only affect the RTA's adjustment of number density of the F2 layer (affecting foF2 calculations), not the height of the F2 layer. Computational Physics Inc. has already identified this problem in the RTA, occurring when there is a 'significant' difference between the model E and F2 layer peak densities. The problem in the RTA will be corrected in PRISM version 1.7c [Brown, 1997].

Another interesting feature in the Wallops Island hmF2 (Figure 7) is PRISM's attempt to indicate a pre-sunset rise in hmF2 which seems to mimic the more familiar "pre-reversal enhancement" in equatorial vertical plasma drifts around sunset. A pre-

reversal enhancement is a brief duration surge in the eastward electric field before local sunset which will cause the F-layer plasma to be driven to higher altitudes via the $\mathbf{E} \times \mathbf{B}$ drift mechanism. This result is unexpected here because a pre-reversal enhancement is an equatorial (magnetic) latitude phenomenon (Wallops Island is a geomagnetic mid-latitude station) and does not usually appear during equinox and solar minimum conditions [Heelis *et al.*, 1979]. As explained in a private communication with Lincoln Brown at CPI, this is actually not an attempt by PRISM to model a pre-reversal enhancement, but is an intensification of the RTA hmF2 height adjustment problem discussed in the second paragraph. Recombination dominates after sunset and occurs more rapidly at E region altitudes, causing the difference between the peak density of the E and F2 layer to increase, resulting in the amplification of the RTA hmF2 height adjustment problem [Brown, 1997] .

In winter (Figures 8 and 9) and during equinox (Figures 6 and 7) at both Point Arguello and Wallops Island, PRISM (with or without real-time input parameters) underestimates hmF2 in the nighttime hours (22:00L - 04:00L) by as much as 35 km. Perhaps PRISM (more specifically HWM90) does not adequately model the component of the neutral wind along geomagnetic field lines. The equatorward, upward component of the neutral wind moves electrons along the geomagnetic field lines in the mid-latitudes, which raises the height of the F2 peak in the evening hours to a level where the neutral molecular concentration and resultant recombination rate are an order of magnitude lower than during the daytime [Tascione, 1992].

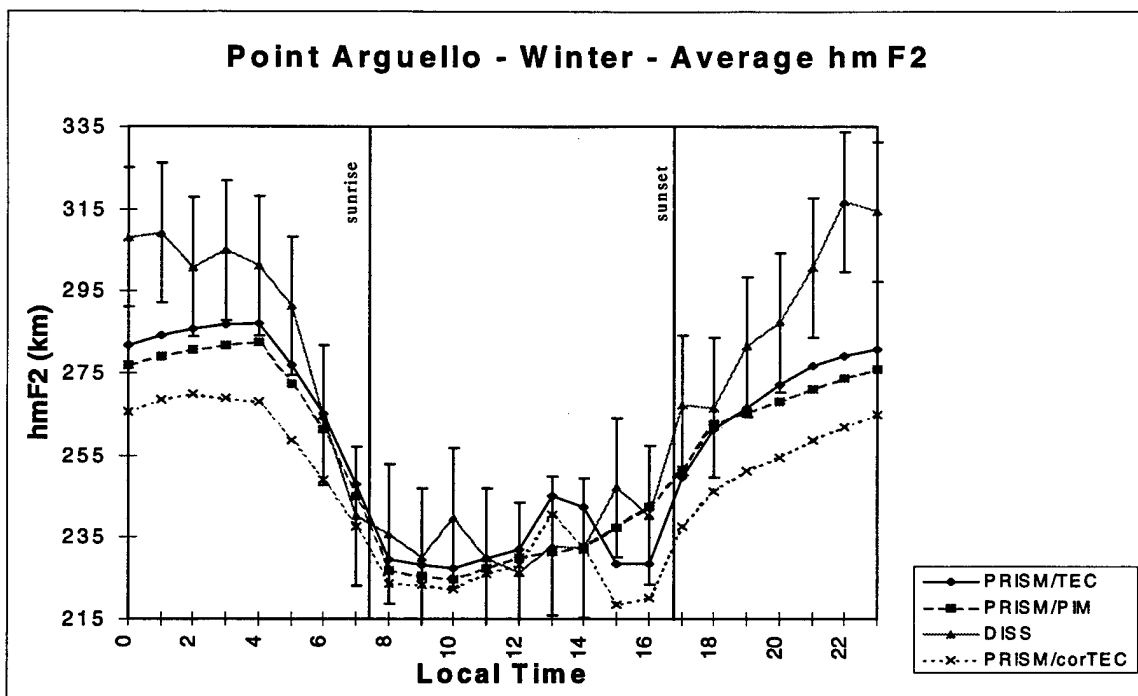


Figure 8: Point Arguello Average Winter hmF2

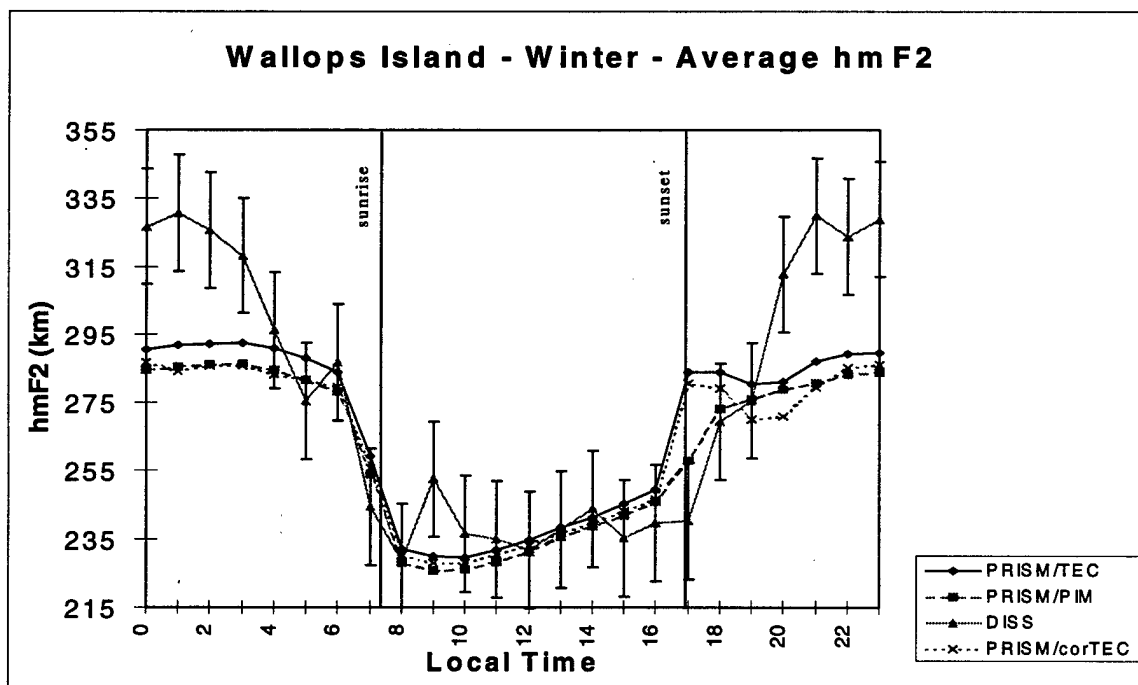


Figure 9: Wallops Island Average Winter hmF2

In analyzing critical frequency, PRISM/TEC overestimated foF2 by 1.5 to 2 MHz (as seen in Figures 10 and 11). The theoretical climatological basis for PRISM, PIM, performs better than (or equally as well as) PRISM/TEC in calculating foF2. In fact, PRISM foF2 values are significantly more accurate without GPS TEC input as evidenced in the winter foF2 plots (Figure 11) as well as in Figures 37 - 39 in Appendix F. PRISM/PIM more accurately specifies foF2 during summer and winter than does PRISM/TEC; differences in equinox specifications of foF2 are less noticeable.

Why would PRISM/PIM provide a more accurate foF2 than PRISM/TEC? When the RTA ingests a TEC value it adjusts the number densities to match the real-time input, which is taken to be a true representation of *ionospheric* free electron content. The TEC measurement, however, measures not only ionospheric but also plasmaspheric electrons, because the GPS satellite orbits well above the top of the ionosphere (22,000 km). PRISM only models the topside of the ionosphere as an O⁺ profile, not taking into account those free electrons with origins from the light ions, nor any free electrons above the ionosphere (in the plasmasphere). When the RTA adjusts the density (and the foF2) of each layer, it actually overcompensates because the GPS TEC value is too large by the contribution from the topside/plasmaspheric electrons. To lessen the overestimation of foF2 by PRISM/TEC requires one to correct the GPS TEC measurements before they are ingested into the RTA, which is discussed in the next paragraph.

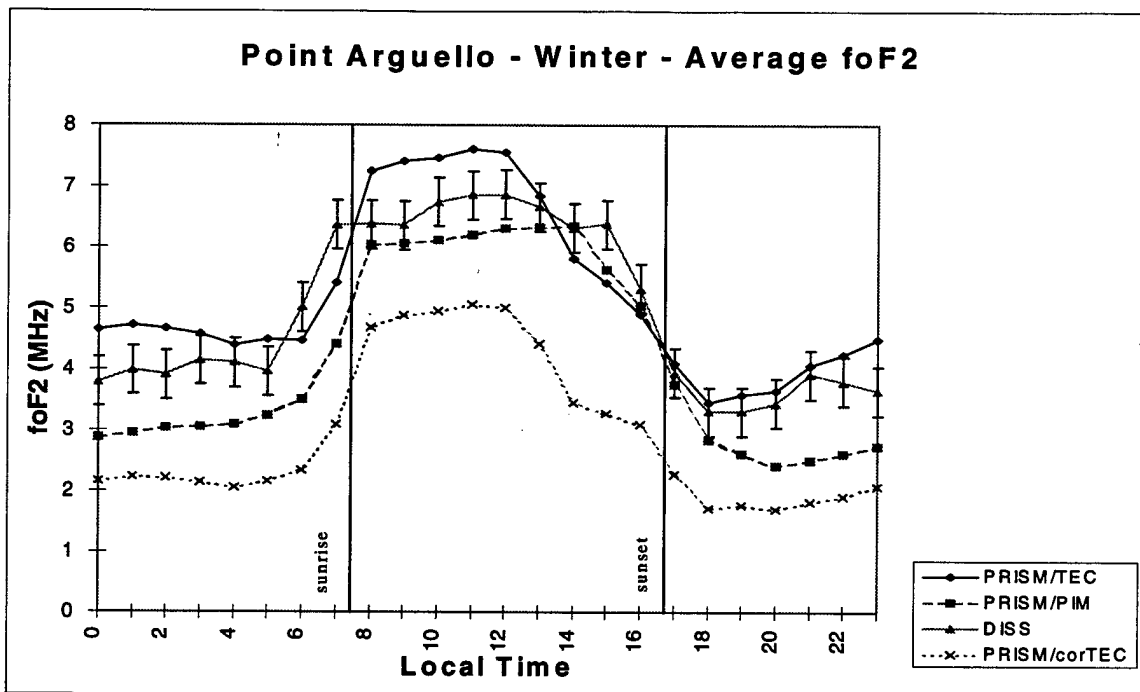


Figure 10: Point Arguello Average Winter foF2

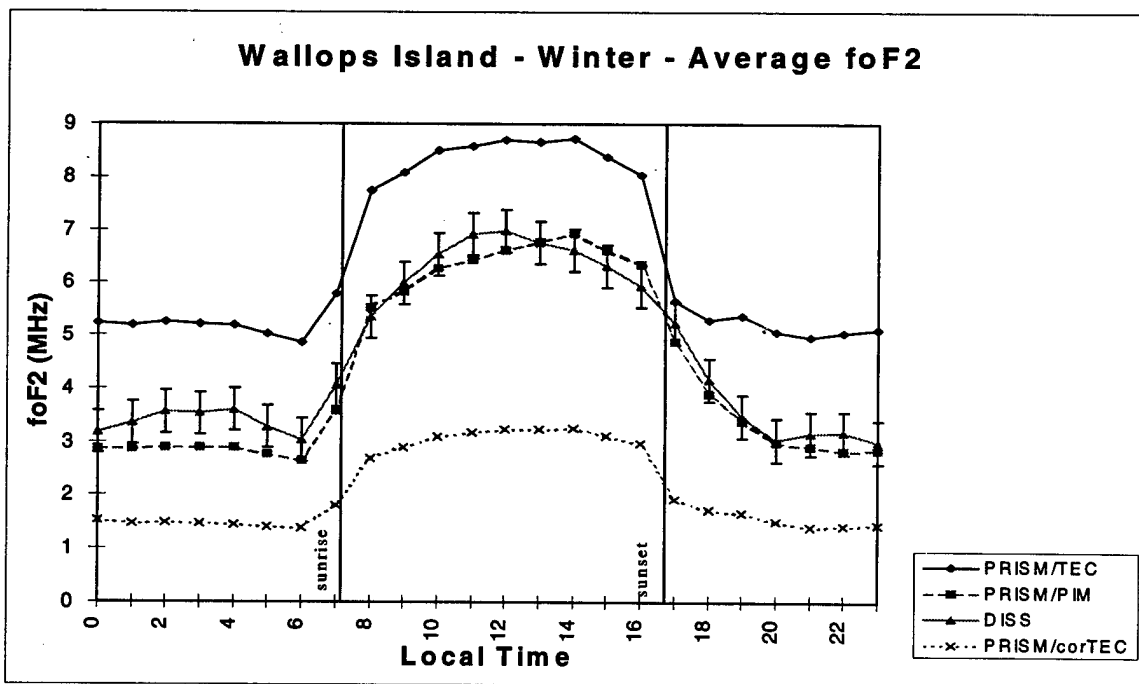


Figure 11: Wallops Island Average Winter foF2

4.5 Possible Influence of Topside/Plasmaspheric Electrons on Error Analysis

In Figures 6 - 12 the averaged values of hmF2 and foF2 when GPS TEC values are reduced by four TEC units (to account for topside/plasmaspheric electrons [Anderson, 1997]) are labeled in the figures as "PRISM/corTEC." This correction increases the underestimation of hmF2 on average by 5 km during the late evening/early morning hours for all seasons. Without the correction factor, PRISM/TEC overestimated foF2 values for all seasons; with the 'correction' of four TEC units, the model becomes biased in the opposite sense for all seasons except for equinox at Wallops Island where the bias is approximately zero, shown below in Figure 12.

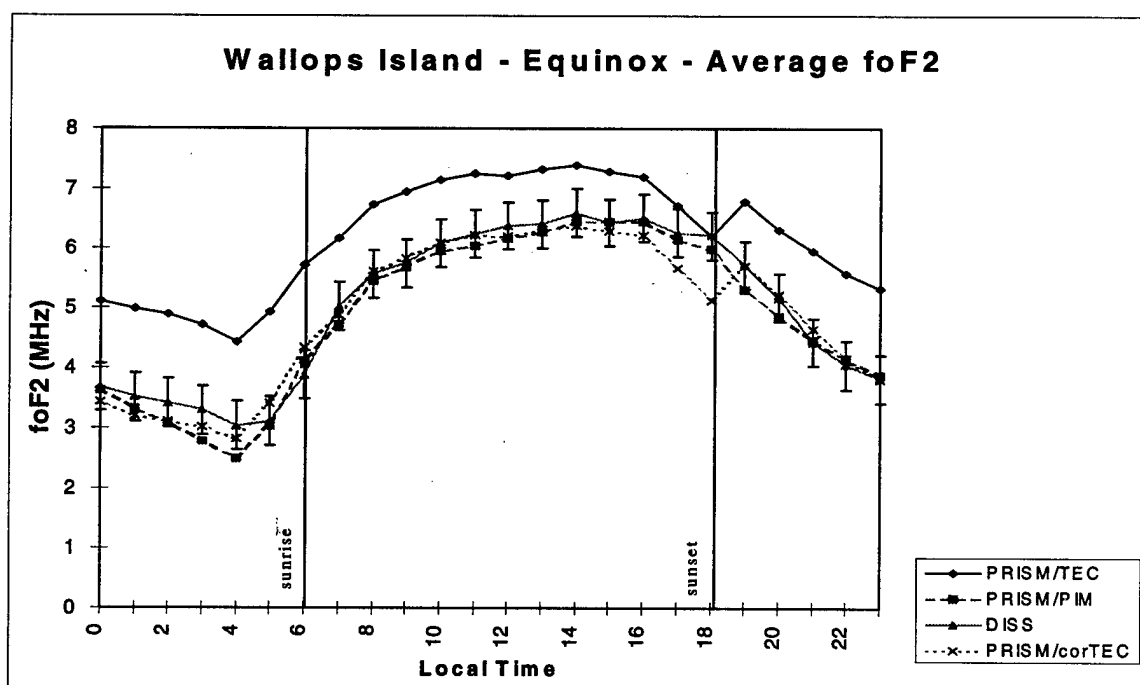


Figure 12: Wallops Island Average foF2 at Equinox

The correction factor of four TEC units, too high by one or two TEC units for the summer and winter season, adequately corrected TEC real-time parameters for foF2

during equinox at Wallops Island. This suggests there may be a seasonal variation in the topside/plasmaspheric electron content. A correction term of two or three TEC units for ingested GPS TEC measurements might more accurately adjust calculations of hmF2 and foF2 in summer and winter (solstices). Using the International Reference Ionosphere (IRI) model to provide a better estimation of topside/plasmaspheric electron content would account for the seasonal and hourly variations in their contributions to TEC.

A better solution is to model the topside/plasmaspheric electrons instead of correcting for them. The Sheffield University Plasmasphere Ionosphere Model (SUPIM) accounts for O^+ , H^+ , He^+ , N_2^+ , O_2^+ , and NO^+ , which is a more complete representation of the topside ionosphere and plasmasphere than PIM's current model of an O^+ topside and no model for the plasmasphere. SUPIM is a time-dependent, physical model for the Earth's mid- and low-latitude ionosphere and plasmasphere [Bailey *et al*, 1997]. This model uses the same tilted dipole magnetic field assumptions and inputs from some of the same empirical models (e.g. HWM90 and the Plasma Drift Model) at TDIM. The accuracy of future versions of PRISM might benefit from the modeling of the topside/plasmaspheric electrons rather than estimating a correction factor to account for them.

The advantage to real-time input parameters is the ability to capture temporal and spatial variability in the ionosphere. The real-time input parameters help delineate small time scale or local phenomenon that would be otherwise missed by a purely theoretical model (e.g. PIM) because the theoretical models tend to 'smooth' small scale features.

4.6 Influence of Geomagnetic Activity

The influence of geomagnetic activity is presented in this thesis for two seasons, Equinox and Winter at Point Arguello. These two seasons were chosen because they represented an adequate statistical basis for comparison; other seasons were excluded from this analysis because some geomagnetic activity categories were either not represented in the data set or too few cases were available for comparison. To distinguish geomagnetic activity, the daily geomagnetic index C9 was used. The C9 index is a conversion of the Planetary Daily Character Figure, a qualitative estimate of the overall level of magnetic activity for the day, to a scale from 0 to 9. Three categories were established: low geomagnetic activity ($0 \leq C9 \leq 2$), median geomagnetic activity ($3 \leq C9 \leq 5$), and high geomagnetic activity ($6 \leq C9 \leq 9$).

The mean residuals for low, median, and high geomagnetic activity are included in the two tables below:

Table 9: Point Arguello Equinox hmF2 Mean Residual and Standard Deviation by Geomagnetic Activity

Note: The mean residual is located in non-shaded rows and standard deviation in the shaded rows.

Geomagnetic Activity	PRISM/TEC	PRISM/PIM
Low	-8.539	-12.465
	54.695	55.219
Median	-7.200	-10.338
	43.451	46.720
High	-16.684	-13.716
	45.652	45.606

Table 10: Point Arguello Equinox foF2 Mean Residual and Standard Deviation by Geomagnetic Activity

Note: The mean residual is located in non-shaded rows and standard deviation in the shaded rows.

Geomagnetic Activity	PRISM/TEC	PRISM/PIM
Low	0.907	-0.689
	1.173	1.181
Median	0.560	-0.327
	0.980	1.208
High	0.586	0.218
	0.912	1.262

Neutral winds and electric fields greatly affect the altitude and number densities of the F2 layer in the mid-latitudes. Geomagnetic storms enhance the electric fields forcing hmF2 to rise in altitude and exhibit a greater degree of diurnal variability (as much as 165 km). Number density (and consequently foF2), also shows a large degree of fluctuation during geomagnetic storms (as much as 5.5 MHz). During a geomagnetic storm molecular nitrogen and oxygen move up into the F2 region and decrease the available atomic oxygen (which is a primary source of photoelectrons), resulting in a decrease in electron density [Kelley, 1989, Tascione, 1994].

The Point Arguello PRISM/TEC foF2 standard deviation decreases from the low geomagnetic activity case to the high geomagnetic activity case during equinox, while the PRISM/PIM foF2 standard deviation shows a slight increase. As expected, PRISM models the temporal variability slightly better when ingesting GPS TEC as a real-time input parameter. The increase in temporal variability in both hmF2 and foF2 is seen in the DISS data during the high geomagnetic activity case (Figures 14 and 16) when compared to the low geomagnetic activity case (Figures 13 and 15). Some of the

apparent variability in the high variability cases can be attributed to fewer days with high geomagnetic activity as compared to low geomagnetic activity which, when averaged, would not be as 'smooth.'

An interesting feature can be seen in Figure 16 where the average values of foF2 are plotted for high geomagnetic activity. These plots are unique in this thesis, as the PRISM/PIM foF2 values shown here are higher than the PRISM/TEC values for the daylight hours. This indicates PIM does not correctly model a reduced number density (and consequently foF2) during periods of daytime high geomagnetic activity (the PRISM/TEC result reveals that the RTA is making a negative adjustment to foF2 when ingesting GPS TEC values). Further study into the overestimation of foF2 by PIM during equinox daylight hours with high geomagnetic activity is warranted.

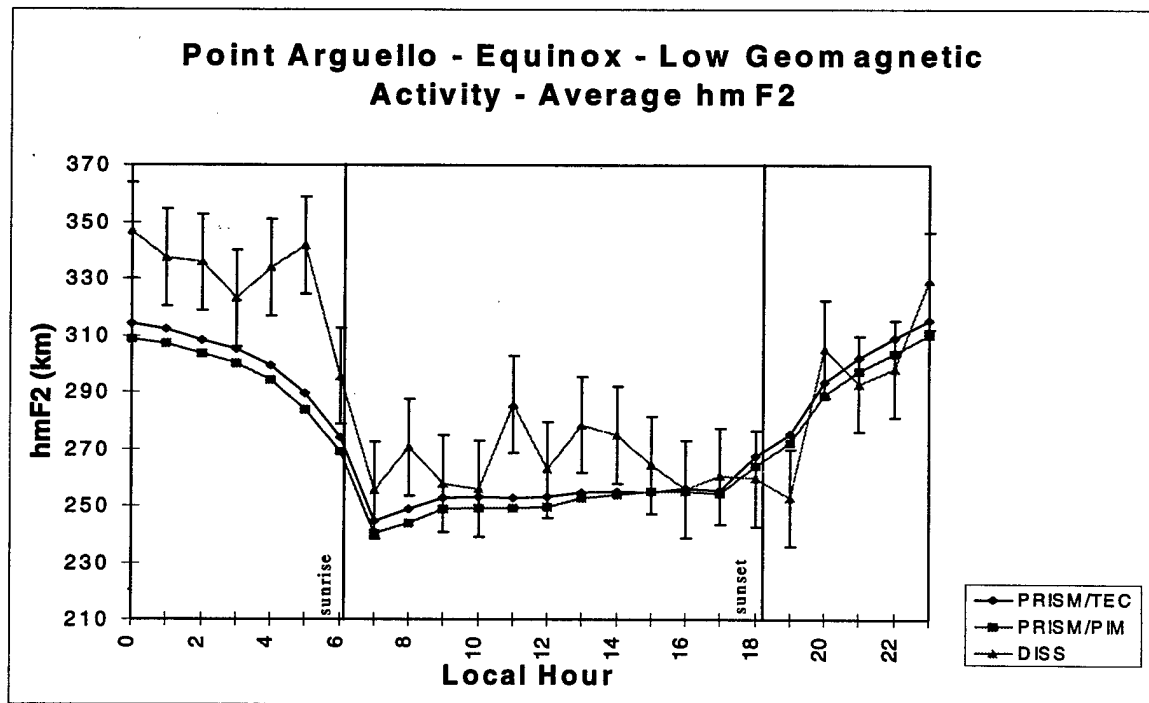


Figure 13: Point Arguello Equinox hmF2 for Low Geomagnetic Activity

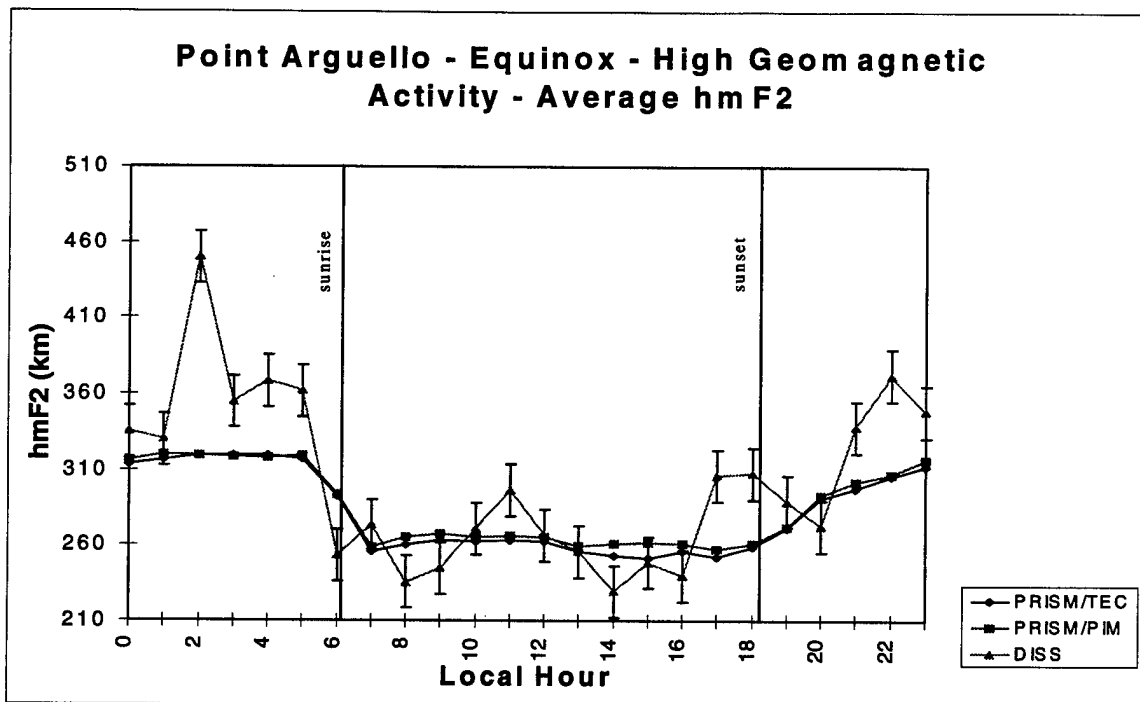


Figure 14: Point Arguello Average Equinox hmF2 for High Geomagnetic Activity

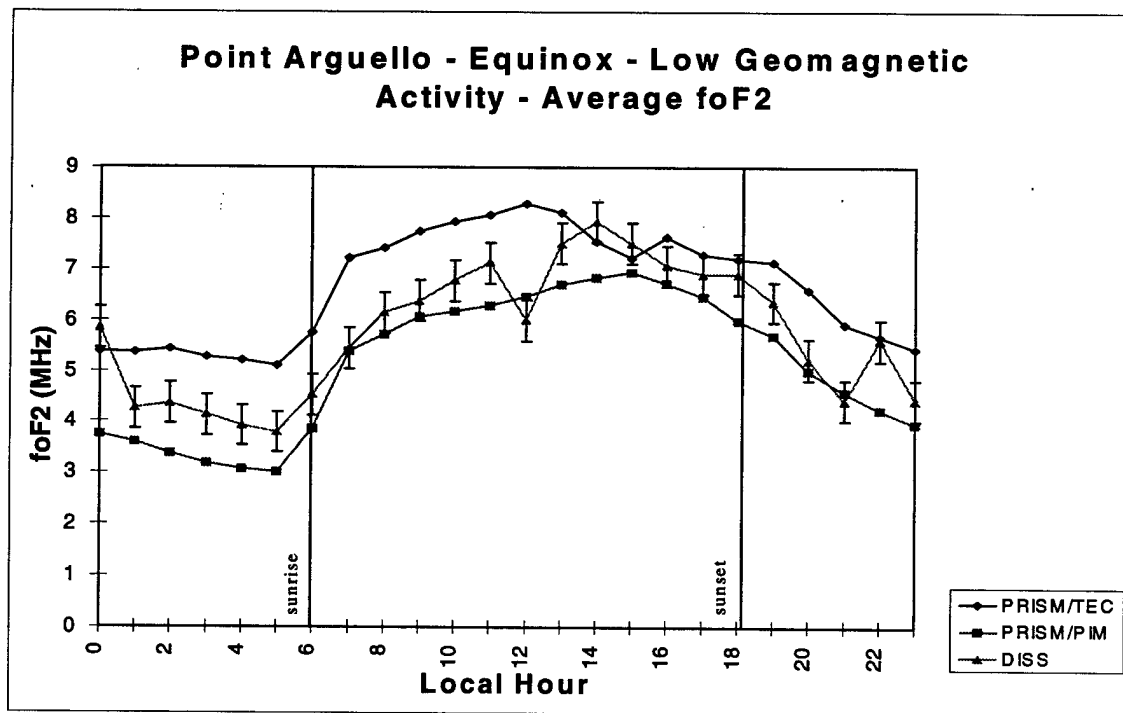


Figure 15: Point Arguello Average Equinox foF2 for Low Geomagnetic Activity

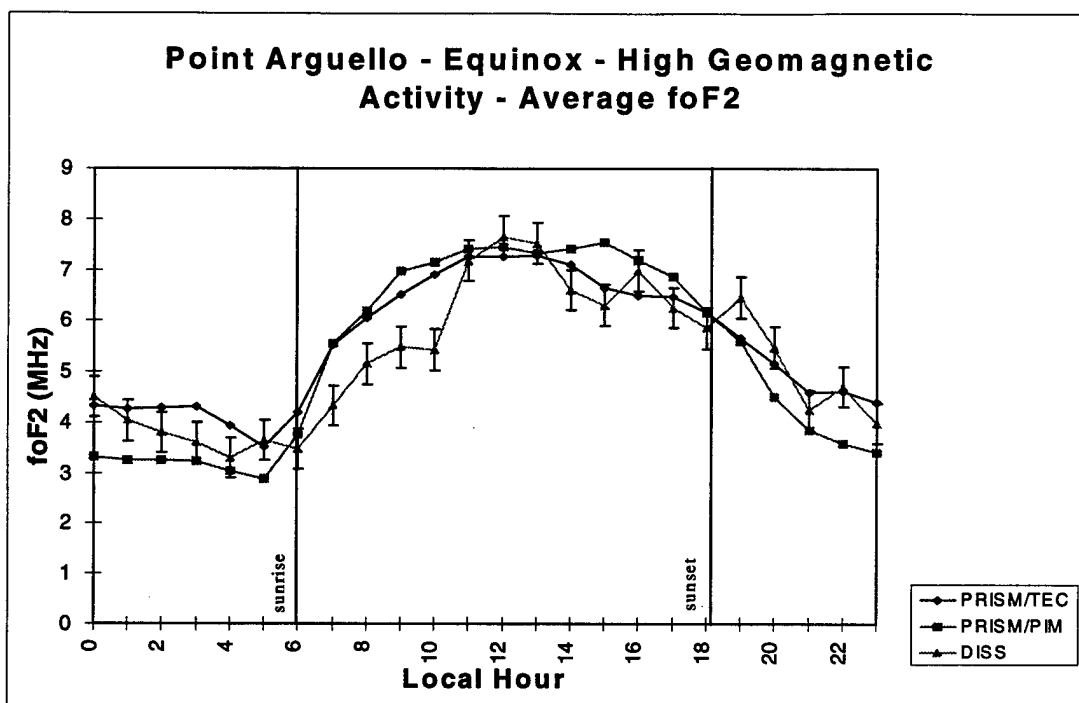


Figure 16: Point Arguello Average Equinox foF2 for High Geomagnetic Activity

Also during the high geomagnetic activity case at Point Arguello (equinox), PRISM/PIM shows higher values (on average 5-10 km) for hmF2 than PRISM/TEC. This may be associated with the problem of the RTA adjusting hmF2 when ingesting GPS TEC. This feature should disappear once the RTA adjustment problem is resolved.

The statistical analysis of effects of winter geomagnetic activity is similar to the equinox analysis on the following page:

Table 11: Point Arguello Winter hmF2 Mean Residual and Standard Deviation by Geomagnetic Activity

Note: The mean residual is located in the non-shaded rows and the standard deviation in the shaded rows

Geomagnetic Activity	PRISM/TEC	PRISM/PIM
Low	-13.375	-17.482
	30.023	29.911
Median	-19.160	-20.081
	40.726	40.470
High	0.674	-0.762
	17.587	17.921

Table 12: Point Arguello Winter foF2 Mean Residual and Standard Deviation by Geomagnetic Activity

Note: The mean residual is located in the non-shaded rows and the standard deviation in the shaded rows

Geomagnetic Activity	PRISM/TEC	PRISM/PIM
Low	0.471	-0.898
	1.702	1.193
Median	0.022	-0.499
	1.255	0.983
High	-1.220	-1.776
	0.712	0.780

Winter (Figure 18) displays similar overestimation of foF2 by PIM except the period of overestimation is near sunset (14:00L - 19:00L). The higher values for PRISM/PIM as compared to PRISM/TEC are also noted for the same period during median geomagnetic activity (Figure 17).

PRISM/TEC shows a positive foF2 mean residual for all seasons when geomagnetic activity differences were neglected (Table 6, page 31). However, the mean residual for PRISM/TEC winter foF2 during high geomagnetic activity is negative indicating PIM so greatly underestimates foF2, the contributions from the topside/plasmaspheric electrons can not compensate for the underestimation. During equinox, PIM overestimates foF2

during daylight hours and high geomagnetic activity (as evident in higher PRISM/PIM foF2 than PRISM/TEC) and underestimates foF2 in winter during high geomagnetic activity. The effects of high geomagnetic activity on PIM foF2 calculations needs to be studied.

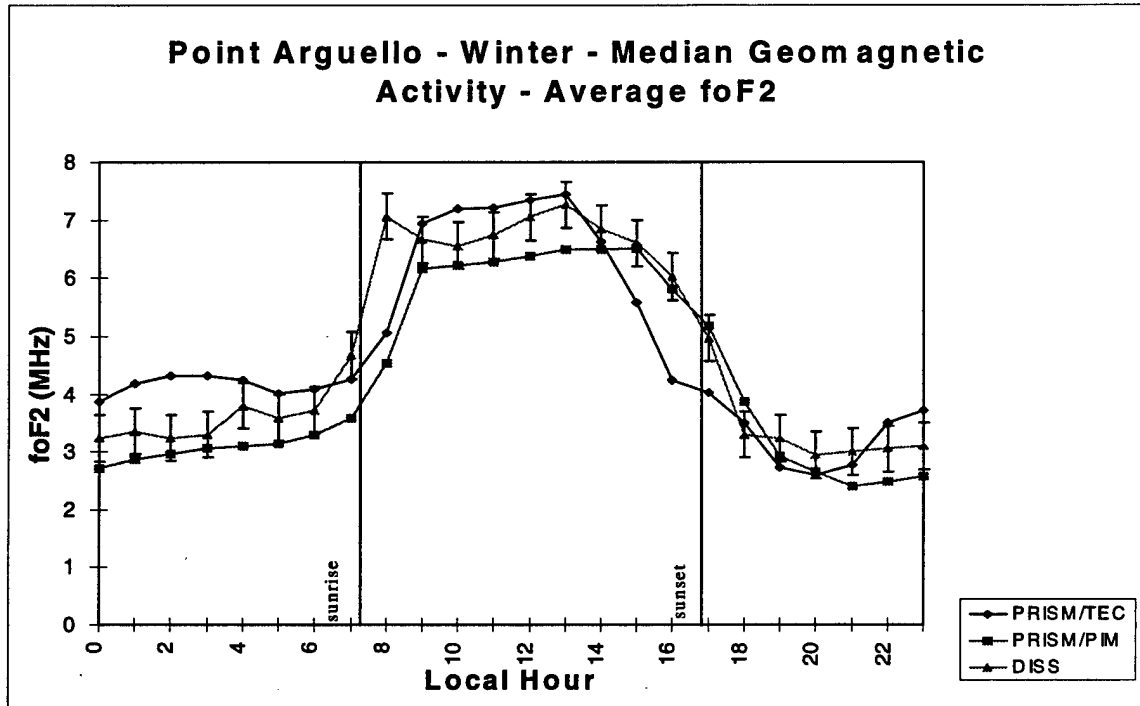


Figure 17: Point Arguello Average Winter foF2 for Median Geomagnetic Activity

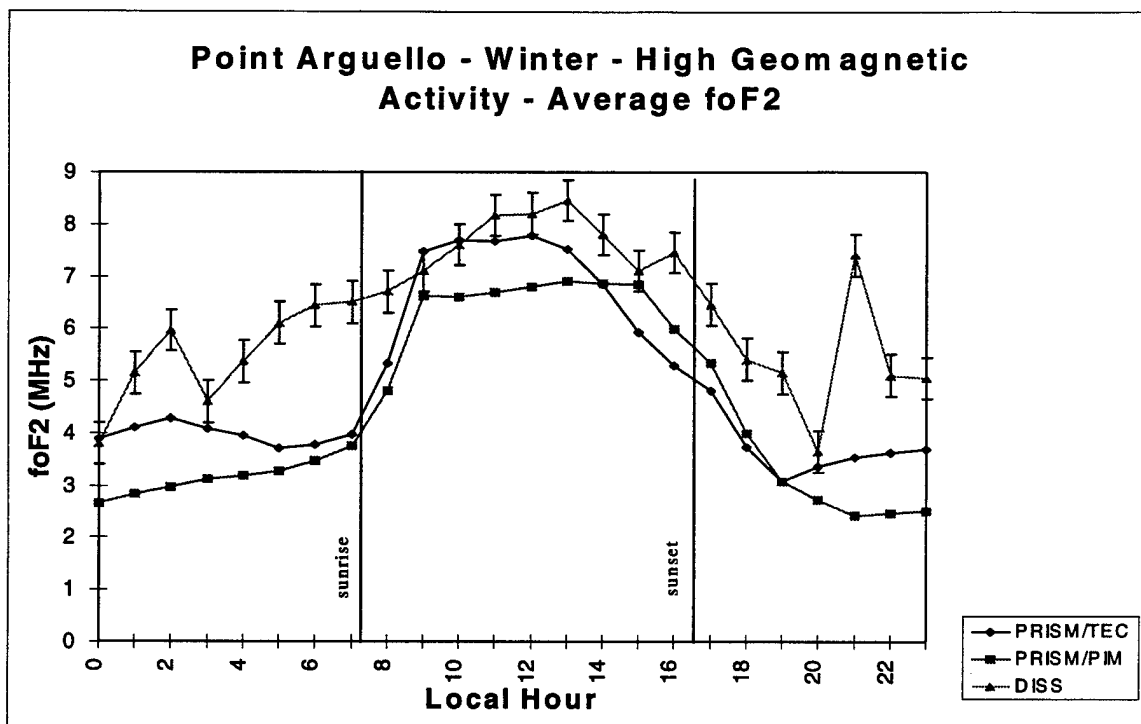


Figure 18: Point Arguello Average Winter foF2 for High Geomagnetic Activity

5. Conclusions and Recommendations

5.1 Summary

The objective of this research was to validate PRISM when driven by Global Positioning System (GPS) measurements of TEC. The scope of the research was intended to provide an hourly measure of accuracy of PRISM/TEC in mid-latitudes as a function of season and geomagnetic activity under conditions of solar minimum. The subtraction of four TEC units from all GPS measurements was suggested by Dr. David Anderson of the United States Air Force Phillips Laboratory at Hanscom AFB, Massachusetts [Anderson, 1997]. This correction was to account for the topside/plasmaspheric electrons measured by GPS from its 22,000 km orbit. The correction was necessary because the physical models in PRISM do not account for any topside/plasmaspheric electrons produced by photoionization of the light elements H and He and only consider the upper ionosphere as a profile of O^+ .

The purpose of the Parameterized Real-time Ionospheric Specification Model (PRISM) is to provide the Department of Defense with an accurate, real-time specification of the global ionosphere. PRISM accomplishes this by using a Real-Time Adjustment (RTA) algorithm to combine real-time observations with a theoretical climatological database, the Parameterized Ionospheric Model (PIM). The real time observations can come from three sources: instruments measuring Total Electron Content (TEC) (e.g. Global Positioning System satellites, polarimeters, and TOPEX), satellites capable of *in situ* measurements (e.g. DMSP), and ionospheric sounding

systems (e.g. Digital Ionospheric Sounding System (DISS), lidar, Incoherent Scatter Radar). Real-time input parameters include: TEC; ion drift velocities; *in situ* number density; ion/electron temperatures; fractional He^+ , H^+ , and O^+ content; mean electron and ion energies; electron and ion energy fluxes and their standard deviations; ionospheric layer critical frequencies (foF2, foF1, and FoE); and peak electron density heights (hmF2, hmF1, and hmE). Planetary geomagnetic values (daily and 90-day average K_p values), Interplanetary Magnetic Field (IMF) values (B_z and B_y), and the measure of the 10.7 cm solar flux (F10.7) are also required by PIM, the physical models upon which PRISM is based.

The scope of this thesis was limited to only two geographic locations (Wallops Island, Virginia, (37.9N 284.5E), and Point Arguello, California, (35.6N, 239.4E)) because of the requirement for the GPS receiver to be in close proximity to the DISS stations used as ground truth (Westford, Massachusetts, (42.9N, 280.0E) and Vandenberg, California, (37.8N, 284.5E) respectively). PRISM was executed twice; first with no real-time input parameters (PRISM/PIM), and second, with the GPS TEC as the sole input parameter (PRISM/TEC). The calculated critical frequency of the F2 layer (foF2) and the altitude of the electron density peak of the F2 layer (hmF2) were then compared with the coincident DISS measurements. These comparisons were made as a function of hour and season for each of the two locations. In addition, two seasons (Point Arguello winter and equinox) were analyzed as a function of hour and geomagnetic activity based on the geomagnetic index C9. The C9 index is conversion of the Planetary Daily Character Figure, a qualitative estimate of the overall level of magnetic activity for

the day, to a scale from 0 to 9. Three categories were established: low geomagnetic activity ($0 \leq C9 \leq 2$), median geomagnetic activity ($3 \leq C9 \leq 5$), and high geomagnetic activity ($6 \leq C9 \leq 9$). Finally, an execution of PRISM with corrected TEC values (PRISM/corTEC) was compared to PRISM/TEC, PRISM/PIM, and the ground truth DISS data.

5.2 Conclusions

The mean residual calculations by season (not distinguishing local hour) indicate a positive model bias for foF2 during all seasons at Wallops Island when PRISM was driven by Global Positioning System (GPS) total electron content (TEC). This is not an unexpected result because the GPS TEC measurements include the contributions from topside/plasmaspheric electrons that are not modeled by PRISM. A similar overestimation of foF2 was observed at Point Arguello only during the summer; variability or error in GPS receiver bias or a statistical anomaly may explain this phenomenon. The chi-square goodness of fit test verifies that PRISM/PIM more accurately calculates foF2 than PRISM/TEC for nearly all hours during every season..

The PRISM/TEC hourly winter mean residuals for both Point Arguello and Wallops Island from 20:00L through 04:00L indicate a negative model bias for hmF2. The average mean residual for this time period was -35 km and -25 km for Wallops Island and Point Arguello, respectively. This model bias is confirmed by the underestimation of hmF2 by PRISM/TEC by almost 35 km in the averaged data output. This may indicate a weakness in the Horizontal Wind Model (HWM90) during winter nighttime hours at mid-latitudes because it is the neutral winds that drive the electron concentrations to higher

altitudes along geomagnetic field lines [*Tascione*, 1992]. Another explanation for the underestimation of hmF2 could be the reflection of the RTA adjustment algorithm problem discussed earlier.

In the analysis of the averaged PRISM/TEC, PRISM/PIM, and DISS data, the consistent feature in all seasons was the overestimation of hmF2 by PRISM/TEC in the pre-midnight through pre-sunset hours. An unexpected finding in the averaged value analysis was the increase in hmF2 values when PRISM ingested GPS TEC values (noted in all seasons). The RTA takes TEC measurements and adjusts the density of each layer (affecting the foF2 calculation which is proportional to number density), but the TEC adjustment should not affect the height of any given layer. The increase in hmF2 when PRISM ingests TEC measurements has been identified by CPI as a flaw in the RTA occurring when there are 'significant' differences in the model output E and F2 layer electron densities. CPI will correct this problem in PRISM 1.7c [*Brown*, 1997]. Another surprising finding was the apparent attempt by PRISM to model a pre-sunset enhancement in hmF2 at Wallops Island for all seasons when ingesting GPS TEC values. Again, when PRISM ingests GPS TEC values, it should not affect the height of the F2 peak. This apparent attempt to model a pre-sunset rise in hmF2 is really just an intensification of the error described above. PRISM accounts for the loss of photoionization near sunset and the dominance of recombination, which in turn increases the difference between the E and F2 layer electron densities. The error leading to the overestimation of hmF2 would be the greatest during this time, thus the rise in the model hmF2. The fact that the PRISM/PIM hmF2 does not show this increase in hmF2 supports

this reasoning; PRISM/PIM is not affected because no real-time parameters were fed into the RTA (the source of the problem).

In a subsequent execution of PRISM the GPS TEC measurements were corrected for topside/plasmaspheric electrons by subtracting four TEC units. Analysis reveals this correction increases the underestimation of the hmF2 by an average of 5 km during the late evening/early morning hours for all seasons. Without the correction factor, PRISM/TEC overestimated foF2 by 1.5 to 2 MHz for all seasons; with the correction factor, the model underestimated foF2 for all seasons by as much as 50% except for equinox at Wallops Island, where the foF2 calculations are in good agreement with the ground truth DISS data.

Two conclusions resulting from separating cases of low, median, and high geomagnetic activity are (1) the overestimation of foF2 during equinox daylight hours and high geomagnetic activity and (2) the underestimation of winter foF2 in the hours near sunset during median and high geomagnetic activity.

5.3 Recommendations

Three recommendations result from this research: 1) the RTA should be corrected to eliminate the rise in hmF2 values when PRISM ingests GPS TEC measurements, 2) an update to the Horizontal Wind Model 1990 should be incorporated into PIM, and 3) either GPS TEC values need to be appropriately corrected for topside/plasmaspheric electrons or a top-side model of H^+ and He^+ should be incorporated into PIM.

The unexpected increase in hmF2 when PRISM ingested GPS TEC data has been noted by CPI programmers in cases where the model F2 and E layer electron

densities were 'significantly' different [Brown, 1997]. A fix to the Real-Time Adjustment (RTA) algorithm is recommended (and planned by CPI for PRISM version 1.7c) for the next version of PRISM.

An update to the Horizontal Wind Model 1990 has been developed by Hedin et al. [1996] and should be incorporated into PIM's theoretical models, LOWLAT and MIDLAT. A new scaling factor corrects for a 44% underestimation of horizontal winds in a portion of the HWM90's database [Biondi et al, 1995]. The newer version of the Horizontal Wind Model, HWM93, used Medium Frequency (MF) Radar and Meteor data to extend the HWM90 to include the lower portions of the ionosphere and altitudes up to the exosphere [Hedin et al., 1996]. HWM93 captures the major wind variations (e.g. latitude, annual, semiannual, local time (tides), and longitude) and will provide a more comprehensive model of horizontal winds encompassing the whole ionosphere. This may correct for PRISM's underestimation of hmF2 in the late evening/early morning hours in winter.

Finally, this thesis implemented a correction of four TEC units to GPS TEC values to account for topside and plasmaspheric electrons. This correction is too high by one or two TEC units for the summer and winter seasons, but seems to be quite adequate for the equinox foF2 calculations at Wallops Island. This strongly suggests a seasonal variation in the topside/plasmaspheric electron contribution to GPS TEC which must be correctly accounted for. A summer/winter correction of two or three (rather than four) TEC units is recommended as a short-term fix. A better solution is to use the 1990 International Reference Ionosphere (IRI90) model to provide a more accurate estimate of the

topside/plasmaspheric electron content, one which can vary with season and local time. To eliminate a need for a correction term, it would be better that PRISM actually model the light ions and plasmasphere instead of correcting for them. The Sheffield University Plasmasphere Ionosphere Model (SUPIM) models the topside of the ionosphere for six ions; when incorporated into PRISM, a correction factor would not be needed. SUPIM is a time-dependent, physical model for the earth's mid- and low-latitude ionosphere and plasmasphere for O^+ , H^+ , He^+ , N_2^+ , O_2^+ , and NO^+ [Bailey *et al.*, 1997]. This model uses the same tilted dipole magnetic field assumptions and inputs from some of the empirical models (e.g. HWM90 and the Plasma Drift Model) as TDIM. The accuracy of future versions of PRISM may benefit from the modeling of topside/plasmaspheric electrons rather than using an estimated, non-varying correction factor.

Recommendations for future work are as follows:

- Test the next version of PRISM (version 1.7c) to ensure that the RTA coding problem (unintended changes in hmF2 when PRISM ingests TEC) is indeed fixed.
- Validate PRISM's ability to correctly model the topside/plasmasphere electron content once the Sheffield University Plasmasphere Ionosphere Model is incorporated into the code.
- Revalidate PRISM for solar maximum conditions (which has not been accomplished since version 1.2).
- Revalidate PRISM at high-latitudes (this was done in a cursory manner for version 1.2). As ground-truth, employ the chain of high-latitude incoherent scatter radars in Norway, Sweden, Finland, and Greenland.

- Extend the study of PRISM accuracy as a function of geomagnetic activity to include the summer season (not done in this thesis).

Finally, the major conclusion of this work is that PRISM version 1.7b should not be operationally employed with GPS TEC as a real-time input until a version of the code incorporating a good topside/plasmasphere model is successfully validated.

Appendix A: Characteristics of the Ionosphere

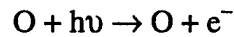
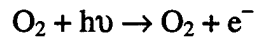
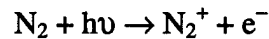
A.1 The Continuity Equation

The ionosphere is often described in terms of stratified layers of electron density. How these electrons are deposited into this stratification is a complex process best described by the continuity equation:

$$\Delta N_e / \Delta t = P - L + \text{transport}$$

where $\Delta N_e / \Delta t$ is the rate of change in the number density of electrons with time, P is the production rate of electrons, L is the loss rate of free electrons, and transport is the rate at which electrons are transported into or out of the volume.

Production of electrons throughout the ionosphere is driven by two processes; the photoionization of neutral particles by solar radiation and the bombardment of the ionosphere by high-energy particles from outside the ionosphere, often called *particle precipitation*. Photoionization is the principle mechanism for electron production throughout the ionosphere. For example, photoionization of the three major species of the ionosphere are as follows:



where $h\nu$ is solar radiation. Particle precipitation occurs primarily within the high latitude auroral zones due to the convergence of the earth's magnetic field lines at those

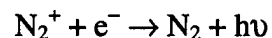
latitudes. High energy electrons and protons are captured by the geomagnetic field and are sent hurling towards the earth, where collisions with neutral gas molecules causes the particles to lose some of their energy to form free electrons, positive ions, and a reduced-energy particles. For example :



where a precipitating high energy electron “e*” collides with atomic oxygen to produce a positive oxygen ion, a reduced-energy precipitating electron, and a free electron. The precipitating particle will continue to create ion/electron pairs until it has lost energy to the point where it is unable to strip any more electrons free through collisions. This process contributes to the electron density production, but generally photoionization (solar radiation) dominates the electron production in the ionosphere.

Photoionization is a daytime source of electrons, thus higher density values occur in the daytime hours as compared to nighttime hours. At sunset, this production comes to an abrupt halt and the loss of electrons dominates to a point of eliminating some layers of the ionosphere completely at night.

The loss of electrons counterbalances production of electrons and occurs even in the daytime. The primary loss mechanism in the ionosphere is recombination in which an electron combines with a positive ion, for example:



As mentioned before, the loss mechanism becomes dominant at nighttime with the absence of the photoionization process. At sunrise, the photoionization rapidly

replenishes the electron density to start the cycle again. The production and loss mechanisms vary by altitude and are briefly discussed later for each layer.

The last term in the continuity equation represents the transport of electrons into and out of the volume. The two contributors to transport are diffusion and plasma drift. Diffusion of ions and electrons is the movement of particles from an area of higher density into an area of lower density. Ion drift can be caused by several outside forces to include gravity, neutral winds, electric and/or magnetic fields, or other forces. The drift velocities of ionospheric particles are highly dependent on collision frequencies, which in turn, are dependent upon the densities of the particles. Simply, the more obstacles to run into, the slower the progress and the smaller the transport term. Plasma drift shows the greatest variability with altitude because the densities decrease with height.

Transport of plasma (electrons) is also greatly influenced by the electric and magnetic fields in the ionosphere. Electric fields, coupled with the Earth's geomagnetic field, produce an $\mathbf{E} \times \mathbf{B}$ drift which serves as a major contribution to electron/ion movement. Equatorial plasma motions in the ionosphere have been measured drifting upwards and to the west during the day, and downwards and to the east at night. In the higher latitudes, currents flow downward on the dawn side and upward on the dusk side of the poleward boundary of the auroral oval. Equatorward of the auroral oval, the field-aligned currents change directions, upward on the dawn side and downward on the dusk side of the auroral oval [Tascione, 1994]. The current systems move plasma, greatly influencing electron densities at each of the ionospheric layers. $\mathbf{E} \times \mathbf{B}$ motions supply

electrons the nighttime F2 layer and are the cause of the Appleton Anomaly discussed later in this appendix.

A.2 Ionospheric Layers

The ionosphere is the region of Earth's upper atmosphere that is partially ionized by solar radiation and energetic particles and contains appreciable numbers of free electrons. The ionosphere begins at about 60 kilometers above the surface of the earth and is classified by four 'layers,' the D layer, E layer, F1 layer, and the F2 layer. See Figure 19 below:

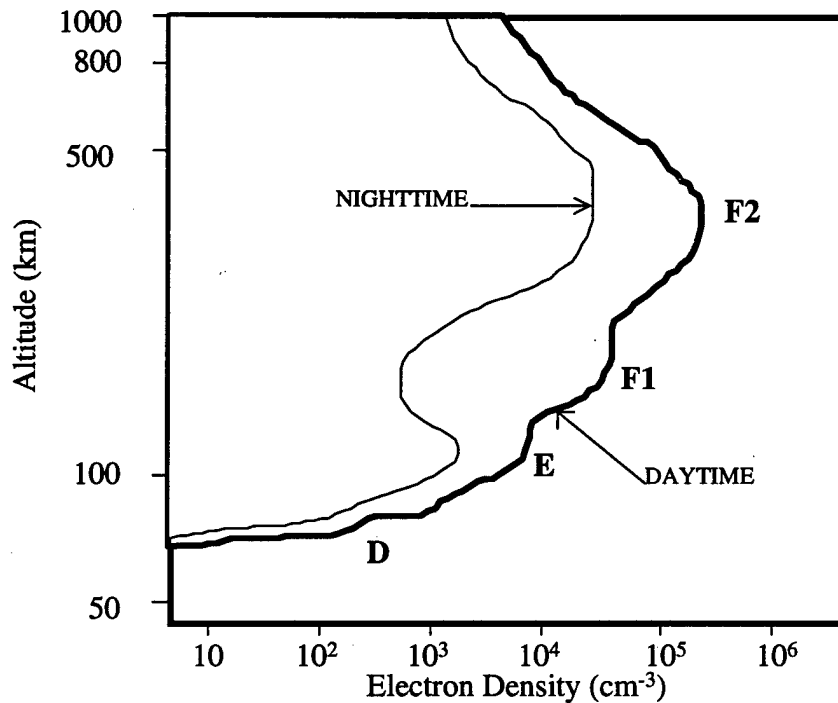


Figure 19: A Typical Mid-Latitude Ionospheric Profile

Starting with the lowest layer, the D layer, a typical height range is from about 60 km to about 95 km above the surface of the earth. The photochemical production of electrons

is caused by Extreme Ultra-Violet (EUV) radiation from the sun (1027 Angstroms to 1118 Angstroms with a large contributions at 1215 Angstroms, the Lyman- α line) ionizing major neutral constituents O_2 and N_2 . Also, in the high latitudes, energetic particles streaming in along geomagnetic field lines bombard the D region and can be the main source of ionization for this layer. The loss of free electrons in the D layer occurs mainly via dissociative recombination ($O_2^+ + e^- \rightarrow O + O$ and $NO^+ + e^- \rightarrow N + O$) [Tascione, 1994]. The major ions in the D region are NO^+ and O^+ due to three-body attachment and photoionization. Negative ions are formed in the D region through electron attachment to O and O_2 atoms. At nighttime, recombination dominates and the D layer disappears until it quickly returns just after sunrise.

The E layer is typically 95 to 140 kilometers above the surface of the earth and is also influenced greatly by the influx of solar radiation (and particle precipitation at high latitudes). The principle production of electrons is through the ionization of O, O_2 , and N_2 due to EUV of $\lambda < 1100$ Angstroms. As in the D region, dissociative recombination plays the major role in eliminating the free electrons. Radiative recombination ($O^+ + e^- \rightarrow O + h\nu$) is also an important factor in electron loss at high latitudes. Unlike the D region, the E region can persist (at reduced electron densities) throughout the night as a result of transient, dense slabs of ionization called 'Sporadic E'. Upward propagating gravity waves and tides collect this ionization into thin, downward propagating layers of enhanced ionization. Sporadic E can occur at all latitudes [Hargreaves, 1992].

The F1 (140-200 km) and F2 (200 - 1000 km) layers contain the greatest concentration of electrons; they represent the area of greatest interest in the study of the

ionosphere, especially the F2 layer. The F layer is bounded by the plasmasphere around 1000 km above the surface of the earth, though this is not a distinct boundary. The primary source of electron production in the F layers is photoionization of atomic oxygen, with a minor contribution from the ionization of atomic nitrogen. One loss mechanism for electrons in the F layer is a two step process beginning with an atom-ion interchange ($O^+ + O_2 \rightarrow O_2^+ + O$ and $O^+ + N_2 \rightarrow NO^+ + N$) and completed with radiative recombination reaction [Tascione, 1992]. A second loss mechanism is diffusion into the plasmasphere.

A.3 Ionospheric Variability

Not only does the ionosphere vary with altitude, but it also varies with latitude, local time, and season. Latitudinal, local time, and seasonal variations are largely dependent on solar zenith angle, controlling the amount of photoionization. The response of the ionosphere to sunrise and sunset is very rapid; electron densities can increase/decrease by two orders of magnitude within an hour of dawn/dusk, revealing dependence on zenith angle. A latitude dependence is noted because as the northern hemisphere enters into its winter months and the solar zenith angle increases, the photoionization rate drops, resulting in decreased electron density. Additionally, ionization due to particle precipitation demonstrates electron content dependence on latitude. Charged particles follow the earth's magnetic field lines and bombard the high latitude ionosphere resulting in large, sometimes even dominant, electron production rates in the auroral ovals.

Equatorward of the auroral ovals there is a distinct feature of the high-latitude ionosphere called the sub-auroral trough. It is an area of unusually low electron density

which occurs in the winter hemisphere in the nighttime sector caused by increasing recombination and high-latitude convection. The polar caps (poleward of the auroral ovals) are bombarded by relatively low-energy (100 eV) electron precipitation which sometimes is called 'polar rain.' The energy fluxes carried to the polar cap region are one to three orders of magnitude less than the precipitation experienced in the auroral ovals [Tascione, 1994].

Other phenomenon which influence the electron content of the ionosphere are the Sudden Ionospheric Disturbance, the Appleton Anomaly, Equatorial "Spread F", and the Mid-latitude F2 Winter Anomaly. The Sudden Ionospheric Disturbance occurs within minutes of a strong solar flare. The X-rays emitted from the flare lead to superionization of the D and lower E layers and is normally about an hour in duration. The Appleton Anomaly (or Equatorial Anomaly) is high concentrations of electrons on either side of the geomagnetic equator in the post sunset sector. The Equatorial Spread F is a thicker than normal F region which occurs at nighttime in low latitudes. The Mid-latitude F2 Winter Anomaly is the transport of plasma by neutral winds from the summer hemisphere to the winter hemisphere causing the daytime F2 peak electron density in winter to be as much as four times greater than the density in the summer hemisphere. The Winter Anomaly occurs during solar maximum conditions and is most apparent between 45°- 55° (geomagnetic) [Tascione, 1994].

Geomagnetic activity also plays a large role in ionospheric variability especially within high latitude regions under the auroral ovals. A geomagnetic 'storm' is defined as a worldwide disturbance in the earth's magnetic field lasting for a day or longer. During

a geomagnetic storm the auroral oval can expand equatorward and greatly affect the ionospheric properties above an underlying ground station. Almost one third of the ionization in the auroral regions is caused by particle precipitation, so stations not normally influenced by the ovals can see increases in electron densities as the oval moves equatorward. Conversely, stations usually under the oval can see decreases in electron content as they become dominated by the polar cap ionosphere. An additional effect of geomagnetic storms is upward convection of molecular nitrogen and oxygen into the F layers from lower altitudes. The N_2 and O_2 combine with the available free electrons and reduce the ambient electron density. Neutral winds can then displace these compositional changes to lower latitudes in the summer and nighttime hemispheres while constraining these changes in the winter and sunlit hemispheres. Variations in the electron density can be more than 30% in latitudes from 45° to 60° and changes of 10% can be experienced in the lower latitudes. Magnetic records show that sometimes these geomagnetic disturbances reappear with a 27-day period. These repetitive disturbances can be attributed to long-lived active regions on the Sun [Tascione, 1992].

The eleven-year solar cycle influences the ionosphere, and large variations from a period of low solar activity, or 'quiet' sun, to a high solar activity period, or 'active' sun are observed. The increase in the number of high energy particles discharged from the sun during its active periods increases ionization caused by particle precipitation. Particles precipitating can increase of over an order of magnitude from solar minimum to solar maximum. Also during periods of active sun, an increase in the number and

strength of geomagnetic storms is observed, although geomagnetic storms can and do occur during quiet sun conditions [*Tascione*, 1992].

Appendix B: Physical Models versus Climatological Models

Physical (or theoretical) models, differ from climatological (or empirical) models in their approach to representing the ionosphere. Physical models try to capture our current theoretical understanding of the relevant physical processes occurring in the ionosphere: whereas climatological models use observations to build extensive databases from which representative parameters may be recovered [McNamara, 1985].

In ionospheric modeling, much effort has been devoted to developing the International Reference Ionosphere (IRI). Since the late 1960's IRI has incorporated a great deal of data from an international network of ionosondes, incoherent scatter radar, radio absorption measurements, and *in situ* measurement from satellites. Using spherical harmonics, ionospheric parameters such as mean critical frequencies, layer peak heights, ion and electron temperatures, ion drift speeds, and other outputs have been modeled over the 24 hours of the day and for varying of latitude, seasons, and solar activity. This large data base has been reduced to a set of coefficients, from which the values of the critical frequencies and other parameters for any given location on the earth can be specified.

One of the drawbacks to this approach is that IRI cannot accurately represent the day-to-day variation in the ionosphere, which can be as high as 25 percent. This is a byproduct of the climatological model: it tends to give a smoothed or averaged result, which will never have the ability to predict anomalous ionospheric behavior such as Sporadic E, and other irregularities [Hargreaves, 1992]. However, the importance of

such models should not be dismissed lightly. The climatological model is well suited to provide a statistical basis for physically-based-model validations.

Physical models have their problems as well, especially those designed to represent the ionosphere. Physical ionospheric models take the continuity, thermodynamic, and momentum equations for the major ion constituents (O^+ , NO^+ , H^+ , and sometimes He^+ in the topside models) and attempt to predict ionospheric characteristics based on our understanding of the relevant physical, chemical, and electrodynamic processes. Quantities such as ion/electron temperature, drift velocities, and neutral wind speeds are important considerations and frequently the models must use empirical databases to specify at least some of these quantities, rather than solving for them. It would be wrong to assert that the physics, chemistry, or variability of the ionosphere are fully understood. These models do help in studying the behavior of the dynamic ionosphere especially for those latitudes and altitudes where observations are incomplete or lacking [McNamara, 1985]. These models will also serve as a basis for future forecast models (which must still rely, in part, on climatological models anyway).

Appendix C: Data Inventory

Table 13: Inventory of Data Used

(The following table includes the data used in this research. A checkmark indicates there was both GPS TEC measurements for real-time parameter inputs and DISS data available for comparison on the specified day.)

	Julian Date	Point Arguello	Wallops Island
20-Mar-94	79	√	
21-Mar-94	80	√	
22-Mar-94	81	√	√
23-Mar-94	82	√	√
24-Mar-94	83	√	√
25-Mar-94	84	√	√
26-Mar-94	85	√	√
27-Mar-94	86	√	√
28-Mar-94	87	√	√
29-Mar-94	88	√	√
30-Mar-94	89	√	√
31-Mar-94	90	√	√
1-Apr-94	91	√	√
2-Apr-94	92	√	√
20-Apr-94	110	√	√
21-Apr-94	111	√	√
22-Apr-94	112	√	√
23-Apr-94	113	√	√
24-Apr-94	114	√	√
25-Apr-94	115	√	√
26-Apr-94	116	√	√
27-Apr-94	117	√	√
28-Apr-94	118	√	√
29-Apr-94	119	√	√
13-Jun-94	164		√
14-Jun-94	165		√
15-Jun-94	166		√
16-Jun-94	167		√
28-Jun-94	179		√
29-Jun-94	180	√	√
30-Jun-94	181	√	√

Table 13: Inventory of Data Used (Continued)

	Julian Date	Point Arguello	Wallops Island
1-Jul-94	182	√	
2-Jul-94	183	√	
12-Jul-94	193		√
13-Jul-94	194		√
14-Jul-94	195		√
15-Jul-94	196		√
26-Jul-94	207	√	
27-Jul-94	208		√
28-Jul-94	209	√	√
29-Jul-94	210	√	√
30-Jul-94	211	√	
31-Jul-94	212	√	
6-Nov-94	310	√	
18-Nov-94	322	√	√
19-Nov-94	323		√
20-Nov-94	324	√	√
21-Nov-94	325	√	√
22-Nov-94	326	√	√
23-Nov-94	327	√	
24-Nov-94	328	√	
6-Dec-94	340	√	
7-Dec-94	341	√	
8-Dec-94	342	√	
9-Dec-94	343	√	
10-Dec-94	344	√	
11-Dec-94	345	√	√
12-Dec-94	346	√	√
13-Dec-94	347	√	√
19-Dec-94	353	√	
20-Dec-94	354	√	
21-Dec-94	355	√	
22-Dec-94	356	√	√
23-Dec-94	357	√	√

Table 13: Inventory of Data Used (Continued)

	Julian Date	Point Arguello	Wallops Island
24-Dec-94	358	√	√
2-Jan-95	2		√
3-Jan-95	3		√
4-Jan-95	4		√
17-Jan-95	17		√
18-Jan-95	18		√
20-Jan-95	20	√	√
21-Jan-95	21	√	√
22-Jan-95	22	√	√
15-Jul-95	196	√	√
16-Jul-95	197	√	√
17-Jul-95	198	√	√
18-Jul-95	199	√	√
19-Jul-95	200	√	√
20-Jul-95	201	√	√
9-Aug-95	221	√	√
10-Aug-95	222	√	
11-Aug-95	223	√	
12-Aug-95	224	√	√
13-Aug-95	225	√	
14-Aug-95	226	√	
15-Aug-95	227	√	
16-Aug-95	228	√	√
17-Aug-95	229	√	√
18-Aug-95	230	√	
3-Sep-95	246	√	
5-Sep-95	248	√	
6-Sep-95	249	√	√
7-Sep-95	250	√	√
8-Sep-95	251	√	√
9-Sep-95	252	√	√
10-Sep-95	253	√	√

Table 13: Inventory of Data Used (Continued)

	Julian Date	Point Arguello	Wallops Island
11-Sep-95	254	√	√
30-Sep-95	273		√
1-Oct-95	274		√
2-Oct-95	275		√
3-Oct-95	276		√
4-Oct-95	277		√
5-Oct-95	278		√
6-Oct-95	279		√
7-Oct-95	280		√
8-Oct-95	281		√
9-Oct-95	282		√
10-Oct-95	283		√
11-Oct-95	284		√
12-Oct-95	285		√
6-Dec-95	340	√	
7-Dec-95	341	√	
8-Dec-95	342	√	
16-Dec-95	350	√	
17-Dec-95	351	√	
18-Dec-95	352	√	
19-Dec-95	353	√	
30-Dec-95	364	√	
31-Dec-95	365	√	
1-Jan-96	1	√	
2-Jan-96	2	√	
3-Jan-96	3	√	
4-Jan-96	4	√	

Appendix D: Sample PRISM Inputs/Outputs

```
*****
= PRISM 1.7b 14-February-1997 =
*****

Is this run interactive (Y/y/N/n)?
N
n
What is the year (1901 to 2099)?
1994
1994
What is the day of the year (1 to 365)?
079
79
What is the Universal Time in hhmm (0000 to 2359)?
0000
0
The types of station output are:
0=Critical frequencies and heights and TEC
1=EDPs
2=EDPs, critical frequencies and heights, and TEC
3=No station output
What type of station output do you want (0 to 3)?
0
0
The types of gridded output are:
0=Critical frequencies and heights and TEC
1=EDPs
2=EDPs, critical frequencies and heights, and TEC
3=No gridded output
What type of gridded output do you want (0 to 3)?
0
0
Do you want to normalize foF2 to the URSI coefficients (0=Yes, 1=No)?
1
1
Do you want an output station list other than the direct data ionosonde
station list (Y/y/N/n)?
y
y
What is the name of the output station list file?
arguello.all
arguello.all
What is the name of the gridded output file?
mytest.out
mytest.out
```

Figure 20: A Sample PRISM Input Sequence

Do you want a non-global output latitude/longitude grid (Y/y/N/n)?
y
y
Do you want the output latitude/longitude grid to be in geographic or magnetic coordinates (G/g/M/m)?
g
g
What are the latitude (-90. to 90. Degrees north) and longitude (degrees east) of the southwest corner of the output latitude/longitude grid?
35.6,239.4
35.6000 239.4000
What are the latitude (-90. to 90. Degrees north) and longitude (degrees east) of the northeast corner of the output latitude/longitude grid?
35.6,239.4
35.6000 239.4000
Since the southwest and northeast latitudes are equal and the southwest and northeast longitudes are equal, the specified latitude/longitude region is a single point...
What is the real Kp (0. To 6.5)?
3.3
3.30000
What are the Bz and By components of the IMF?
-1,1
-1.00000 1.00000
What is the 90-day average F10.7 (70. to 210.)?
103.18864
103.1886
The possible relationships between daily F10.7 and effective sunspot number are:
0=Daily F10.7 and effective sunspot number are unrelated
1=Effective sunspot number is to be calculated from daily F10.7
2=Daily F10.7 is to be calculated from effective sunspot number
How do you want daily F10.7 to be related to effective sunspot number (0 to 2)?
0
0
What is the daily F10.7 (70. to 210.)?
91.98889
What is the effective sunspot number (0. to 300.)?
8
Daily F10.7= 91.99 and effective sunspot number = 8.00

Figure 20: A Sample PRISM Input Sequence (continued)

YEAR	DAY	UT (sec)	F10.7	Kp	Solar Sunspot Number			
1994	80	43200.0	91.5	3.7	17.00			
IONOSONDE		data	1 records					
0								
NUM	UT	GLAT	GLON	MLAT	MLON	MLT	FoF2	HmF2
1	12.00	35.60	239.40	41.49	301.80	3.39	4.98	331.17
FoF1	HmF1	FoE	HmE	TEC				
0.00	0.00	0.45	105.00	6.87				

Figure 21: A Sample PRISM Output File

This output gives geographic latitude (GLAT), geographic longitude (GLON), magnetic latitude (MLAT), and magnetic longitude (MLON) of the station in question. It also gives magnetic local time (MLT) for the observational period. Critical frequencies in MHz (FoF2, FoF1, and FoE) and heights in kilometers of electron density peaks of the ionospheric layers are also calculated (HmF2, HmF1, and HmE). The total electron count (TEC) is given in TEC units

YEAR	DAY	UT (sec)	F10.7	Kp	Solar Sunspot Number	
1994	79	0.0	92.0	3.3	8.00	
IONOSONDE		data,	1 records			
1						
Number of altitude points =			50			
Altitudes						
90.00	95.00	100.00	105.00	110.00		
115.00	120.00	125.00	130.00	135.00		
140.00	145.00	150.00	160.00	170.00		
180.00	190.00	200.00	210.00	220.00		
230.00	240.00	250.00	260.00	270.00		
280.00	290.00	300.00	320.00	340.00		
360.00	380.00	400.00	450.00	500.00		
550.00	600.00	650.00	700.00	750.00		
800.00	850.00	900.00	950.00	1100.00		
1200.00	1300.00	1400.00	1500.00	1600.00		
1	0.00	35.60	239.40	41.49	301.80	15.37
Densities						
2.46E+01	1.13E+03	1.41E+04	5.54E+04	8.13E+04		
8.25E+04	8.01E+04	7.93E+04	7.89E+04	8.08E+04		
8.50E+04	9.09E+04	9.82E+04	1.16E+05	1.40E+05		
1.73E+05	2.24E+05	2.96E+05	3.86E+05	4.85E+05		
5.70E+05	6.46E+05	7.02E+05	7.17E+05	7.02E+05		
6.73E+05	6.37E+05	5.97E+05	5.21E+05	4.52E+05		
3.92E+05	3.41E+05	2.97E+05	2.12E+05	1.54E+05		
1.16E+05	8.97E+04	7.30E+04	6.01E+04	4.97E+04		
4.14E+04	3.47E+04	2.93E+04	2.10E+04	1.53E+04		
1.12E+04	8.34E+03	6.23E+03	4.69E+03	3.55E+03		

Figure 22: A Sample Electron Density Profile Output

The electron density profile (EDP) is given for each of the first table's altitude points. The line directly above 'Densities' gives a '1' for the first output location for the specified time '0.00' UT which is located at 35.60 latitude and 239.40 longitude. The next numbers, '41.49' and '301.80' are the magnetic latitude and longitude respectively. The '15.37' is the total electron content for the specified time and location.

Appendix E: Statistics

Table 14: Equinox Hourly hmF2 Mean Residuals and Standard Deviations of the Mean Residuals

The mean residual is calculated by model output - DISS in kilometers. The gray rows are the standard deviations of the mean residuals.

Equinox	Point Arguello		Wallops Island	
Local Hour	PRISM/TEC	PRISM/PIM	PRISM/TEC	PRISM/PIM
0	-4.334	-6.598	-24.069	-27.912
	63.165	62.173	26.184	26.02
1	-10.412	-11.981	-29.659	-33.917
	40.664	36.725	21.59	20.289
2	-23.366	-25.102	-26.878	-31.443
	72.114	68.133	28.711	26.704
3	-21.699	-24.087	-27.683	-32.047
	62.06	60.067	29.154	28.263
4	-21.585	-25.838	-11.573	-15.2
	53.3	52.73	37.773	36.17
5	-24.808	-28.191	-2.431	-4.883
	41.927	41.355	41.655	40.319
6	-16.689	-17.162	-2.661	-7.081
	44.645	43.851	27.055	25.614
7	-33.966	-37.011	-4.521	-7.98
	38.512	39.487	33.065	32.757
8	-16.117	-17.335	12.629	10.158
	40.247	42.232	17.277	16.061
9	-12.655	-12.83	16.303	13.776
	47.405	49.748	23.56	22.643
10	-10.689	-11.293	3.296	1.19
	39.723	41.343	26.893	26.399
11	-34.37	-35.011	6.161	3.947
	55.979	58.728	25.459	25.322
12	-21.055	-20.749	1.523	-0.42
	48.53	50.986	25.508	26.235
13	-16.353	-15.552	-0.291	-2.336
	33.396	35.925	21.876	22.34
14	-13.563	-10.362	-1.885	-3.804
	26.082	31.321	15.793	16.351

Table 14: Equinox Hourly hmF2 Mean Residuals and Standard Deviations of the Mean Residuals (Continued).

Equinox	Point Arguello		Wallops Island	
Local Hour	PRISM/TEC	PRISM/PIM	PRISM/TEC	PRISM/PIM
15	-7.157	-1.232	-1.667	-3.405
	28.173	33.037	15.103	15.223
16	1.616	-4.621	-1.376	-2.608
	48.796	52.142	18.383	16.768
17	-6.514	0.3743	42.724	7.407
	45.329	41.988	18.185	17.78
18	-7.092	-4.118	35.276	0.689
	64.151	62.5	21.574	21.269
19	6.938	6.929	8.914	25.969
	44.396	40.423	23.432	19.186
20	-0.019	0.114	2.974	23.595
	63.737	59.386	37.683	25.873
21	-5.139	-5.317	15.548	11.56
	64.817	61.318	23.067	22.757
22	-9.895	-12.485	-7.747	-11.896
	76.416	76.171	25.238	25.872
23	-25.534	-25.359	-18.946	-23.095
	75.175	68.216	23.747	22.053

Table 15: Summer Hourly hmF2 Mean Residuals and Standard Deviations of the Mean Residuals

The mean residual is calculated by model output - DISS in kilometers. The gray rows are the standard deviations of the mean residuals.

Summer	Point	Arguello	Wallops	Island
Local Hour	PRISM/TEC	PRISM/PIM	PRISM/TEC	PRISM/PIM
0	14.839	9.222	-25.104	-30.457
	39.836	40.751	59.656	59.578
1	-2.082	-8.011	-22.551	-27.48
	35.906	36.555	30.525	30.722
2	6.34	0.332	-22.572	-27.737
	35.888	35.961	32.315	32.355
3	3.895	-1.56	-8.391	-13.939
	33.597	34.515	29.997	30.331
4	2.076	2.527	8.804	3.627
	23.614	24.853	40.364	40.13
5	-4.419	-8.624	21.026	17.6394
	31.269	28.372	33.985	32.933
6	-3.606	-3.525	-15.58	-17.548
	47.374	41.902	33.648	33.337
7	15.15	13.078	0.973	-1.158
	33.511	31.263	35.062	35.473
8	27.424	24.387	3.334	-2.51
	27.97	26.63	26.545	26.641
9	21.15	19.42	-0.089	-3.763
	27.988	25.657	30.63	31.398
10	-1.014	-4.341	3.373	0.323
	58.01	57.133	30.28	30.887
11	7.89	5.362	15.077	11.547
	71.736	71.412	39.823	40.292
12	20.5943	17.326	40.922	38.157
	23.254	23.673	40.287	41.076
13	34.224	30.302	38.203	35.687
	35.673	36.454	40.105	40.958
14	13.48	13.4811	30.092	27.973
	27.804	31.591	28.189	29.07

Table 15: Summer Hourly hmF2 Mean Residuals and Standard Deviations of the Mean Residuals (Continued)

Summer	Point Arguello		Wallops Island	
Local Hour	PRISM/TEC	PRISM/PIM	PRISM/TEC	PRISM/PIM
15	20.826	25.1886	12.659	10.619
	14.308	13.58	35.328	35.661
16	20.319	18.078	2.017	-1.14
	26.618	28.517	31.437	32.067
17	1.516	-1.32	25.345	-3.922
	18.552	20.226	19.493	20.69
18	-0.608	-4.943	10.28	-14.728
	38.34	38.637	11.945	11.355
19	-0.026	-4.213	4.498	15.352
	28.377	28.839	40.454	39.36
20	20.673	16.404	32.301	43.538
	21.787	22.704	19.659	16.347
21	18.835	13.702	32.926	29.048
	22.022	22.568	23.833	22.75
22	18.701	13.183	11.978	7.624
	44.414	45.146	35.004	35.032
23	13.26	8.493	-5.522	-9.893
	29.98	30.016	28.642	29.036

Table 16: Winter Hourly hmF2 Mean Residuals and Standard Deviations of the Mean Residuals

The mean residual is calculated by model output - DISS in kilometers. The gray rows are the standard deviations of the mean residuals.

Winter	Point Arguello		Wallops Island	
Local Hour	PRISM/TEC	PRISM/PIM	PRISM/TEC	PRISM/PIM
0	-34.651	-39.450	-24.835	-30.003
	30.876	31.106	30.185	30.994
1	-27.447	-32.112	-39.564	-45.483
	31.708	31.715	19.103	19.352
2	-26.047	-31.059	-31.897	-37.727
	27.684	27.670	30.825	30.689
3	-16.435	-21.529	-35.307	-41.020
	25.384	25.328	25.006	24.935
4	-17.781	-22.867	-18.125	-24.206
	45.864	45.907	34.354	33.959
5	-14.518	-18.929	2.532	-3.715
	40.450	39.936	37.243	37.063
6	-14.316	-18.601	-9.079	-14.594
	33.273	34.001	39.831	39.420
7	0.864	-3.139	5.437	-0.188
	29.338	29.661	26.309	26.616
8	7.543	4.682	-4.237	-8.158
	18.574	18.674	19.787	19.698
9	-6.279	-9.049	-28.494	-32.598
	17.909	17.933	48.759	48.850
10	-9.854	-12.852	-9.362	-12.572
	19.002	19.030	17.524	17.470
11	-19.909	-22.732	-3.568	-6.563
	31.116	33.562	15.765	15.573
12	-9.020	-11.623	-1.288	-4.382
	17.838	18.186	12.737	13.131
13	-3.088	-5.207	-3.369	-5.865
	16.859	17.217	15.734	15.469
14	3.563	-9.829	-5.231	-7.413
	19.076	19.682	45.088	45.114

Table 16: Winter Hourly hmF2 Mean Residuals and Standard Deviations of the Mean Residuals (Continued)

Winter	Point Arguello		Wallops Island	
Local Hour	PRISM/TEC	PRISM/PIM	PRISM/TEC	PRISM/PIM
15	-3.457	-12.885	4.670	1.928
	29.417	29.792	13.226	13.357
16	-18.528	-9.076	6.363	3.190
	24.931	23.532	19.781	19.439
17	-11.252	2.070	27.697	5.764
	45.801	40.673	21.936	19.867
18	-17.617	-15.064	-1.568	-10.525
	52.732	50.256	41.685	40.315
19	-6.130	-4.980	-6.304	-6.589
	39.513	39.422	27.882	25.249
20	-16.007	-16.779	-29.993	-29.534
	35.764	34.659	32.387	34.969
21	-14.942	-19.386	-34.719	-38.451
	34.700	34.269	27.717	28.767
22	-24.708	-30.273	-39.835	-45.383
	37.253	36.900	32.120	31.607
23	-39.445	-44.608	-31.739	-36.944
	48.176	48.172	22.194	21.776

Table 17: Equinox Hourly foF2 Mean Residuals and Standard Deviations of the Mean Residuals

The mean residual is calculated by model output - DISS in MHz. The gray rows are the standard deviations of the mean residuals

Equinox	Point Arguello		Wallops Island	
Local Hour	PRISM/TEC	PRISM/PIM	PRISM/TEC	PRISM/PIM
0	0.279	-1.028	1.473	-0.045
	2.199	2.309	1.054	0.695
1	0.760	-0.409	1.481	-0.184
	0.881	0.739	1.164	0.651
2	0.838	-0.647	1.500	-0.327
	1.000	0.680	1.145	0.606
3	0.798	-0.592	1.385	-0.512
	0.935	0.414	1.349	0.559
4	0.873	-0.056	1.323	-0.524
	0.895	0.719	1.258	0.507
5	0.648	-0.707	1.641	-0.022
	0.995	0.872	1.229	0.440
6	0.690	-0.403	1.835	0.239
	0.904	0.777	1.268	0.506
7	1.192	0.136	1.134	-0.310
	0.909	0.811	1.286	0.828
8	0.807	-0.110	1.162	-0.117
	0.897	0.988	1.131	0.738
9	0.773	0.099	1.206	-0.058
	0.990	1.148	1.011	0.767
10	0.778	0.003	1.139	-0.146
	0.891	1.185	1.089	0.896
11	0.447	-0.189	1.046	-0.207
	0.779	1.006	0.928	0.907
12	0.257	-0.269	0.815	-0.207
	1.015	1.268	0.965	1.065
13	0.218	-0.122	0.893	-0.126
	0.851	1.097	0.992	1.048
14	0.000	-0.101	0.820	-0.104
	0.675	1.171	0.951	1.121

Table 17: Equinox Hourly foF2 Mean Residuals and Standard Deviations of the Mean Residuals (Continued)

Equinox	Point Arguello		Wallops Island	
Local Hour	PRISM/TEC	PRISM/PIM	PRISM/TEC	PRISM/PIM
15	0.037	0.334	0.880	0.073
	0.616	1.425	0.879	0.953
16	0.218	0.024	0.723	0.016
	0.722	1.894	0.985	1.016
17	0.191	0.266	0.435	-0.085
	0.691	1.009	1.110	0.983
18	0.017	-0.172	0.003	-0.201
	0.613	0.947	1.173	1.161
19	0.412	-0.202	1.066	-0.405
	0.902	0.849	0.996	1.078
20	0.611	-0.134	1.137	-0.315
	1.067	0.912	1.159	0.970
21	0.873	0.115	1.510	0.024
	1.009	0.881	1.027	0.820
22	0.513	-0.586	1.601	0.126
	1.949	1.991	0.987	0.774
23	0.707	-0.300	1.601	0.082
	1.032	1.004	1.125	0.760

Table 18: Summer Hourly foF2 Mean Residuals and Standard Deviations of the Mean Residuals

The mean residual is calculated by model output - DISS in MHz. The gray rows are the standard deviations of the mean residuals

Summer	Point Arguello		Wallops Island	
Local Hour	PRISM/TEC	PRISM/PIM	PRISM/TEC	PRISM/PIM
0	2.982	0.135	1.453	-0.011
	1.583	0.574	0.604	0.522
1	3.274	0.021	1.485	-0.191
	1.521	0.424	0.539	0.534
2	2.976	-0.087	1.761	-0.161
	1.468	0.364	0.439	0.525
3	2.761	-0.293	1.919	-0.193
	1.481	0.394	0.465	0.527
4	2.841	0.029	1.689	-0.291
	1.333	0.373	0.381	0.350
5	2.271	-0.150	1.837	0.023
	1.538	0.367	0.520	0.520
6	1.904	-0.017	2.162	0.647
	1.352	0.432	0.668	0.561
7	2.241	0.590	1.321	0.159
	1.572	0.490	0.743	0.792
8	1.454	0.074	0.951	-0.101
	1.976	1.360	1.040	1.155
9	1.274	0.065	0.323	0.465
	2.112	1.588	1.319	1.624
10	1.537	0.244	0.651	0.292
	1.322	0.870	0.590	0.979
11	1.496	0.306	0.773	0.022
	0.955	0.824	0.922	0.974
12	1.598	0.431	1.051	0.389
	1.157	0.996	0.453	0.579
13	1.804	1.034	0.736	0.181
	0.885	0.619	1.746	1.580
14	1.435	0.989	1.348	0.808
	0.788	0.767	0.752	0.969

Table 18: Summer Hourly foF2 Mean Residuals and Standard Deviations of the Mean Residuals

Summer	Point Arguello		Wallops Island	
Local Hour	PRISM/TEC	PRISM/PIM	PRISM/TEC	PRISM/PIM
15	1.433	1.131	1.169	0.617
	0.606	0.931	0.562	0.722
16	1.513	0.682	1.306	0.599
	1.177	0.852	0.543	0.643
17	1.659	0.664	1.711	0.353
	0.965	0.575	0.603	0.532
18	1.998	0.567	1.563	0.196
	0.991	0.666	0.696	0.690
19	1.857	0.237	1.354	0.575
	1.045	0.624	0.843	0.917
20	1.383	-0.391	1.290	0.701
	1.346	0.727	0.844	0.647
21	2.026	0.040	1.408	0.310
	1.263	0.683	0.592	0.835
22	2.382	0.130	1.557	0.404
	1.476	0.619	0.744	0.782
23	2.646	0.048	1.358	0.109
	1.894	0.910	0.690	0.749

Table 19: Winter Hourly foF2 Mean Residuals and Standard Deviations of the Mean Residuals

The mean residual is calculated by model output - DISS in MHz. The gray rows are the standard deviations of the mean residuals.

Winter	Point Arguello		Wallops Island	
Local Hour	PRISM/TEC	PRISM/PIM	PRISM/TEC	PRISM/PIM
0	0.877	-0.090	1.555	-0.458
	1.557	1.382	0.820	0.635
1	0.841	-0.914	1.173	-0.868
	1.480	1.097	0.974	0.845
2	0.733	-1.032	1.315	-0.813
	1.514	1.259	0.762	0.790
3	0.748	-0.875	1.107	-0.990
	1.193	0.960	0.900	0.770
4	0.425	-1.086	1.127	-1.022
	1.688	1.312	0.882	0.736
5	0.375	-1.028	1.302	-0.856
	1.883	1.572	0.785	0.695
6	0.505	-0.725	1.362	-0.746
	1.837	1.440	0.881	0.668
7	-0.502	-1.533	1.242	-0.797
	1.731	1.417	1.087	1.068
8	-0.093	-1.958	1.694	-0.407
	1.757	1.097	0.996	1.042
9	0.877	-0.342	1.475	-0.543
	0.962	0.606	0.831	0.959
10	0.867	-0.516	0.863	-1.044
	1.045	0.826	1.273	1.201
11	0.479	-0.895	0.909	-1.030
	1.274	1.085	1.083	0.980
12	0.517	-0.895	1.369	-0.513
	1.239	0.929	0.684	0.654
13	0.424	-0.825	1.576	-0.222
	1.308	0.923	0.562	0.662
14	-0.062	-0.584	1.605	-0.103
	1.057	0.776	0.657	0.819

Table 19: Winter Hourly foF2 Mean Residuals and Standard Deviations of the Mean Residuals (Continued)

Winter	Point Arguello		Wallops Island	
Local Hour	PRISM foF2	PIM foF2	PRISM foF2	PIM foF2
15	-0.793	-0.258	1.674	0.036
	1.563	1.042	0.636	0.685
16	-0.947	-0.735	1.573	0.021
	1.800	1.271	0.871	0.919
17	-0.408	-0.281	0.130	-0.577
	1.759	1.183	1.170	0.950
18	0.146	-0.177	0.361	-0.535
	1.771	1.234	1.364	0.818
19	0.186	-0.468	1.017	-0.467
	1.728	0.996	1.103	0.704
20	0.303	-0.686	1.239	-0.150
	1.599	0.952	0.993	0.469
21	0.243	-1.030	1.473	-0.190
	1.761	1.154	0.700	0.572
22	0.151	-1.403	1.497	-0.481
	2.027	1.540	0.835	0.692
23	0.527	-1.184	1.583	-0.336
	1.683	1.272	0.770	0.563

Table 20: Reduced Chi-Squared for Equinox hmF2

Equinox	Point Arguello		Wallops Island	
Local Hour	PRISM/TEC	PRISM/PIM	PRISM/TEC	PRISM/PIM
0	9.421	8.930	3.474	3.986
1	4.848	4.056	3.862	4.489
2	12.414	11.178	4.496	4.936
3	10.162	9.857	4.777	5.353
4	7.138	7.440	5.092	4.845
5	7.448	7.747	5.513	5.006
6	6.888	6.652	2.713	2.508
7	7.705	8.589	3.859	3.817
8	6.334	7.078	2.044	1.612
9	8.917	10.008	4.139	3.590
10	6.547	7.093	2.987	2.800
11	13.160	14.329	3.118	2.957
12	8.421	9.276	3.106	3.169
13	4.596	5.162	2.195	2.278
14	3.212	4.162	1.031	1.133
15	3.197	4.505	0.878	0.907
16	1.285	9.956	1.262	1.068
17	5.949	4.980	8.843	1.529
18	10.619	9.935	6.952	1.726
19	7.341	6.128	2.795	4.202
20	11.831	10.453	5.234	4.831
21	10.597	9.622	2.785	2.314
22	13.910	13.948	2.100	2.389
23	13.482	11.313	2.643	2.905

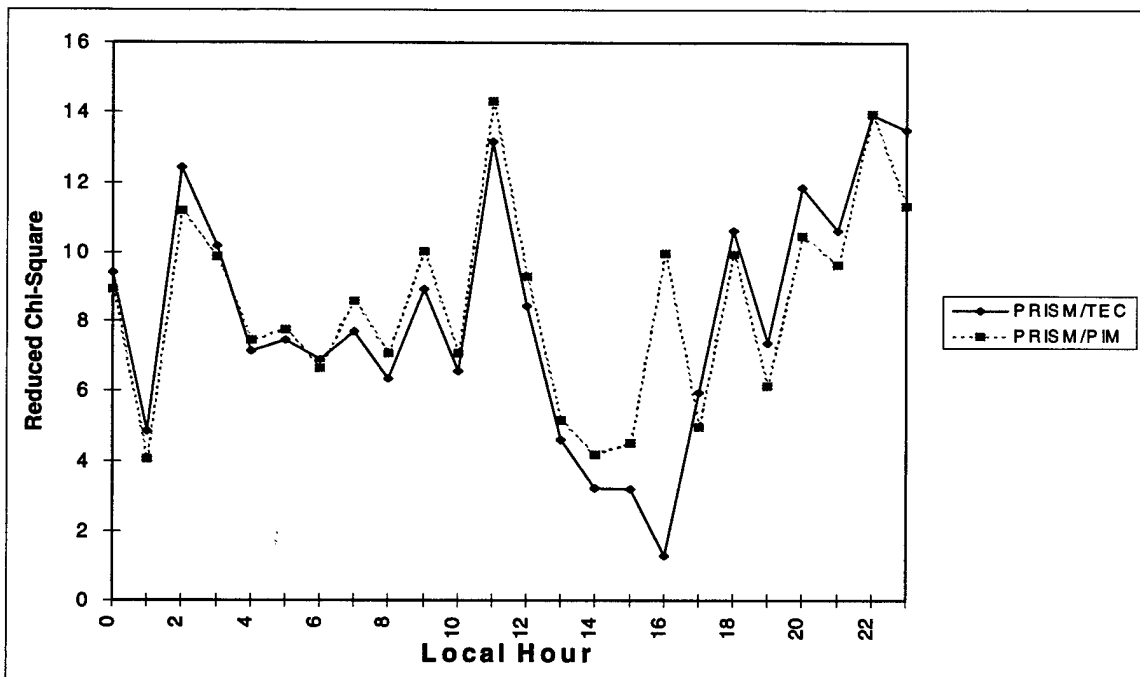


Figure 23: Point Arguello Reduced Chi-Squared for Equinox hmF2

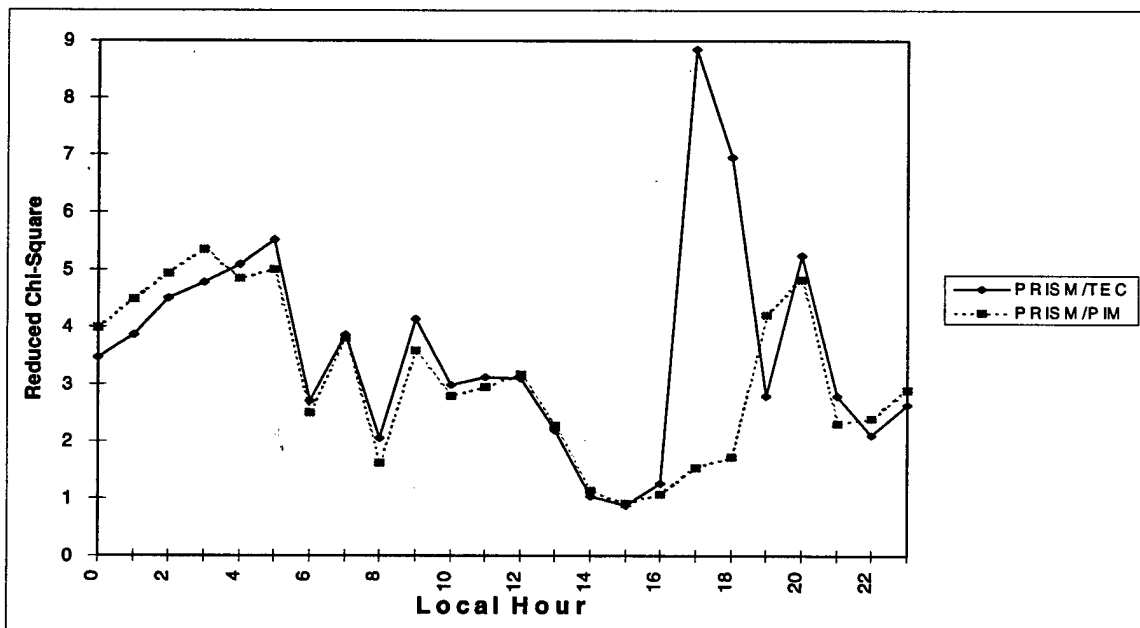


Figure 24: Wallops Island Reduced Chi-Squared for Equinox hmF2

Table 21: Reduced Chi-Squared for Summer hmF2

Summer	Point Arguello		Wallops Island	
Local Hour	PRISM/TEC	PRISM/PIM	PRISM/TEC	PRISM/PIM
0	7.077	6.703	8.625	9.241
1	4.290	4.521	4.074	4.781
2	4.615	4.349	4.365	5.106
3	3.887	3.935	3.023	3.395
4	1.772	1.839	6.661	6.127
5	3.254	2.750	7.563	6.564
6	7.292	5.647	4.690	4.842
7	5.234	4.468	5.120	5.144
8	7.158	6.025	2.614	2.520
9	5.306	4.483	3.443	3.615
10	13.160	12.686	3.897	3.931
11	18.223	17.495	8.631	8.253
12	3.957	3.443	18.001	17.109
13	11.724	10.748	15.863	15.179
14	3.882	4.747	8.157	7.796
15	2.582	3.404	6.692	6.462
16	4.930	4.979	4.091	4.152
17	1.337	1.567	3.756	1.411
18	4.043	4.071	0.810	1.095
19	2.548	2.657	5.080	5.836
20	3.265	2.793	5.683	8.804
21	3.066	2.514	6.212	5.116
22	7.045	6.464	4.601	4.202
23	3.504	3.105	2.496	2.707

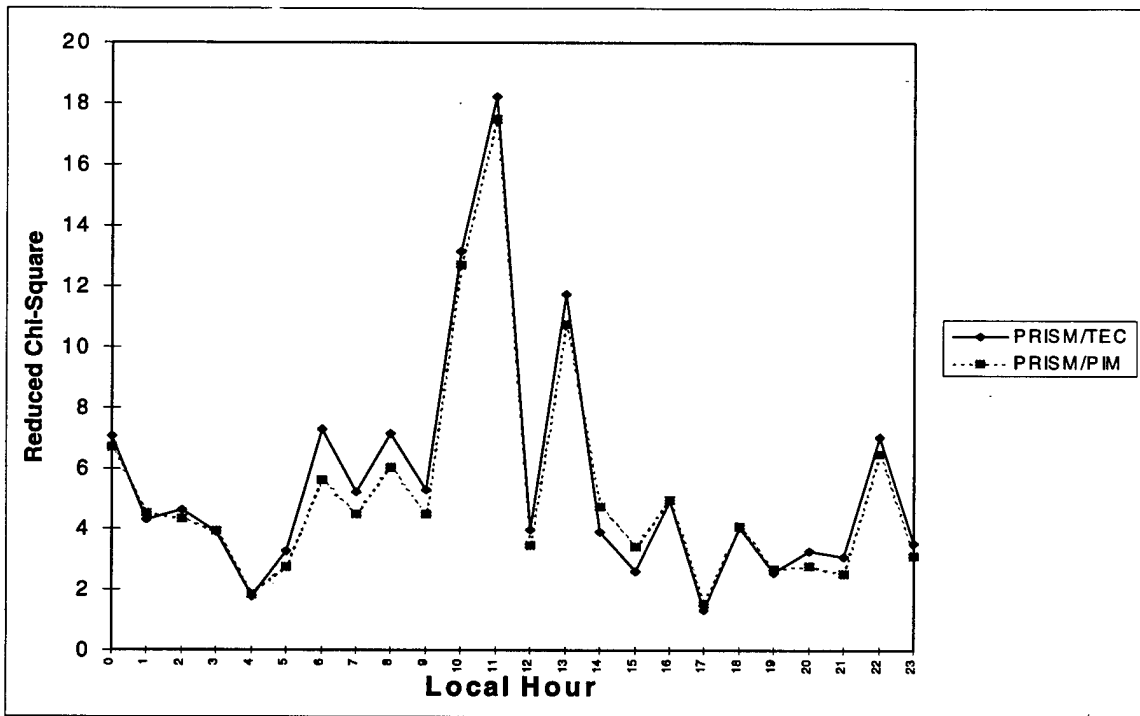


Figure 25: Point Arguello Reduced Chi-Squared for Summer hmF2

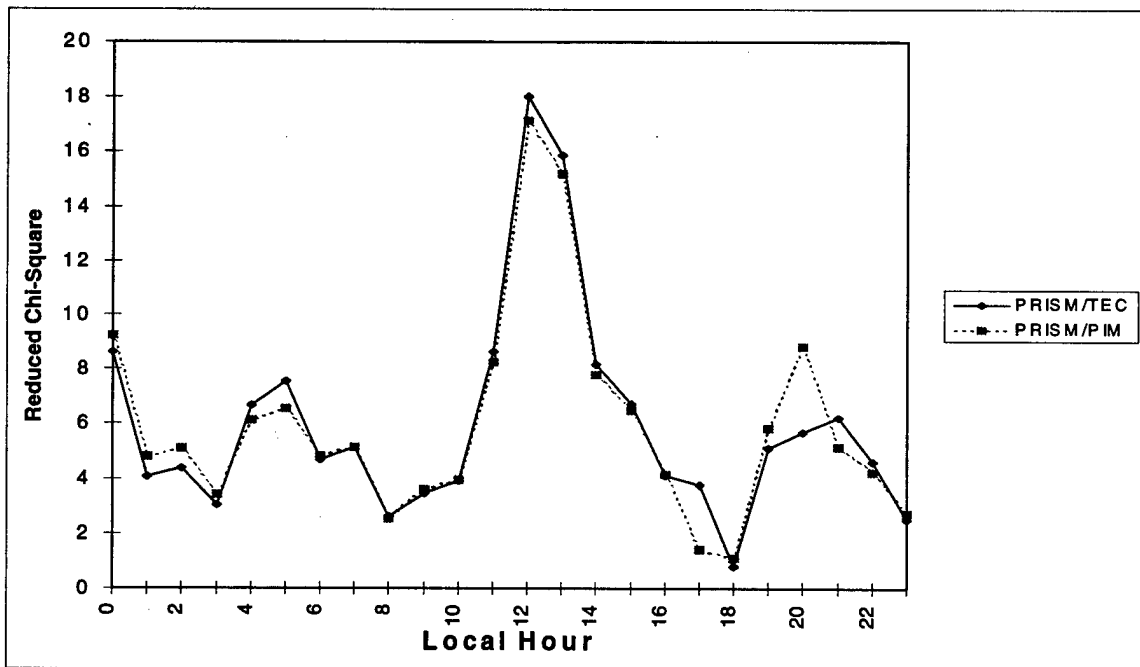


Figure 26: Wallops Island Reduced Chi-Squared for Summer hmF2

Table 22: Reduced Chi-Squared for Winter hmF2

Winter	Point Arguello		Wallops Island	
Local Hour	PRISM/TEC	PRISM/PIM	PRISM/TEC	PRISM/PIM
0	6.100	7.186	6.140	7.498
1	5.200	6.015	5.951	7.577
2	4.293	5.148	5.920	7.205
3	2.701	3.262	3.771	4.911
4	6.622	7.137	3.413	3.594
5	5.535	5.773	6.111	5.406
6	4.093	4.653	4.756	4.718
7	3.076	3.085	3.263	2.697
8	1.724	1.554	1.389	1.293
9	1.438	1.597	7.807	8.409
10	1.741	1.999	1.225	1.405
11	4.526	4.850	0.972	1.041
12	1.527	1.775	0.616	0.600
13	1.181	1.282	0.885	0.814
14	1.476	1.776	5.218	5.186
15	3.235	3.694	1.065	0.835
16	3.460	2.329	2.060	1.707
17	6.065	4.768	9.061	2.393
18	8.278	7.360	6.146	4.788
19	5.359	5.245	2.374	2.015
20	4.845	4.792	5.356	6.138
21	4.400	4.697	6.639	8.309
22	5.586	6.394	5.942	7.169
23	9.412	10.619	5.559	6.865

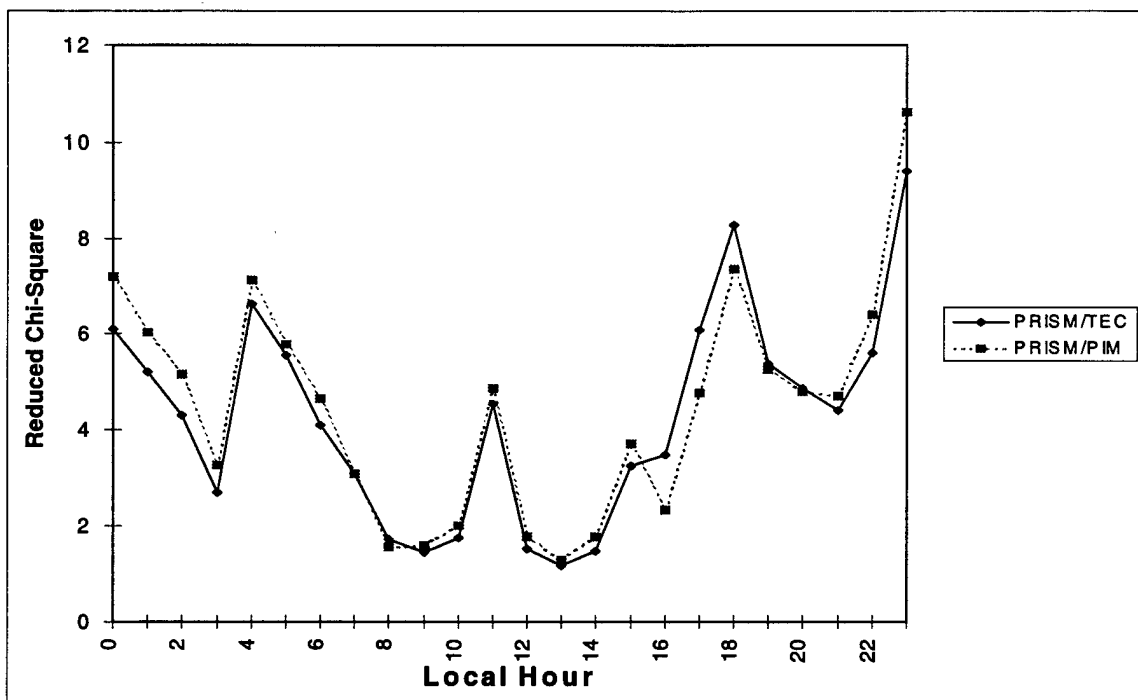


Figure 27: Point Arguello Reduced Chi-Squared for Winter hmF2

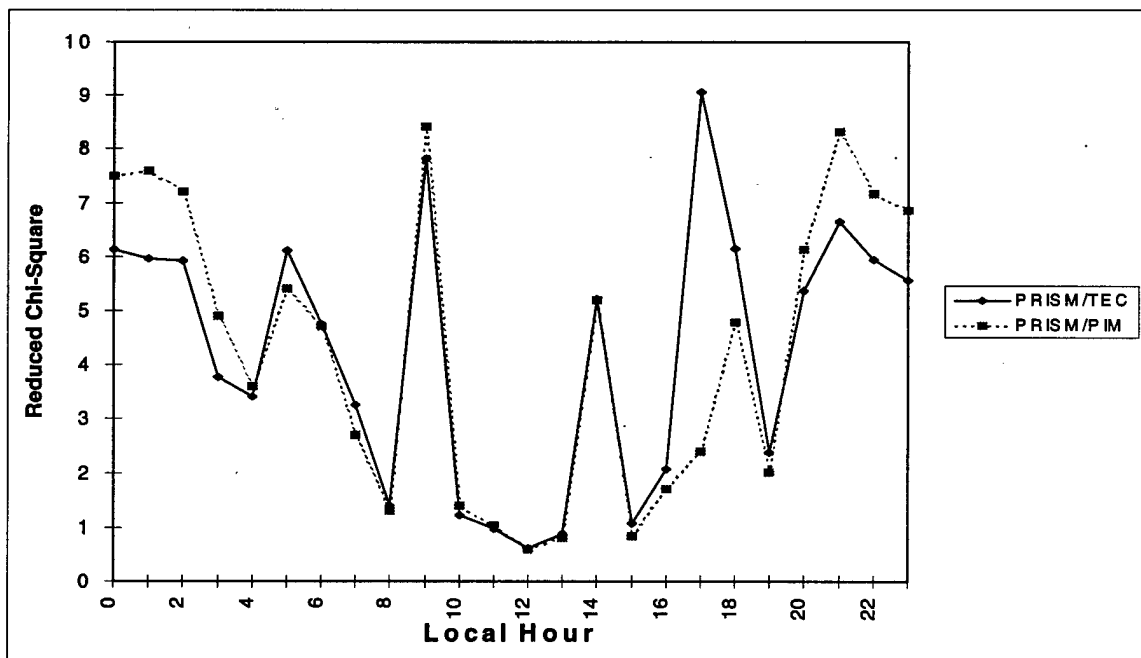


Figure 28: Wallops Island Reduced Chi-Squared for Winter hmF2

Table 23: Reduced Chi-Squared for Equinox foF2

Equinox	Point Arguello		Wallops Island	
Local Hour	PRISM/TEC	PRISM/PIM	PRISM/TEC	PRISM/PIM
0	0.668	0.634	1.050	0.132
1	0.345	0.167	1.152	0.111
2	0.439	0.181	1.215	0.116
3	0.378	0.124	1.340	0.142
4	0.425	0.135	1.271	0.142
5	0.379	0.256	1.520	0.060
6	0.305	0.152	1.423	0.084
7	0.437	0.138	0.656	0.127
8	0.261	0.173	0.520	0.101
9	0.263	0.231	0.475	0.112
10	0.230	0.243	0.458	0.139
11	0.116	0.143	0.359	0.145
12	0.155	0.217	0.285	0.188
13	0.125	0.183	0.318	0.178
14	0.057	0.197	0.283	0.205
15	0.058	0.285	0.282	0.168
16	0.083	0.443	0.258	0.179
17	0.080	0.190	0.252	0.158
18	0.059	0.152	0.229	0.216
19	0.017	0.115	0.447	0.215
20	0.309	0.188	0.592	0.178
21	0.456	0.255	0.905	0.162
22	0.605	0.513	1.041	0.163
23	0.385	0.263	1.241	0.182

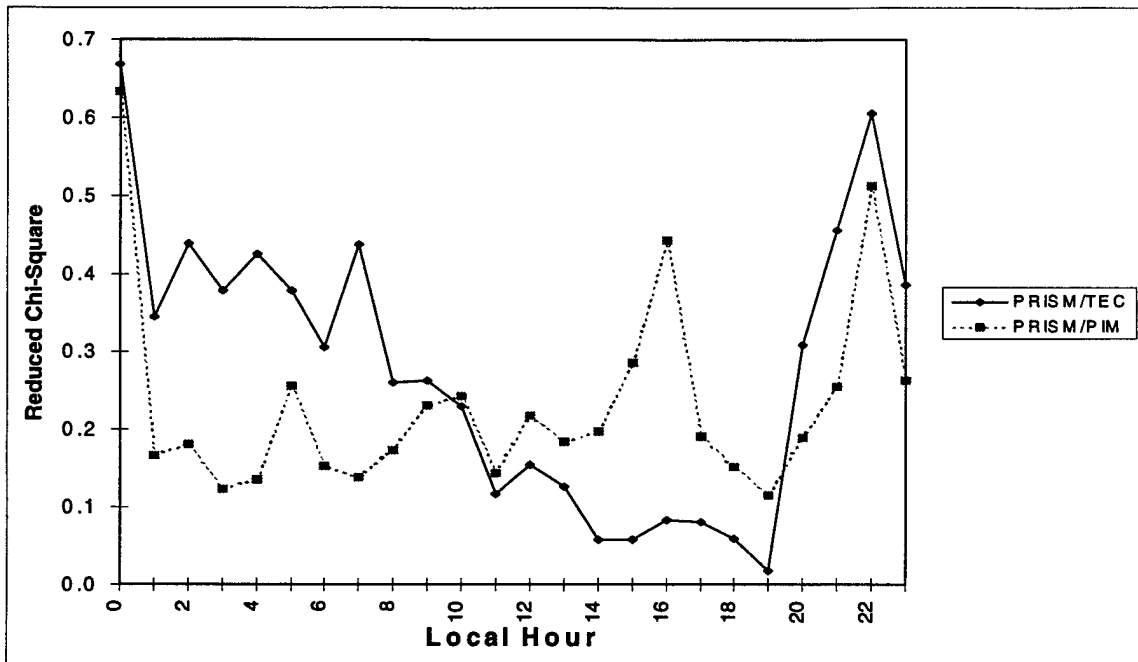


Figure 29: Point Arguello Reduced Chi-Squared for Equinox foF2

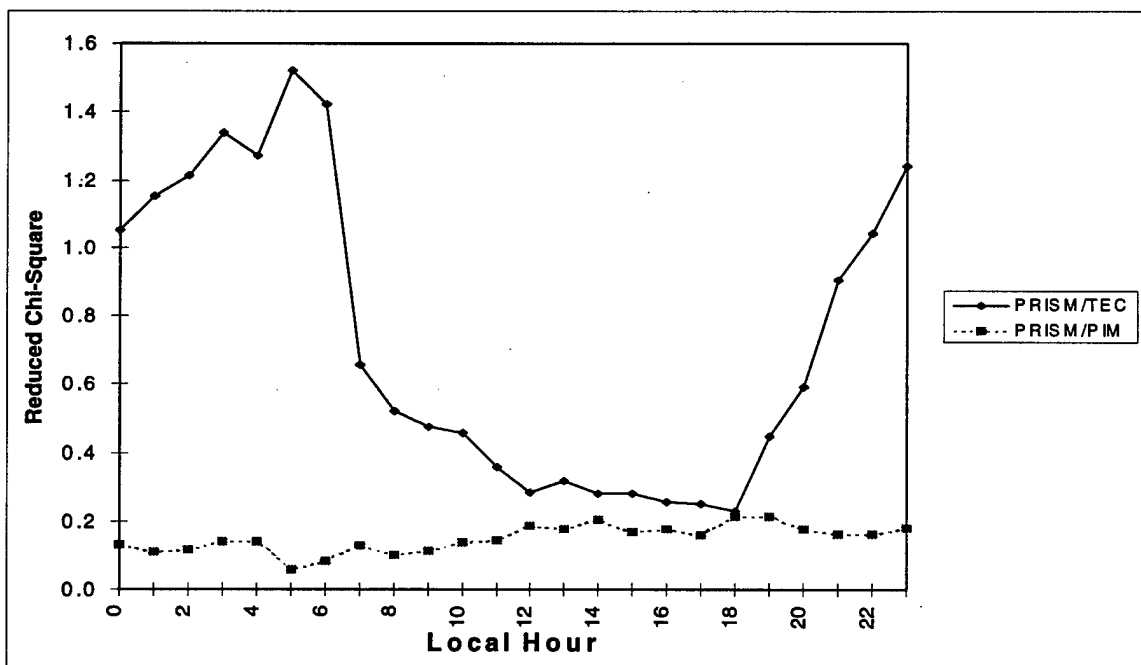


Figure 30: Wallops Island Reduced Chi-Squared for Equinox foF2

Table 24: Reduced Chi-Squared for Summer foF2

Summer	Point Arguello		Wallops Island	
Local Hour	PRISM/TEC	PRISM/PIM	PRISM/TEC	PRISM/PIM
0	3.041	0.083	0.649	0.067
1	3.518	0.042	0.704	0.077
2	3.129	0.037	1.027	0.076
3	2.820	0.068	1.409	0.092
4	3.047	0.045	1.123	0.068
5	2.225	0.039	1.251	0.091
6	1.304	0.041	1.357	0.211
7	1.609	0.140	0.537	0.142
8	1.084	0.239	0.358	0.171
9	1.041	0.349	0.291	0.245
10	0.757	0.140	0.145	0.101
11	0.598	0.135	0.261	0.148
12	0.722	0.201	0.269	0.103
13	0.750	0.281	0.532	0.331
14	0.484	0.298	0.497	0.310
15	0.448	0.418	0.337	0.174
16	0.672	0.225	0.407	0.168
17	0.695	0.146	0.627	0.080
18	0.952	0.144	0.561	0.099
19	0.842	0.081	0.599	0.308
20	0.672	0.099	0.508	0.203
21	1.168	0.087	0.506	0.171
22	1.793	0.084	0.748	0.199
23	2.757	0.172	0.591	0.139

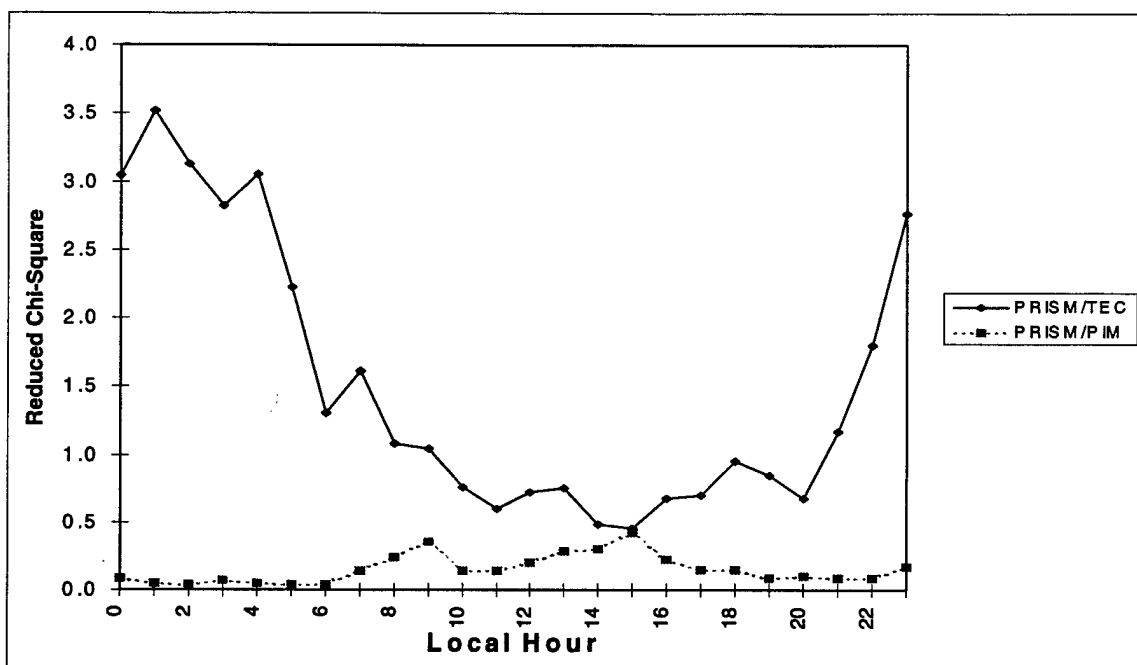


Figure 31: Point Arguello Reduced Chi-Squared for Summer foF2

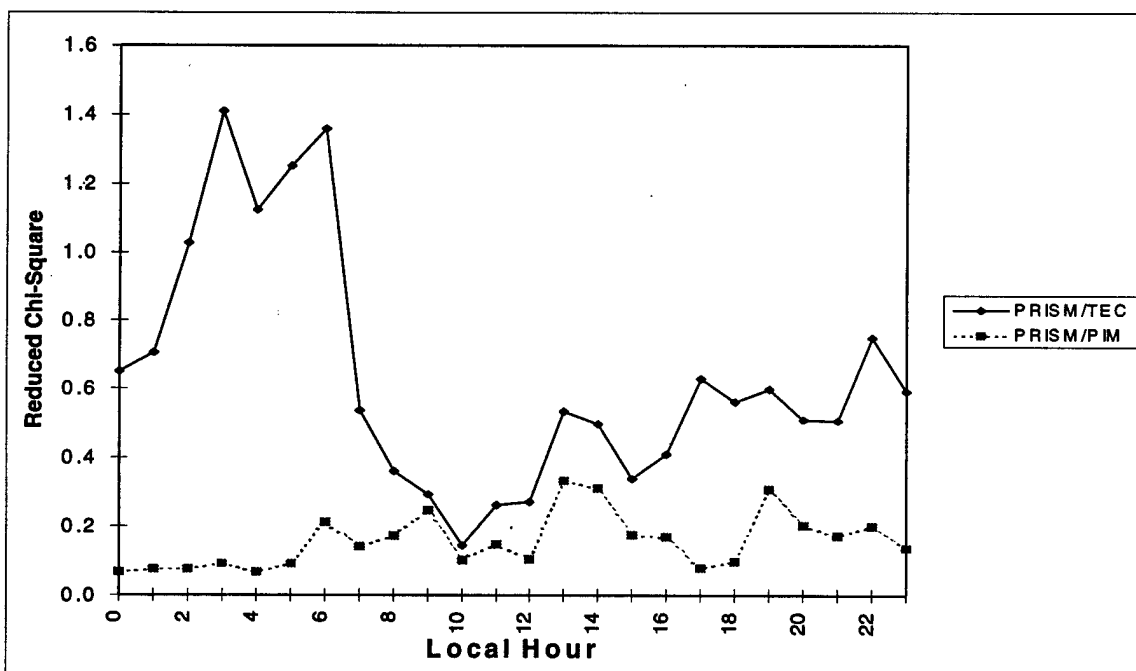


Figure 32: Wallops Island Reduced Chi-Squared for Summer foF2

Table 25: Reduced Chi-Squared for Winter foF2

Winter	Point Arguello		Wallops Island	
Local Hour	PRISM/TEC	PRISM/PIM	PRISM/TEC	PRISM/PIM
0	0.948	0.363	1.618	0.121
1	0.877	0.372	1.325	0.194
2	0.774	0.437	1.103	0.246
3	0.524	0.313	1.063	0.206
4	0.767	0.477	0.988	0.225
5	0.860	0.520	1.186	0.161
6	0.856	0.386	1.385	0.116
7	0.507	0.618	1.037	0.216
8	0.416	0.675	1.234	0.148
9	0.295	0.063	0.805	0.121
10	0.316	0.118	0.666	0.112
11	0.302	0.234	0.517	0.116
12	0.287	0.197	0.483	0.071
13	0.286	0.183	0.565	0.054
14	0.156	0.114	0.710	0.089
15	0.419	0.147	0.733	0.083
16	0.565	0.251	0.904	0.163
17	0.526	0.207	0.268	0.137
18	0.825	0.305	0.661	0.133
19	0.923	0.238	1.238	0.094
20	0.781	0.270	1.532	0.063
21	0.810	0.425	1.220	0.095
22	1.034	0.693	1.462	0.137
23	0.869	0.530	1.675	0.080

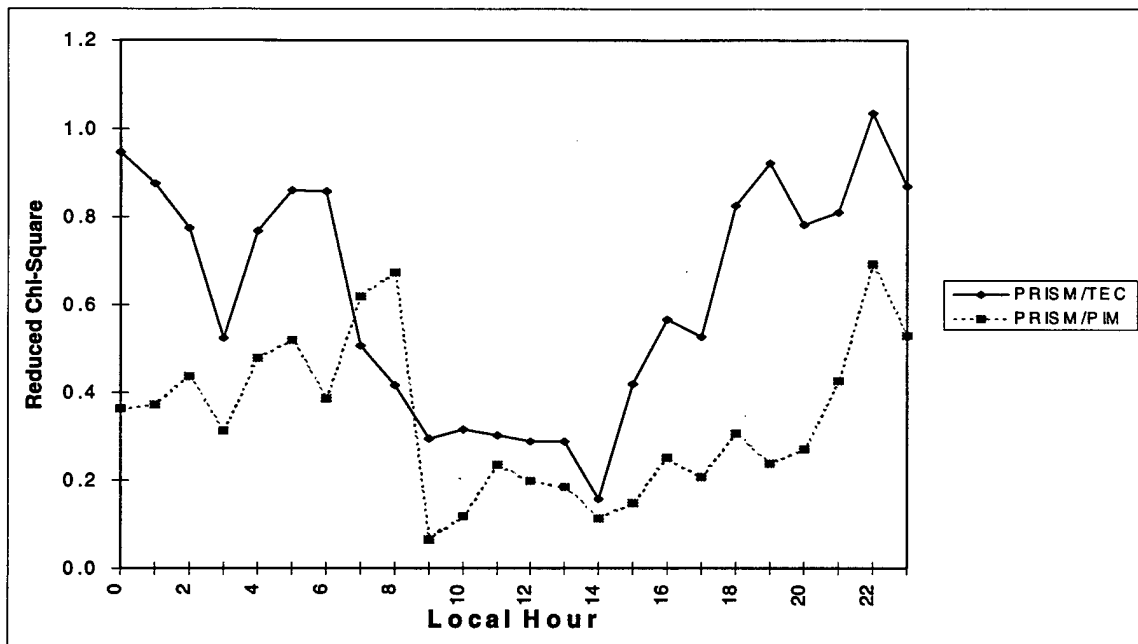


Figure 33: Point Arguello Reduced Chi-Squared for Winter foF2

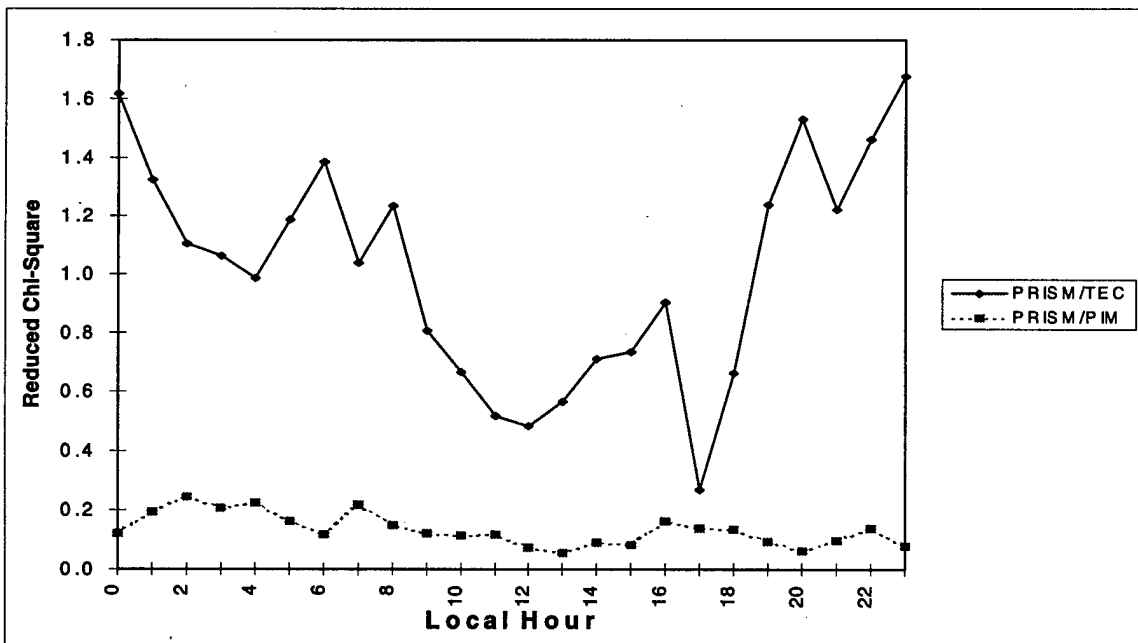


Figure 34: Wallops Island Reduced Chi-Squared for Winter foF2

Appendix F: Plots

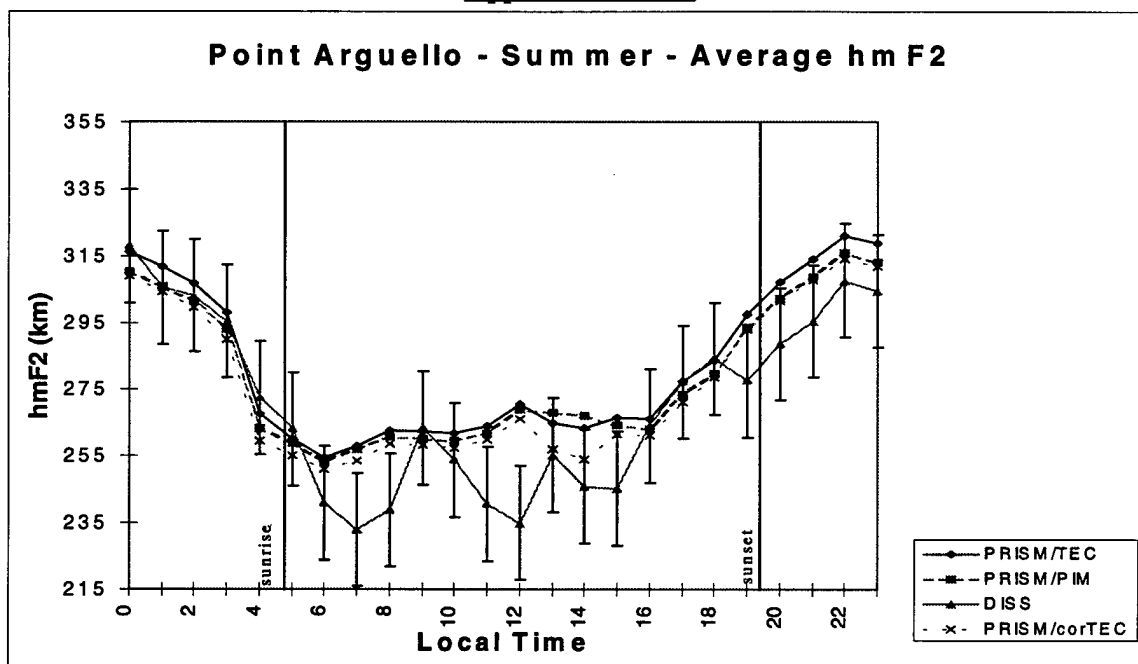


Figure 35: Point Arguello Average Summer hmF2

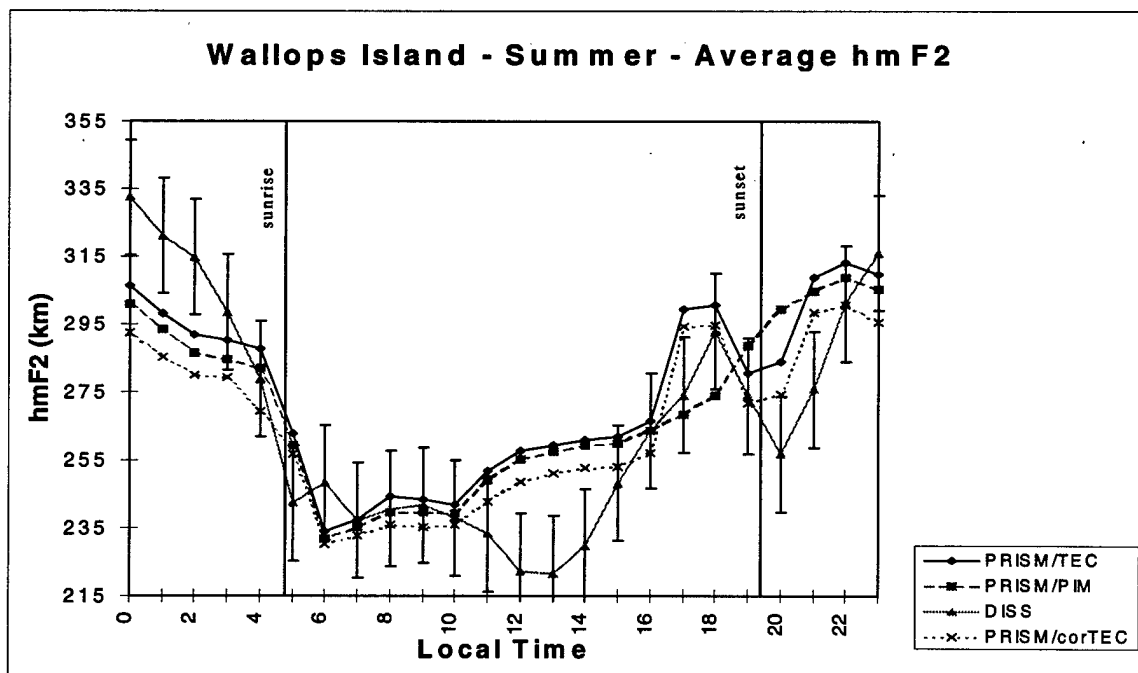


Figure 36: Wallops Island Average Summer hmF2

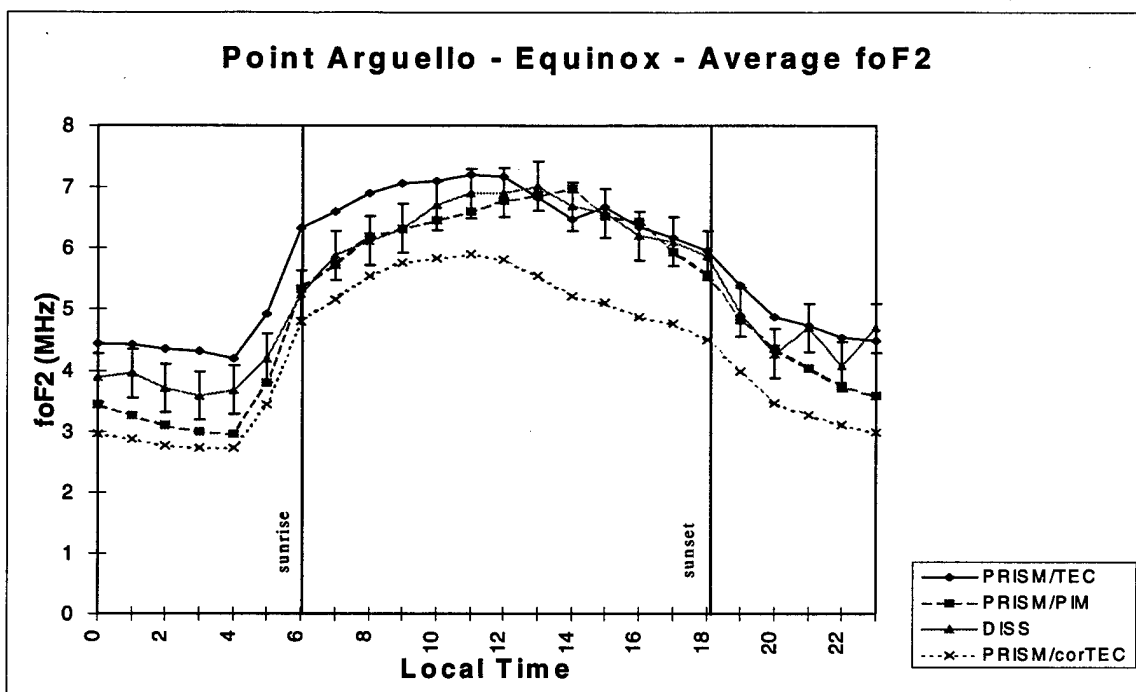


Figure 37: Point Arguello Average foF2 at Equinox

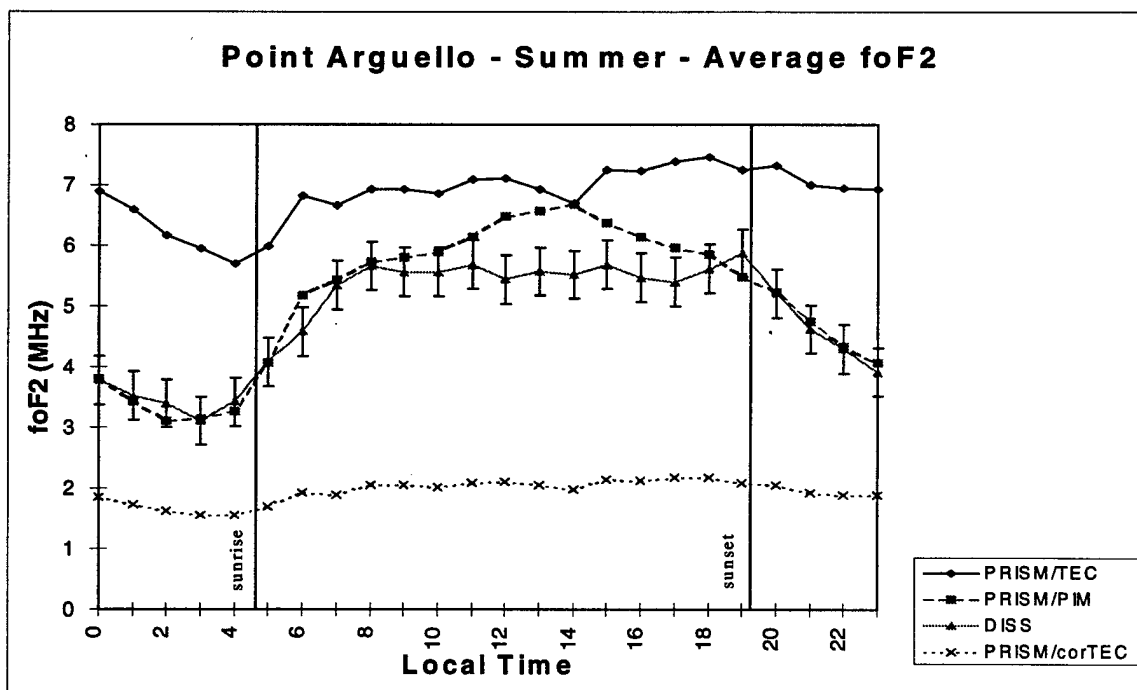


Figure 38: Point Arguello Average Summer foF2

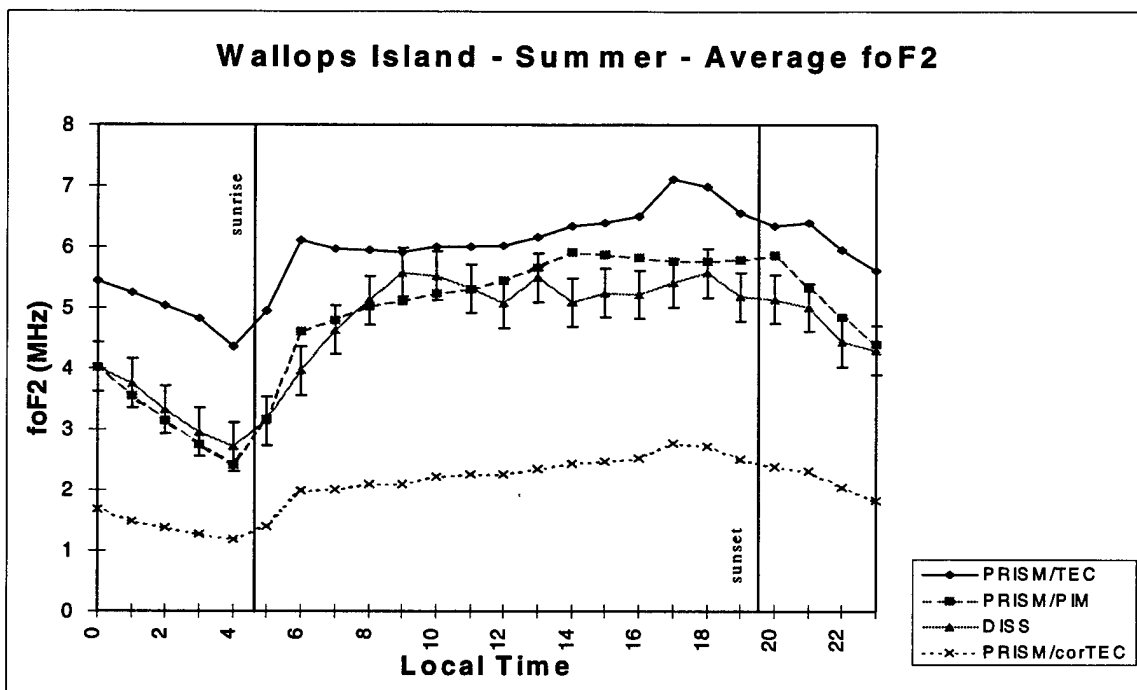


Figure 39: Wallops Island Average Summer foF2

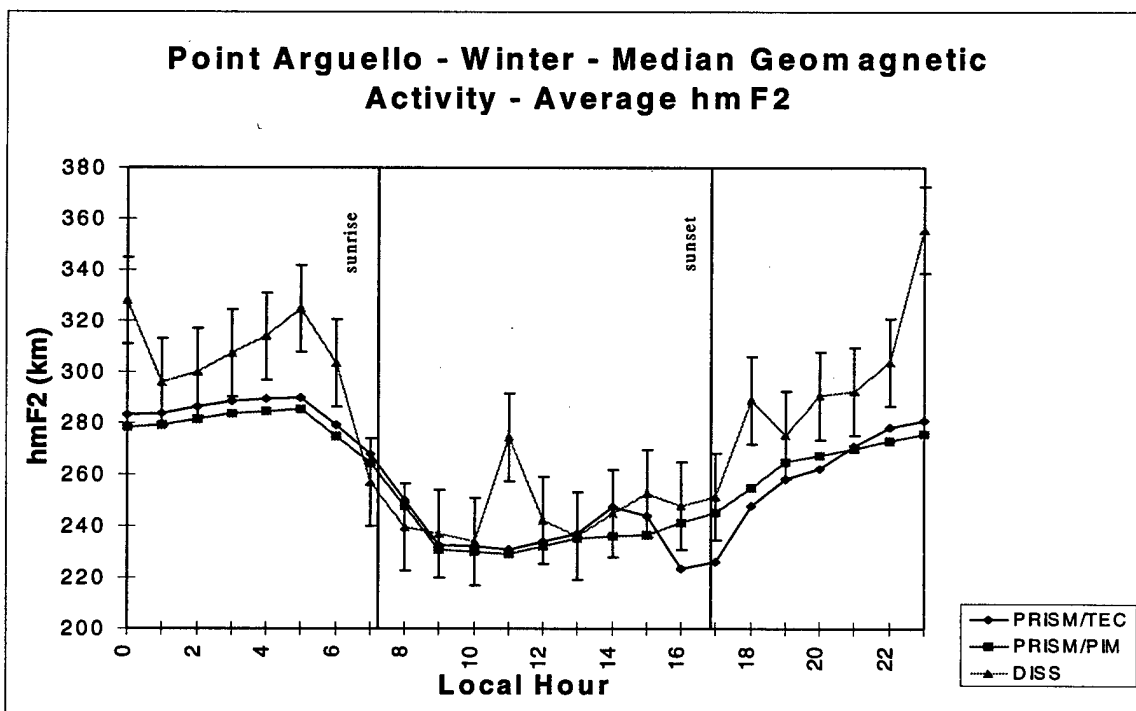


Figure 40: Point Arguello Average Equinox hmF2 for Median Geomagnetic Activity

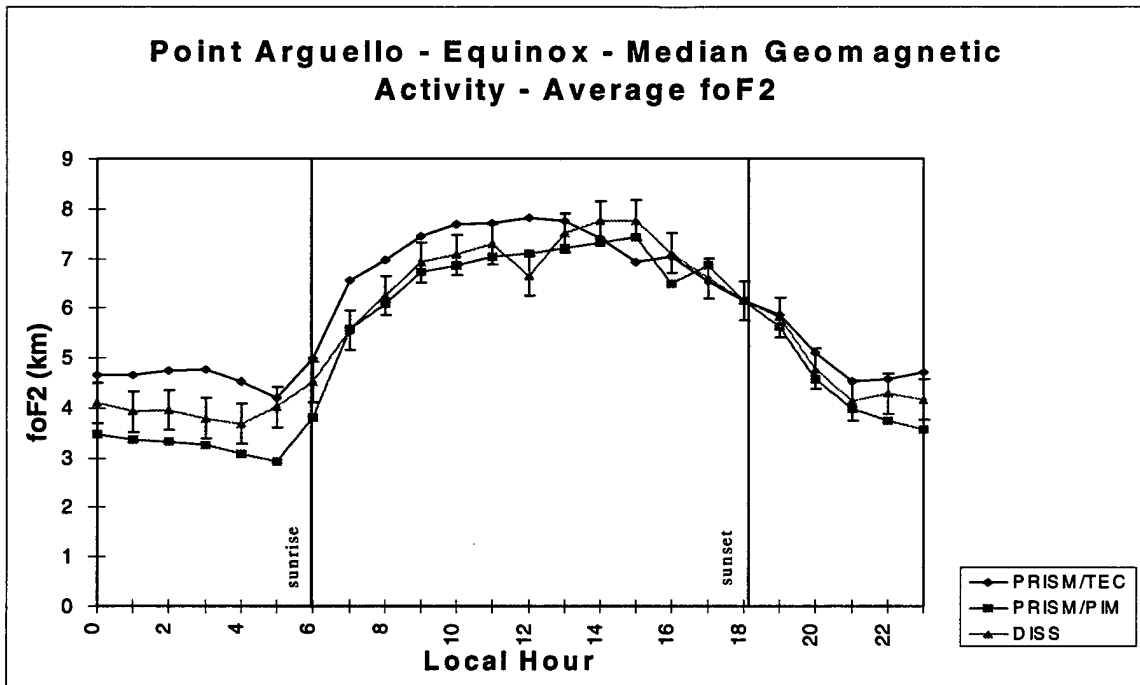


Figure 41: Point Arguello Average Equinox foF2 for Median Geomagnetic Activity

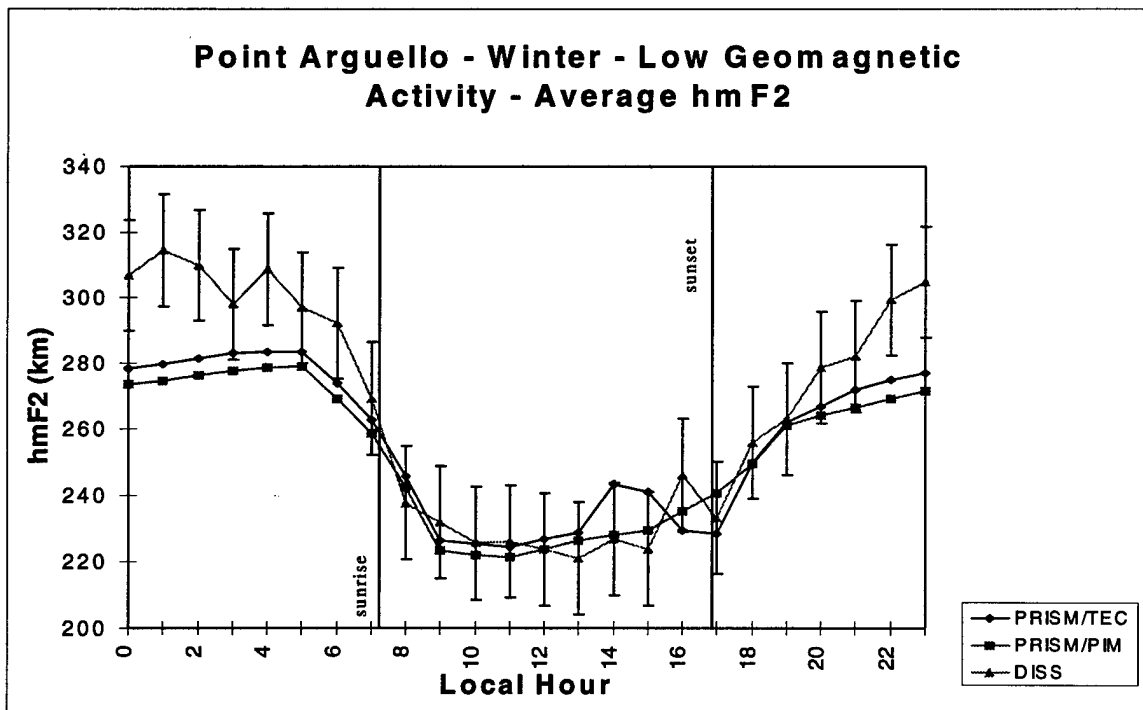


Figure 42: Point Arguello Average Winter hmF2 for Low Geomagnetic Activity

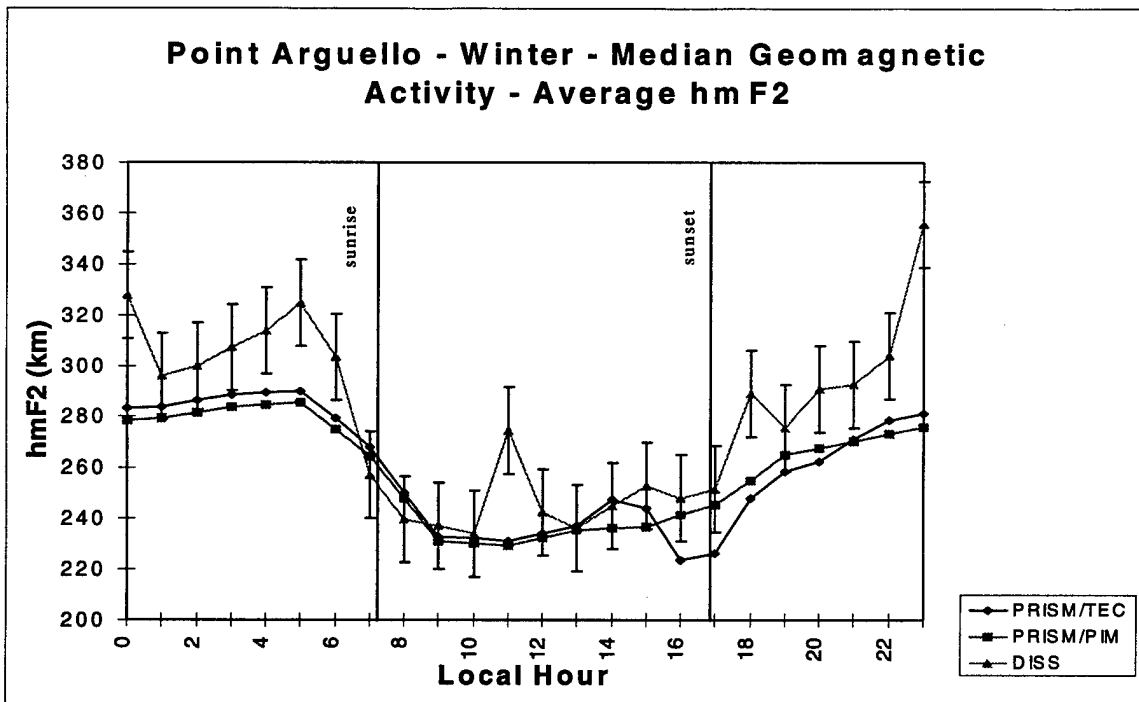


Figure 43: Point Arguello Average Winter hmF2 for Median Geomagnetic Activity

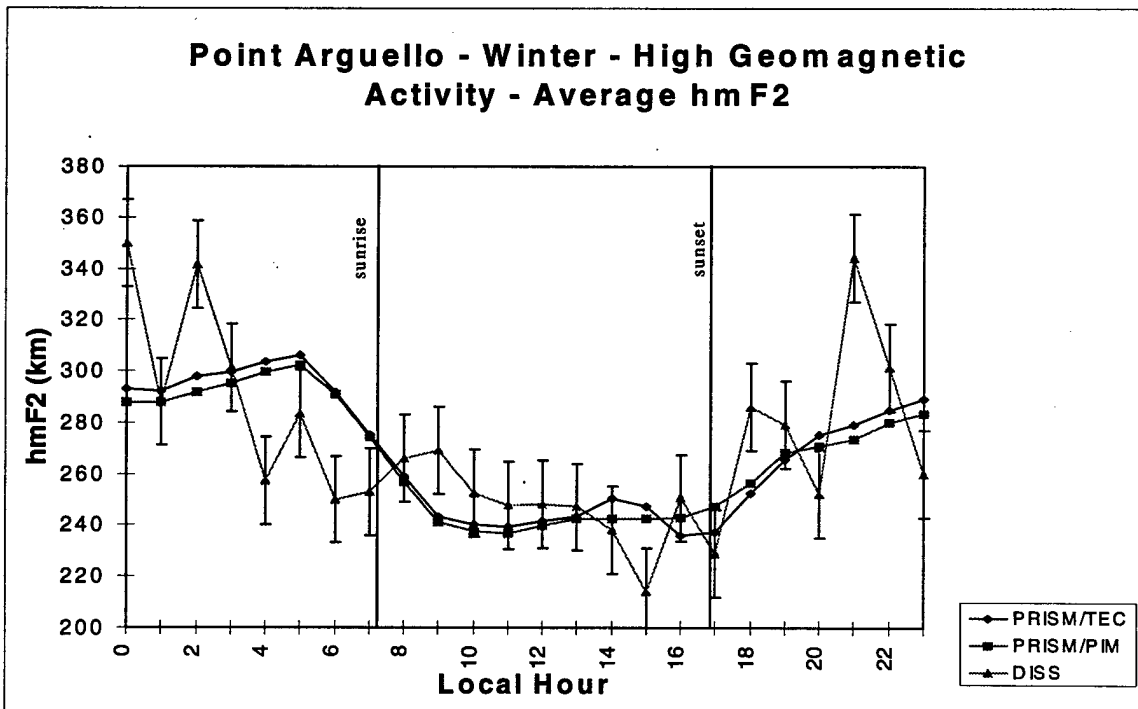


Figure 44: Point Arguello Average Winter hmF2 for High Geomagnetic Activity

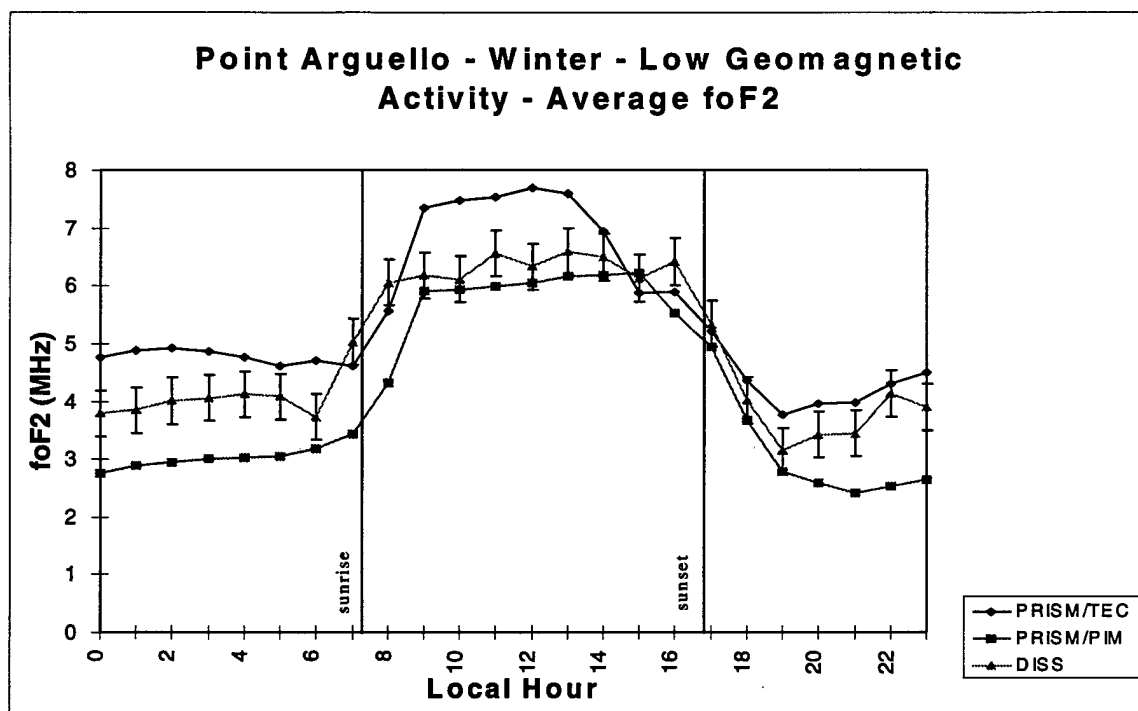


Figure 45: Point Arguello Average Winter foF2 for Low Geomagnetic Activity

Appendix G: Glossary

Auroral Oval – An auroral oval is an approximately circular band (about 4000 km in diameter) in the northern and southern hemispheres near 65° latitude where aurora are most intense at any given time. The ovals can expand towards the equator during magnetically disturbed periods, when the aurora becomes brighter.

CPI – Computational Physics Inc. of Waltham, Massachusetts, the company who wrote PRISM.

Critical frequency – The maximum plasma frequency of a particular layer in the ionosphere, the lowest frequency at which a radio wave can penetrate the layer.

DMSP – Defense Meteorological Satellite Program.

DoD – Department of Defense.

EDP – Electron density profile. A PRISM output which lists electron density at specified altitudes.

Fabry-Perot optical interferometers – An instrument that measures thermospheric winds by calculating Doppler shifts of airglow emissions.

Geomagnetic Activity – Any type of time varying disturbance to the Earth's magnetic field caused by electric current flowing in the magnetosphere and ionosphere.

Geomagnetic Coordinates – Similar to geographic latitude and longitude to locate specific places on the globe, except geomagnetic latitude and longitude are in respect to the earth magnetic poles which are offset from its geographic poles.

GPS – Global Positioning System – a constellation of twenty-four satellites in an orbit 22,000 km above the surface of the earth providing navigational and atmospheric information.

Gravity waves – An oscillation of plasma (with a period hours) occurring in the ionosphere.

IMF – Interplanetary Magnetic Field – The magnetic field carried out from the Sun by the solar wind.

In situ plasma measurements, measurements taken at the altitude of the measuring satellite (DMSP measures total ion density and one component of the horizontal ion drift using its Scintillation Meter on the SSIES instrument package) [Daniell et al., 1994].

Incoherent Scatter Radar – A ground-based remote sensing technique using the re-radiation of incident electromagnetic energy by free electrons, called Thomson scatter. Incoherent Scatter Radar works with a very weak signal, therefore it requires a powerful transmitter, a large antenna, and a extremely sensitive receiver. Its two advantages over ionosondes is its ability to ‘see’ beyond the level of peak electron density and its better spatial resolution [Hargreaves, 1992].

Langmuir probe – a satellite-based analysis tool which measures an electric current from electron or ions depending on the sign and magnitude of the potential applied [Hargreaves, 1992].

Lidar – a technique utilizing a laser which is pulsed from which heights can be deduced from the time delay and density from back-scattered intensity. Also temperature may be deduced from the Doppler broadening of the returned spectrum and the component of the wind in the line of sight can be found from its mean Doppler Shift [Hargreaves, 1992].

Magnetic flux tube – A hypothetical envelope containing the F region plasma whose gyrocenters make up a magnetic field line.

Magnetometers – A instrument aboard satellites which can measure magnetic fields.

Neutral wind – The movement of plasma in the plasmasphere and ionosphere.

Particle precipitation – The release of charged particles stored in Earth’s magnetosphere into the atmosphere. The particles flow along magnetic field lines, and when they strike the atoms of the upper atmosphere, they cause them to glow creating the aurora.

Polar Cap – The region inside the auroral oval where magnetic field lines from Earth extend into the magnetotail and sometimes into interplanetary space.

Pre-reversal enhancement – A brief duration surge before local sunset in the eastward electric field which will cause the F layer plasma to be driven to higher altitudes.

PRISM – Parameterized Real-time Ionospheric Specification Model.

Solar Cycle – The regular increase and decrease in the level of solar activity, usually measured by the number of sunspots on the solar surface. The time between successive maxima or minima in the sunspot number is about 11 years. Periods of large sunspot numbers are called “solar maximum” or “active sun”, while periods of low sunspot number are called “solar minimum” or “quiet sun”.

TEC – Total Electron Content - the integrated number of electrons found within a 1 m^2 column from the surface of the earth through the top of the ionosphere.

TEC Unit – a unit of measure equal to 10^{16} electrons per square meter.

TID – A traveling ionospheric disturbance is an equatorward traveling wave caused by auroral heating events and can affect electron content and peak heights. TIDs can last from one hour up to a full day [Hargreaves, 1992].

Bibliography

1. Anderson, David N. "Corrected TEC Values." Electronic Message. 13:03 EST, 4 September 1997.
2. Bailey, G. J., N. Balan, and Y. Z. Su, "The Sheffield University Plasmasphere Ionosphere Model – a Review," Journal of Atmospheric and Solar-Terrestrial Physics 59 (13): 1541-1552, 1997.
3. Beach, T. L., M. C. Kelley, and P. M. Kintner, "Total Electron Content Variations due to Non-classical Traveling Ionospheric Disturbances: Theory and Global Positioning System Observations," Journal of Geophysical Research 102 (A4): 7279 - 7292, 1997.
4. Bevinton, Philip R. and D. Keith Robinson, Data Reductions and Error Analysis for the Physical Sciences. New York: McGraw-Hill Inc., 1992.
5. Biondi, M. A., J. E. Meriwether, B. G. Fejer, S. A. Gonzalez, and D. C. Hallenbeck, "Corrections to 'Seasonal Variations in the Thermospheric Wind measured at Arequipa, Peru' and 'Equatorial Thermospheric Wind Change During the Solar Cycle: Measurements at Arequipa, Peru from 1983 to 1990' by Biondi et al.," Journal of Geophysical Research, 100 (A3): 7863, 1993.
6. Brace, L. H., and R. F. Theis, "Global Empirical Models of Ionospheric Electron Temperature in the Upper F-Region and Plasmasphere Based on In Situ Measurements from the Atmosphere Explorer-C, ISIS 1, and ISIS 2 Satellites", Journal of Atmospheric and Terrestrial Physics, 43: 1317, 1981.
7. Brown, Lincoln, Computational Physics Inc. Programmer, Waltham, Massachusetts. Telephone interview. 18 September 1997.
8. Chen, C. F., B. W. Reinisch, J. L. Scali, X. Huang, R. R. Gamache, M. J. Buonsanto, and B. D. Ward, "The Accuracy of Ionogram-Derived N(h) Profiles," Advances in Space Research 14 (12): 43-46, 1994.
9. Computational Physics Inc., "Changes to PRISM 1.6b for PRISM 1.7" Memorandum. 30 September 1996.
10. Conkright, Raymond O., "DISS Accuracy," Electronic Message. 12:51 MST, 18 September 1997.

11. Conkright, Raymond O., Kenneth Davies, and Steve Musman, "Comparisons of Ionospheric Total Electron Contents Made at Boulder, Colorado, Using the Global Positioning System," Radio Science, 32 (4): 1491-1497, 1997.
12. Coxwell, R. D., Validation of the Parameterized Real-Time Ionospheric Specification Model (PRISM) Version 1.6b Using TOPEX Total Electron Content (TEC) Data, MS Thesis, AFIT/ENP/GAP/96D. School of Engineering, Air Force Institute of Technology (AETC), Wright-Patterson AFB, OH, 1996.
13. Daniell, Robert E. Parameterized Real-Time Ionospheric Specification Model, PRISM Version 1.7b: Contract F19628-89-C-0005. Waltham, MA: Computational Physics, Inc., 1 December 1991, (AD-A251589).
14. Daniell, Robert E. PRISM: A Parameterized Real-Time Ionospheric Specification Model, Version 1.5: Contract F19628-92-C-0044. Waltham, MA: Computational Physics Inc., 31 May 1995, (AD-A299664).
15. Daniell, Robert E, William G. Whartenby, and Lincoln D. Brown. PRISM Validation: Contract F19628-92-C-0044. Waltham, MA: Computational Physics, Inc., 13 June 1994, (AD-A288476).
16. Davies K. and G. K. Hartmann, "Studying the Ionosphere with the Global Positioning System", Radio Science, 32 (4): 1695-1703, 1997.
17. Decker, Dwight T., Boris V. Koselov, B. Basu, J. R. Jasperse, and V. E. Ivanov, "Collision Degradation of the Proton-H Atom fluxes in the Atmosphere: A Comparison of Theoretical Techniques," Journal of Geophysical Research 101 (A2): 26,947 - 26960, 1996.
18. Department of the Air Force. Handbook of Geophysics and the Space Environment: Ed. Adolph S. Jursa. Air Force Geophysics Laboratory, Air Force Systems Command, 1985. (AD-A167000).
19. Doherty, P., "GPS bias Questions." Electronic Message. 12:33 EST, 31 July 1987.
20. Fejer, B. G., E. R. de Paula, R. A. Heelis, and W. B. Hanson, "Global Equatorial Ionospheric Vertical Plasma Drifts Measured by the AE-E Satellite," Journal of Geophysical Research, 100: 5769-5776, 1995.
21. Hardy D. A., M. S. Gussenhoven, E. Holeman, "A Statistical Model of Auroral Precipitation," Journal of Geophysical Research 90 (A5): 4229-4248, 1985.
22. Hargreaves, J. K. The Solar-Terrestrial Environment, Cambridge, Great Britain: Cambridge University Press , 1992.

23. Hedin, A. E., N. W. Spencer, and T. L. Killeen, "Empirical Global Model of Upper Thermosphere Winds Based on Atmospheric and Dynamics Explorer Satellite Data", Journal of Geophysical Research, 93: 9959-9978, 1988.
24. Hedin A. E., E. L. Fleming, A. H. Manson, F. J. Schmidlin, S. K. Avery, R. R. Clark, S. J. Franke, G. J. Fraser, T. Tsuda, F. Vial, and R. A. Vincent, "Empirical Wind Model for the Upper, Middle and Lower Atmosphere," Journal of Atmospheric and Terrestrial Physics 58 (13): 1421-1447, 1996.
25. Heelis, R. A., P.C. Kendall, R. J. Moffett, D. W. Windle, and H. Rishbeth, "Electrical coupling of the E and F-regions and its effect on F-region drifts and winds," Planetary Space and Science 22: 743-756, 1979.
26. Heppner, J. P., and N. C. Maynard, "Empirical High-Latitude Electric Field Models," Journal of Geophysical Research 92 (A5): 4467-4489, 1987.
27. Kelley, Michael C., The Earth's Ionosphere, Academic Press, Inc., San Diego, CA: 1989.
28. McNamara, L. F., "The Use of Total Electron Content Measurements to Validate Empirical Models of the Ionosphere," Advances in Space Research 5 (4): 81-90, 1985.
29. Schunk R. W., and J. J. Sojka, "Ionosphere-Thermosphere Space Weather Issues," Journal of Atmospheric and Terrestrial Physics 58 (4): 1527-1574, 1996.
30. Strickland, D. J., D. L. Book, T. P. Coffey, and J. A. Fedder, "Transport Equation Techniques for the Deposition of Auroral Electrons," Journal of Geophysical Research 81 (16): 2755-2764, 1976.
31. Tascione, Thomas F., Introduction to the Space Environment, Second Edition, Malabar, FL: Krieger Publishing, 1992.
32. Titheridge, J. E., "Aeronomical Calculations of Valley Size in the Ionosphere," Advances in Space Research, 10 (8): 21-24, 1990.

Vita

Captain Shawn D. Filby was born on 9 March 1967 in New Castle, Pennsylvania. He graduated from high school in 1985 and entered undergraduate studies at Grove City College in Grove City, Pennsylvania. He graduated with a Bachelor of Science degree in Applied Physics in May of 1989. He received his commission as a second lieutenant in the United States Air Force on 13 May 1989.

Captain Filby has held several operational weather positions including the Army Aviation Center, Fort Rucker, Alabama; Kunsan Air Base, Republic of Korea; and Schofield Barracks, Hawaii. In May 1996, he entered the School of Engineering, Air Force Institute of Technology, Wright-Patterson Air Force Base, Ohio.

He is married to the former Melanie Jean Hardie of Waianae, Hawaii. They have one son, Graham Curtis who was born November 14, 1997.

Permanent Address: 1910 Stanton Avenue
New Castle, PA 16101

REPORT DOCUMENTATION PAGE			Form Approved OMB No. 0704-0188	
Public reporting burden for this collection of information is estimated to average 1 hour per response, including the time for reviewing instructions, searching existing data sources, gathering and maintaining the data needed, and completing and reviewing the collection of information. Send comments regarding this burden estimate or any other aspect of this collection of information, including suggestions for reducing this burden, to Washington Headquarters Services, Directorate for Information Operations and Reports, 1215 Jefferson Davis Highway, Suite 1204, Arlington, VA 22202-4302, and to the Office of Management and Budget, Paperwork Reduction Project (0704-0188), Washington, DC 20503.				
1. AGENCY USE ONLY (Leave blank)		2. REPORT DATE November 1997		3. REPORT TYPE AND DATES COVERED Master's Thesis
4. TITLE AND SUBTITLE A VALIDATION OF THE PARAMETERIZED REAL-TIME IONOSPHERIC SPECIFICATION MODEL (PRISM) VERSION 1.7B			5. FUNDING NUMBERS	
6. AUTHOR(S) Shawn D. Filby, Captain, USAF				
7. PERFORMING ORGANIZATION NAME(S) AND ADDRESS(ES) Air Force Institute of Technology 2750 P Street WPAFB OH 45433-7765			8. PERFORMING ORGANIZATION REPORT NUMBER AFIT/GAP/ENP/97D-03	
9. SPONSORING/MONITORING AGENCY NAME(S) AND ADDRESS(ES) PL/GPIM 29 Randolph Road Hanscom AFB, MA 01731-5000			10. SPONSORING/MONITORING AGENCY REPORT NUMBER	
11. SUPPLEMENTARY NOTES				
12a. DISTRIBUTION AVAILABILITY STATEMENT Approved for public release; distribution unlimited			12b. DISTRIBUTION CODE	
13. ABSTRACT (Maximum 200 words) <p>The most current version of the Parameterized Real-time Ionospheric Specification Model (PRISM), version 1.7b, was validated using Digital Ionospheric Sounding System (DISS) measurements of F2 layer critical frequency (foF2) and F2 peak electron density height (hmF2) as the "ground truth." PRISM was executed, first, with no real-time input parameter and, second, with Global Positioning System (GPS) Total Electron Content (TEC) measurements as the sole real-time parameter. Hourly values of hmF2 and foF2 over 123 days in 1994-1996 (solar minimum conditions) and covering three seasons (equinox, summer solstice, and winter solstice) were compared for Wallops Island, Virginia, and Point Arguello, California, which both have a GPS receiver and a nearby DISS station. Values of hmF2 and foF2 from the DISS data, the PRISM output with no real-time input parameters, and the PRISM output with the GPS TEC measurements are compared as a function of season and local time. Results indicate PRISM overestimates foF2 by 20-30% when ingesting GPS TEC. On a subsequent execution of PRISM, the GPS TEC measurements were decreased by four TEC units as an estimation of the topside light ion (He, H) and plasmaspheric electrons which are not considered in the physical models of PRISM. PRISM underestimates foF2 by 30-40% and underestimates hmF2 by as much as 40 km in the post-midnight time-frame when driven by the corrected TEC values.</p>				
14. SUBJECT TERMS Ionospheric Models, Ionosphere, Space Environment, Atmospheric Models			15. NUMBER OF PAGES 127	
			16. PRICE CODE	
17. SECURITY CLASSIFICATION OF REPORT UNCLASSIFIED	18. SECURITY CLASSIFICATION OF THIS PAGE UNCLASSIFIED	19. SECURITY CLASSIFICATION OF ABSTRACT UNCLASSIFIED	20. LIMITATION OF ABSTRACT UL	